



NTNU – Trondheim
Norwegian University of
Science and Technology

On Modeling of a Ship Propulsion System for Control Purposes

Andreas Torp Karlsen

Master of Science in Engineering Cybernetics

Submission date: June 2012

Supervisor: Tor Arne Johansen, ITK

Co-supervisor: Bjørnar Wiulsrød, Kongsberg Maritime
Aleksander Veksler, ITK
Ivar Halvorsen, ITK

Norwegian University of Science and Technology
Department of Engineering Cybernetics

That which does not kill us makes us stronger.

Friedrich Nietzsche

Abstract

In this thesis a model of a ship propulsion system containing an engine, turbocharger, propeller and ship was constructed. The purpose of the model is to be used in controller design and testing. This is motivated by the fact that testing large marine diesel engines is limited due to large costs and difficulty providing a proper testbed facility.

First compressor and turbine models were developed by fitting parameters to manufacturer turbocharger maps. A novel compressor model was made from using exponential functions. The performance of the compressor model surpassed that of a model commonly used in literature. However, to conclude this in the general case, more testing has to be performed. The development of an accurate turbocharger model was stimulated by possibilities of variable area turbine, wastegate and exhaust gas recirculation control. This would again lead to better transient air-to-fuel ratio control, turbocharger speed control and the reduction of pollutants.

Extensions were made to an existing mean value engine model developed in an earlier project work by the same author, this included an intercooler and overload protection. The overload protection works through the use of fuel limiters based of torque and scavenging air pressure. In simulations these limiters showed to effectively maintain the air-to-fuel ratio for perfect combustion, however, at an increased engine response time. It was argued that the limiters could be superfluous if appropriate control of the air-to-fuel ratio was achieved.

The engine and turbocharger were put to the test in simulations. Despite the lack of turbocharger experimental data in low speed regions, the simulations proved that the turbocharger model could cope with low engine load conditions at reduced turbocharger speed. In fact, results show that the engine and turbocharger models worked excellent in the entire speed region.

Furthermore a propeller and ship model was developed. These models were tested in simulations together with a PI engine speed controller. Due to limited fuel actuation an integrator anti-windup scheme had to be included in the controller. The simulations showed that the PI controller was able to follow a slowly changing speed setpoint. However, due to the fact that the model is nonlinear and that no linearization, gain scheduling or excessive parameter tuning was performed, more advanced controller performance was not investigated. Moreover, further research on creating controllers for the purpose of suppressing propeller load torque fluctuations and subsequent engine overspeed is recommended. The total ship propulsion system showed to work in accordance to expected performance.

All in all, this thesis provided as an enlightenment of the parameters and principles that are important in control of propulsion plants. Furthermore, it gives a testing environment for control design of various applications.

Sammendrag

Denne rapporten inneholder modellutvikling av et skips fremdriftssystem med tilhørende motor, turbolader, propell og skip. Modellens hensikt er å bli brukt til regulatordesign og regulatortesting. Dette motiveres av det faktum at testing på store dieselmotorer er begrenset grunnet høye kostnader og vanskeligheter med å sette opp et testmiljø.

Først ble kompressoren og turbinen modellert ved å tilpasse modellparametere til en produsents turboladerkart. En helt ny kompressormodell ble utviklet ved å bruke eksponentialfunksjoner. Den nye modellens ytelse overgikk ytelsen til en populær modell fra litteraturen. Dette kan imidlertid ikke konkluderes i det generelle tilfelle uten å teste ut modellene på flere kompressorkart. Utviklingen av nøyaktige turboladermodeller var motivert av muligheten for regulering av variabel geometri turbin, wastegate og eksosresirkulering. Dette vil igjen kunne føre til bedre kontroll av luft-drivstofforholdet, turboladerens hastighet og bidra til reduksjon av miljøgiftutslipp.

Utvidelser ble utført på en eksisterende middelverdibasert motormodell som ble utviklet av forfatteren i et tidligere prosjektarbeid. Utvidelsene inkluderte en lade-luftkjøler og overbelastningsvern basert på drivstoffbegrensere i forhold til dreiemoment og lufttrykket i inntaksmanifoldet. Under simulering viste disse drivstoffbegrensere seg å opprettholde luft-drivstofforholdet på et slikt nivå at perfekt drivstoffbrenning ble utført. Dette viste seg imidlertid å øke motorens responstid. Det ble hevdet at begrensere kunne være overflødige dersom hensiktsmessig regulering av luft-drivstofforholdet ble innført.

Motoren og turboladeren ble satt på prøve under simuleringer. Til tross for mangelen på eksperimentelle data for lav turboladerhastighet viste simuleringen at turboladermodellene kunne takle lave motorbelastninger og tilhørende lav turboladerhastighet. Faktisk viser resultatene at motor- og turboladermodellen fungerer utmerket i hele hastighetsregimet til motoren.

Videre ble en propell- og en skipsmodell utviklet. Disse modellene ble testet i simulering sammen med en PI-hastighetsregulator for motoren. Grunnet begrenset drivstoffpådrag måtte integratorbegrensning inkluderes i regulatoren. Simuleringene viste at PI-regulatoren var i stand til å følge et endret hastighetssettpunkt. Men på grunn av at modellen er ulineær og at linearisering og påfølgende gain scheduling ikke var inkorporert, ble mer avansert kontrollytelse ikke undersøkt. Videre anbefales det med ytterligere forskning på regulering av varierende propellerlast og påfølgende overhastighet av motoren. Skipsfremdriftsmodellen i sin helhet viste seg å virke i henhold til forventet ytelse.

Denne avhandlingen bidro til innsikt i hvilke parametere og prinsipper som er viktig i regulering av skipsfremdrift. Videre gir den et testmiljø for videre utvikling av ulike regulatorer.

Contents

List of Figures	iii
List of Tables	vii
Nomenclature	ix
1 Introduction	1
1.1 Background and Motivation	1
1.2 Previous Work	3
1.3 Research Objectives	4
1.4 Thesis Outlines	5
2 Theory	7
2.1 Ship Propulsion	7
2.1.1 Hull Resistance	7
2.1.2 Propeller Propulsion	11
2.1.3 Engine Layout and Load Diagrams	15
2.2 Turbocharger Maps	18
2.2.1 Compressor	20
2.2.2 Turbine	21
2.3 Least Squares Curve Fitting	22
3 Compressor Map Modeling	25
3.1 Flow Rate Interpolation	26
3.2 Flow Rate Modeling	28
3.2.1 Exponential Method	32
3.2.2 Exponential Threshold Method	36
3.2.3 Results and Discussion	37
3.2.4 Alternative Method (Rectangular Hyperbolas)	38
3.3 Efficiency	43
3.3.1 Polynomial Fit	43
3.3.2 Six Parameter Efficiency Model	44
3.3.3 Results and Discussion	44

3.4	Concluding Remarks	45
4	Turbine Modeling	49
4.1	Turbine Flow	50
4.2	Modification of Mass Flow Calculation	52
4.3	Turbine Efficiency	54
4.4	Concluding Remarks	56
5	Propeller, Ship and Engine	57
5.1	Interaction of Submodels	57
5.2	Propeller Modeling	58
5.2.1	Thrust and Torque	58
5.2.2	Propeller Inertia	61
5.3	Ship Surge Model	62
5.4	Engine Model Extensions	63
5.4.1	Intercooler	64
5.4.2	Shaft Friction	65
5.4.3	Overload Protection	65
6	Simulation of Engine and Turbocharger	69
6.1	Step Responses	69
6.2	Fuel Limiters	74
6.2.1	Inactive Limiters	74
6.2.2	Active Limiters	76
6.3	Concluding Remarks	77
7	Control	81
7.1	Linear PI Controller	81
7.2	Simulation	82
7.3	Concluding Remarks	85
8	Final Conclusions and Future Work	89
8.1	Conclusions	89
8.2	Recommendations for Future Work	91
	Bibliography	93
A	Engine/Turbocharger Performance Curves	97
B	Tables of Coefficients	101
C	Matlab/Simulink Files	105

List of Figures

1.1	Engine modeling approach.	4
2.1	Ship hull dimensions [1].	10
2.2	Total ship towing resistance $R_T = R_F + R_W + R_E + R_A$ [1].	10
2.3	Definition of speed of advance V_a and ship speed V_s	13
2.4	Illustration of propeller pitch and slip.	16
2.5	Ship propulsion running points and engine layout. (PD) Propeller design point, (PD') Alternative propeller design point, (SP) Service propulsion point, (MP) Specified propulsion point.	17
2.6	Engine load diagram [1].	19
2.7	Conceptual compressor performance map.	21
2.8	Conceptual turbine flow rate map.	22
2.9	Samples (circle), the least squares curve fit (solid) and the vertical deviations (dotted).	24
3.1	Linear interpolation (dashed) and piecewise cubic Hermit interpolation (dash-dot) of the nonlinear function $y = \sin x$ (solid).	26
3.2	Cross section of a centrifugal compressor (a) showing the impeller and diffuser. The compressor impeller (b) showing ideal air flow velocity (V_2), real air flow velocity (V_{2k}) and blade tip speed (U_2).	27
3.3	A compressor map with constant speed curves, surge line and choke line. Samples are taken from a real compressor map and speed curves are regenerated by Hermite interpolation.	28
3.4	Cubic interpolation of speed samples (blue circles) with color-coded turbocharger speed.	29
3.5	Surface fit of the compressor map samples (blue circles) with constant speed curves (solid red) projected into the (Q,PR)-plane. The projected samples are also shown (black cross).	29
3.6	The choke line pressure as a 7th order polynomial of Mach number.	32
3.7	Choke line samples represented with dimensionless parameters, the <i>choke flow</i> is fitted to a (a) 2nd, (b) 3rd, (c) 4th order polynomial of M . The <i>choke pressure</i> is fitted to a (d) 3rd, (e) 4th, (f) 5th order polynomial of M	33

3.8	Surge line samples represented with dimensionless parameters, the <i>surge flow</i> is fitted to a (a) 2nd, (b) 3rd, (c) 4th order polynomial of M . The <i>surge pressure</i> is fitted to a (d) 3rd, (e) 4th, (f) 5th order polynomial of M	33
3.9	Compressor speed curves given in dimensionless (Φ, Ψ) -coordinates.	34
3.10	Properties of the exponential function.	34
3.11	Surge volume flow rate fit as a second order (a) and third order (b) polynomial compressor blade tip speed.	38
3.12	Comparison of the exponential method and the threshold method. In addition to the sampled speed curves, an extended speed curve for $U_c = 425$ and an extrapolated curve for $U_c = 200$ are shown.	40
3.13	Modeled compressor volume flow rate at constant turbocharger speed with the alternative method. Solid curves represent the speed of the samples, the dashed curve indicates an extended speed curve for $U_c = 425$	40
3.14	Modeled compressor volume flow rate at constant turbocharger speed with the <i>improved</i> alternative method. Solid curves represent the speed of the samples, the dashed curve indicates an extended speed curve for $U_c = 425$	41
3.15	Comparing the exponential threshold flow model (solid) and the hyperbola model (dashed).	41
3.16	Normalized flow function $\Phi = \frac{k_3\Psi - k_1}{k_2 + \Psi}$ for $M = 0.874$. The lower left part of the graph resembles a speed curve. Asymptotes are showed as dashed lines.	42
3.17	The alternative flow model with poor choice of initial coefficient values. Solid curves represent the speed of the samples, the dashed curve indicates an extended speed curve for $U_c = 425$	42
3.18	Compressor efficiency samples (blue dots) with a 5th order polynomial surface fit. The compressor pressure ratio and volume flow rate are inputs.	46
3.19	Polynomial fit of the compressor efficiency in the (Q_c, Π_c) -plane. Efficiency is color-coded.	46
3.20	Contours of constant efficiency from the 5th order polynomial fit of Q_c and Π_c	47
3.21	Regenerated compressor map with speed lines (solid black), surge line (dashed black) and efficiency contours (colored).	47
4.1	Samples (dots) from the provided turbine flow map together with three different model fits.	53
4.2	Volume flow rate for the turbine given different exhaust manifold temperatures.	53

4.3	Flow through a restriction for a compressible fluid. Ψ shows the usual flow function, Ψ_{mod} is an approximation to the flow around pressure ratio of 1 to make it Lipschitz.	54
4.4	Typical turbine efficiency curve. The dotted line represents a higher exhaust manifold pressure.	55
5.1	Interaction the simulation model subsystems.	57
5.2	Inputs and outputs of the propeller model.	58
5.3	Open-water characteristics for a Wageningen B propeller with $D = 6.5\text{m}$, $Z = 5$, $P/D = 0.665$, $A_E/A_O = 0.57$ and $R_n = 2 \times 10^6$	60
5.4	Propeller thrust characteristics for $K_{T0} = 0.2896$, $K_{T1} = 0.1956$ and $K_{T2} = 0.1016$	60
5.5	Inputs and outputs of the ship model.	62
5.6	Inputs and outputs of the intercooler.	64
5.7	Torque limiter.	66
5.8	Scavenging air pressure limiter.	67
6.1	Simulink diagram for engine step responses with standard propeller curve load.	70
6.2	Simulation of the engine and turbocharger with the load following a theoretical propeller curve.	72
6.3	Compressor steady state load line. Samples represent fuel rack positions 0.3, 0.4, ..., 1.1.	73
6.4	Simulation of the engine/turbocharger response for a fuel rack step from $u = 0.3$ to $u = 1.0$ with <i>inactive</i> fuel limiters.	75
6.5	Simulink diagram of the simulation model with fuel limiters included .	76
6.6	Simulation of the engine/turbocharger response for a fuel rack step from $u = 0.3$ to $u = 1.0$ with <i>active</i> fuel limiters.	78
7.1	Simulink diagram of the engine governor. It includes a PI controller with integrator windup in addition to a scavenge air limiter and torque limiter (implemented as Matlab functions).	83
7.2	Simulink diagram for the engine/propeller/ship final simulation model.	84
7.3	Simulation of the engine and turbocharger with PI-controller.	86
7.4	Simulation of the ship and propeller with PI-controller	87
A.1	Compressor map for a MAN Diesel & Turbo TCA55 turbocharger (Courtesy of MAN Diesel & Turbo).	98
A.2	Turbine flow rate map for a MAN Diesel & Turbo TCA55 turbocharger (Courtesy of MAN Diesel & Turbo).	99
A.3	Performance curves for the MAN B&W 6L60MC-C mk7 two stroke marine diesel engine [2].	100

List of Tables

3.1	Parameters used in conversion to dimensionless values.	31
4.1	Regression coefficients from least squares fit of the turbine flow models.	52
5.1	Propeller quadrants of operation.	58
5.2	Propeller geometrical data.	59
5.3	Ship data for a large “Handymax” type bulk carrier [3].	63
5.4	Engine parameters of a MAN 6L60MC mk6 marine diesel engine.	64
7.1	Controller gains.	82
7.2	Simulation events for a ship simulation with a PI controller for engine speed.	83
B.1	Regression coefficients from least squares fit of the exponential compressor flow model (3.20).	101
B.2	Regression coefficients from least squares fit of the exponential threshold compressor flow model (3.29). Note that the polynomial order of the expressions (3.26) and (3.28) are increased by 1 to increase precision.	102
B.3	Regression coefficients from least squares fit of the alternative compressor flow model by rectangular hyperbolas (3.35).	102
B.4	Parameters from least squares fit of the 5th order compressor efficiency polynomial in (3.41).	103
B.5	Coefficients for K_T and K_Q for the Wageningen B-screw series propeller used in (5.5) and (5.6).	104
C.1	Description of Matlab scripts.	105
C.2	Description of Matlab functions.	106
C.3	Description of data files.	106
C.4	Description of Simulink files and Matlab functions within.	107

Nomenclature

Abbreviations

AFR	Air-to-fuel ratio
BMEP	Brake mean effective pressure
BSFC	Brake specific fuel consumption
CPP	Controllable pitch propeller
EGR	Exhaust gas recirculation
FMEP	Friction mean effective pressure
FPP	Fixed pitch propeller
IMEP	Indicated mean effective pressure
MCR	Maximum continuous rating
MVEM	Mean value engine model
SMCR	Specified maximum continuous rating
VAT	Variable area turbine

Greek

η_0	Open-water propeller efficiency	[–]
$\eta_{t,\max}$	Maximum turbine isentropic efficiency	[–]
η_B	Behind ship propeller efficiency	[–]
η_c	Compressor isentropic efficiency	[–]
η_i	Intercooler efficiency	[–]
η_R	Relative rotative efficiency	[–]
η_t	Turbine isentropic efficiency	[–]
κ_a	Ratio of specific heats for air	[–]
κ_e	Ratio of specific heats for exhaust gas	[–]
ω_e	Engine shaft angular frequency	[rad/s]
ω_{tc}	Turbocharger angular frequency	[rad/s]
Φ	Normalized compressor flow	[–]
Π_c	Pressure ratio over the compressor	[–]
Π_t	Turbine expansion ratio	[–]
Ψ	Compressor pressure head	[–]
ρ_a	Air density	[kg/m ³]

ρ_e	Exhaust gas density	[kg/m ³]
ρ_w	Water density	[kg/m ³]

Lowercase

\bar{p}_b	Break mean effective pressure	[Pa]
\bar{p}_f	Friction mean effective pressure	[Pa]
\bar{p}_i	Indicated mean effective pressure	[Pa]
$\bar{p}_{i,\max}$	Maximum indicated mean effective pressure	[Pa]
$\dot{m}_{c,\text{corr}}$	Corrected mass flow rate through the compressor	[kg/s]
$\dot{m}_{t,\text{corr}}$	Corrected mass flow rate through the turbine	[kg/s]
$\dot{m}_{t,\text{red}}$	Reduced mass flow rate through the turbine	[kg/s]
\dot{m}_a	Mass flow rate of air into the cylinders	[kg/s]
\dot{m}_c	Mass flow rate through the compressor	[kg/s]
\dot{m}_t	Mass flow rate through the turbine	[kg/s]
c_p	Air specific heat at constant pressure	[J/(kg K)]
c_t	Turbine correction factor	[-]
d_c	Compressor diameter	[m]
d_t	Turbine diameter	[m]
n	Propeller shaft speed	[r/s]
p_{amb}	Ambient pressure	[Pa]
p_{em}	Exhaust manifold pressure	[Pa]
p_{ep}	Exhaust pipe pressure	[Pa]
p_{im}	Intake manifold pressure	[Pa]
t/c	Ratio of maximum propeller blade thickness to length of the chord	[-]
t_d	Ship thrust deduction factor	[-]
u	Fuel index	[-]
w	Wake fraction number	[-]
z_c	Number of engine cylinders	[-]

Uppercase

\hat{Q}_t	Turbine map flow rate	[m ³ /(s \sqrt{K})]
A_E/A_O	Propeller blade area ratio	[-]
A_{Teq}	Turbine equivalent effective area	[m ²]
C_s	Exhaust gas velocity	[m/s]
D	Propeller diameter	[m]
F_n	Froude number	[-]
F_R	Fuel index (rack) position	[-]
J_{tot}	Shafting system total inertia	[kg m ²]
J_a	Propeller advance ratio	[-]
J_e	Engine moment of inertia	[kg m ²]
J_p	Propeller moment of inertia inertia	[kg m ²]

J_{eq}	Entrained water inertia	[kg m ²]
J_{tc}	Turbocharger system moment of inertia	[kg m ²]
K_Q	Propeller torque coefficient	[–]
K_T	Propeller thrust coefficient	[–]
K_{QB}	Propeller behind ship torque coefficient	[–]
M	Compressor Mach number	[–]
M_a	Ship added mass	[kg]
M_s	Ship mass	[kg]
N_{MCR}	Engine speed at MCR	[r/min]
$N_{tc,corr}$	Corrected rotational speed turbocharger	[r/min]
$N_{tc,red}$	Reduced rotational speed turbocharger	[(r/min)/√K]
N_d	Desired engine speed	[r/min]
N_e	Engine rotational speed	[r/min]
N_{tc}	Turbocharger rotational speed	[r/min]
P/D	Propeller pitch-diameter ratio	[–]
P_{MCR}	Engine brake power at MCR	[W]
P_b	Engine brake power	[W]
P_c	Compressor absorbed power	[W]
P_D	Propeller shaft power	[W]
P_E	Effective ship resistance power	[W]
P_p	Propeller consumed power	[W]
P_T	Propeller thrust power	[W]
P_t	Turbine produced power	[W]
$Q_{t,red}$	Reduced turbine volume flow rate	[m ³ √K/(s Pa)]
Q_B	Propeller torque behind ship	[N m]
Q_c	Compressor volume flow rate	[m ³ /s]
Q_e	Engine torque	[N m]
Q_f	Shaft friction torque	[N m]
Q_p	Propeller torque	[N m]
Q_t	Turbine volume flow rate	[m ³ /s]
R_A	Ship air resistance	[N]
R_a	Specific gas constant for air	[J/(kg K)]
R_E	Ship eddy resistance	[N]
R_e	Specific gas constant for exhaust gas	[J/(kg K)]
R_F	Ship frictional resistance	[N]
R_n	Reynolds number	[–]
R_R	Ship residual resistance	[N]
R_T	Total ship resistance	[N]
R_W	Ship wave resistance	[N]
S_R	Slip ratio	[–]
T_{ext}	External weather forces on the ship	[N]
T_c	Temperature of air from the compressor	[K]

T_i	Temperature after intercooler	[K]
T_p	Propeller thrust	[N]
T_w	Intercooler coolant water temperature	[K]
T_{amb}	Ambient temperature	[K]
T_{em}	Exhaust manifold temperature	[K]
T_{ep}	Exhaust pipe temperature	[K]
T_{im}	Intake manifold temperature	[K]
U_c	Compressor blade tip velocity	[m/s]
U_t	Turbine blade tip velocity	[m/s]
V_a	Propeller speed of advance	[m/s]
V_s	Ship surge velocity	[m/s]
Z	Number of propeller blades	[m ³]

Chapter 1

Introduction

Propulsion of modern merchant ships is dominated by diesel engines. Large two-stroke marine diesel engines are the leading type of prime mover that is widely used for propulsion of the majority of today's merchant vessels. The benefits of the large diesel engines as marine propulsion are the superior efficiency, the possibility of burning heavy fuel oil and that slow-speed engines can be directly connected to the propeller without the need of a gearbox and clutch. Regardless of the advantages, it is important to include safe operation of the engine, having control over the propeller revolutions and accordingly the ship's speed. When the engine is running near its maximum value, rough seas can cause it to overspeed and induce damage to the engine. Therefore complete awareness of the factors impacting the engine speed and robust control is important. Losing propulsion is dangerous and can cause human and environmental hazard, so it is best avoided. Moreover, with today's strict pollution regulations and high oil prices more accurate knowledge and control of the engine is sought after.

1.1 Background and Motivation

The background for writing a thesis on modeling of a ship propulsion system comes from a summer internship at Kongsberg Maritime, Merchant Marine division in Horten. Kongsberg had a desire to develop a new low-speed diesel engine speed controller. However, making a speed controller without a predefined model to control or knowledge about the process is difficult. Hence, a ship propulsion system model had to be made. By modeling the process one acquires the awareness on what parameters affect the system and how to control it. Furthermore, a testing environment for the controller is needed as testing possibilities on real engines are limited.

The cost involved in purchase and installment a two-stroke marine diesel engine is high. Moreover, the sheer physical size and power output of the largest engines makes it difficult and time consuming setting up a proper testbed facility.

Therefore the use of engine models to describe the engine behavior is essential to understanding how different parameters affect the system, and to be used in controller design and testing. Experimental investigation of an engine's dynamic behavior is for the most part prohibited. One can not simply do live testing on a ship with the possibility of human loss and environmental damage by unstable control of the engine. Consequently, the use of simulation for transient response and optimization is of utmost importance. The model must be able to represent the engine's transient response, as well as steady state conditions.

Ship propulsion is a complex system, it contains the influences from several sources; engine, turbocharger, propeller and ship. It is not enough to know how the engine behaves alone. To get the correct system behavior one has to understand how the turbocharger works and the amount of air that it provides to the engine's cylinders for combustion. If turbocharger operation is incorrectly modeled, the amount of air in the cylinders is wrong and the modeled engine torque may be inexact due to incorrect air-to-fuel ratio and combustion efficiency. If the engine torque is erroneous, most likely the modeled engine speed is faulty. Thus, control of the real ship shaft speed will suffer. Focusing on torque production alone is, however, not sufficient to support decent control of the engine speed. One must also have knowledge of how the propeller is loaded during varying conditions, such as in inclement weather situations and in low-depth water. Moreover, this requires the knowledge of the propeller's speed of advance.

Since the propeller load is dependent on the square of the shaft speed the system can be seen as inherently stable and one may believe that overspeed of the engine does not occur. However, the propeller can experience sudden loss of torque. For instance, in big wave conditions torque loss is usual as a result of propeller emergence. If the engine is running at maximum speed a loss of load torque may lead to damaging overspeed of the engine. For this reason it is important to employ a robust speed controller for circumstances involving severe propeller load fluctuations, as during heavy weather and sea conditions.

Overspeed of the engine is regularly avoided by decreasing engine speed in situations of propeller load fluctuations. In order to retain a desired ship speed under such circumstances, engines are often oversized. This means that an engine larger than what is needed for normal operating conditions is fitted on the ship. With an oversized engine there is a power margin available to be used in these situations, and the overspeed problem is prevented. However, oversizing of engines increases fuel consumption, uses extra engine room space, runs at lower efficiency, increases pollutant emissions and leads to higher running and installation costs. Consequently, there are lots of benefits by being able to detect overload conditions and applying a robust controller to cope with this problem. The ultimate goal is to appropriately solve the control problem such that no engine oversizing or speed reduction is needed in harsh weather conditions.

1.2 Previous Work

This master's thesis is based on the project work [4] by the same author. In the project work an engine model for a two stroke marine diesel engine was developed. The model was a so-called *mean value engine model*, which means that it calculates the engine states based on average values over one engine cycle. The aim of the work was to develop a model that was as simple as possible, yet complex enough to capture the essential system properties. The model needed to represent the states and dynamics that is of interest to control. In addition to engine speed, control objectives could for instance be fuel consumption, transient air-to-fuel ratio and turbocharger speed.

A simple transfer function from fuel to engine speed does not have this capability. Moreover, an advanced three-dimensional simulation model becomes too complex, with numerous parameters to be fitted and a computational burden. The mean value model is an intermediate between these extremes, and a good choice as a controller basis.

In the mean value approach the fastest dynamics of the engine are neglected and the slowest dynamics are seen as constants. Mass and energy in the control volumes are considered homogeneous, i.e. perfectly mixed. An assumption is that the air and fuel flow is continuous, meaning the discrete nature of a real engine is simplified. As a consequence the independent variable is time, whereas crank-angle degree is needed for modeling discrete engine events.

The engine model was split into different subsystems as shown in Figure 1.1; the compressor, intake manifold, cylinders, exhaust manifold and turbine. Each part was modeled using physical principles, and information was exchanged between them with the means of flow of mass and energy.

Performance of the engine model was decent. The modeled turbocharger showed inadequate behavior, on the other hand. This was a result of compressor flow data not being available, leading to a generalized approach to compressor flow rate modeling. As a result, the intake and exhaust manifold pressures became unrealistically high and the air flow rate equally so. Consequently, the cylinder's supply of air was abundant and perfect combustion values were attained independent of the amount of injected fuel. Effectively this lead to the turbocharger dynamics being irrelevant for the engine's performance. For a real engine, the turbocharger time response is important for the engine's supply of air, and consequently the produced engine torque. This problem gives an incentive to model the compressor and turbine more accurately. Therefore the turbocharger will be thoroughly examined and modeled in this thesis to achieve reasonable overall engine performance.

Often, the encountered literature focuses on either torque production (engine/-turbocharger) or torque absorption (propeller/ship). Thus only covering one part of the problem of deciding engine speed. In sources where the engine and turbocharger is adequately described, the load is recurrently overlooked, or the pro-

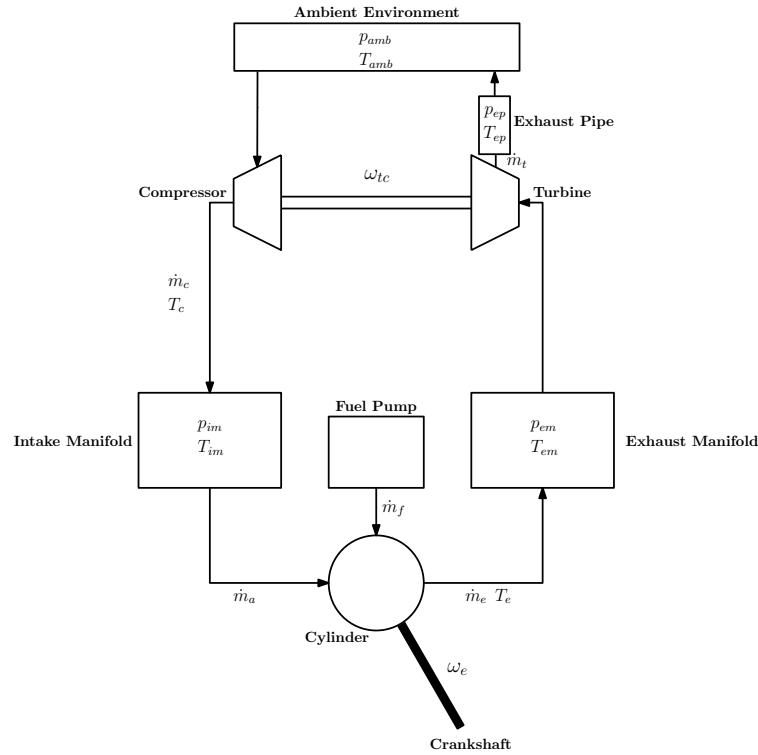


Figure 1.1: Engine modeling approach.

propeller is assumed to always match the theoretical propeller load curve. The propeller load curve, however, is only correct for a limited number of operating conditions, i.e. no hull fouling, no heavy weather, no large acceleration, no propeller losses. So the propeller curve approximation is too crude to represent a real operating condition. Literature regarding propeller modeling, on the other hand, rarely reflects over the system creating rotation of the propeller.

For this reason this thesis will serve as an important factor in collecting and consolidating the information from different literature and producing a reference for ship propulsion in total.

1.3 Research Objectives

The purpose of this thesis is to give an overview over the subject of ship propulsion modeling and to create a testing environment for controller design. The main objectives of the work are to:

1. Make a compressor and turbine model by map fitting.
2. Develop a propeller load model.

3. Extend the existing engine model by including an intercooler and overload protection.
4. Verify the performance of the engine and turbocharger through simulation.
5. Develop an engine speed PI controller with anti-windup capabilities.
6. Verify the speed controller, propeller model and ship model by simulation of the total ship propulsion system.

1.4 Thesis Outlines

- **Chapter 2:** Provides the necessary theoretical background for developing of a ship propulsion model by explanation of hull resistance, propeller properties and engine diagrams. A short introduction to turbocharger maps is given. Moreover, the chapter gives an introduction to the least squares method that is used for curve fitting of the turbocharger maps.
- **Chapter 3:** A compressor flow rate model is designed based on exponential functions. The new model's performance is compared with models from literatures. Additionally, the compressor efficiency is fitted to a manufacturer compressor map by the use of polynomials.
- **Chapter 4:** The deriving of a turbine flow model is performed, where parameters are fitted to a manufacturer turbine flow map. The chapter also produces a general purpose model for turbine efficiency as an efficiency map was not obtained.
- **Chapter 5:** Contains the development of the propeller load model. For the calculation of the propeller's speed of advance a ship surge model is also provided. Furthermore, the existing engine model is extended with an intercooler and overload protection.
- **Chapter 6:** The engine and turbocharger is simulated and the models verified. The nonlinear properties of the engine is investigated. Extrapolation capabilities of the turbocharger model is examined in addition to the influence of the overload protection fuel limiters.
- **Chapter 7:** Includes the development of a PI-controller with integrator anti-windup to cope with a limited fuel index. Also provides simulation of the total ship propulsion model with the speed controller enabled.

Chapter 2

Theory

The intricate process to be modeled requires some fundamental theory about ship propulsion. This chapter covers basic theory regarding ship propulsion, turbochargers and curve fitting to be used later in the thesis. First, ship propulsion is presented by discussing hull resistance, propeller characteristics, thrust losses and how these effects impact the engine by illustrating the engine layout and load diagrams. A short description of compressor and turbine maps follows. Lastly, an introduction to least squares curve fitting is undergone to illuminate how turbocharger map models are fitted.

2.1 Ship Propulsion

To control the revolutions of a marine diesel engine a general idea of how the propeller load acts should be in place. In a marine propulsion setting the engine power is used to rotate a propeller in water causing forward thrust. The water exerts a torque on the propeller as it rotates. What the engine torque and power output should be to maintain desired speed is better fathomed by having a good estimate on the propeller load. The propeller load is related to the propeller design, the ship load and the resistance the ship encounters. Furthermore, the resistance depends on the hull form and wear, as well as external forces such as wind, waves and currents. This section explains the basic principles of ship propulsion; including hull resistance, propeller operation and engine load diagrams.

2.1.1 Hull Resistance

The resistance of the hull is the sum of forces on the hull acting against the movement of the ship. The resistance forces reduce the effect of the forces created by the propulsion devices, hence reducing ship speed. To be able to make a good decision on what engine (power output) and propeller to embed on a ship, one should have an idea on what forces is working against its propulsion. The

resistance of the ship is mainly dependent on the speed of the vessel, as well as the displacement and hull form. A more streamlined body, for example, will create less resistance.

The total hull resistance consists of many source-resistances, they can in general be split in to three main categories

1. Frictional resistance
2. Residual resistance
3. Air resistance

Increased frictional and residual resistance comes from increased submergence of the hull. Nonetheless, not all frictional resistance is caused by water, the part of the ship structure above the waterline is affected by air resistance. More drag is however experienced beneath the water surface as water is more dense than air. Submergence of the hull is measured by the amount of water that the hull displaces, either as weight or volume, and is called the ship's displacement. Figure 2.1 shows some of the dimensions of a ship.

Frictional resistance (R_F) comes from hydrodynamic friction on the hull as the ship moves through the water. It increases approximately by the square of the ship speed. Fouling of the hull, i.e. degradation of the hull smoothness by erosion, growth of marine organisms and buckled bottom plates, will increase the frictional resistance. The friction force can be written as a function of the water density ρ_w , the hull's wetted (submerged) area S and the ship velocity V_s

$$R_F = 1/2 C_F \rho_w S V_s^2 \quad (2.1)$$

where C_F is the frictional resistance coefficient,

$$C_F = \frac{R_F}{1/2 \rho_w S V_s^2} = f(R_n) \quad (2.2)$$

that is mainly dependent on Reynolds number R_n [5, p.6]

$$R_n := VL/v \quad (2.3)$$

Residual resistance includes the wave (R_W) and eddy resistances (R_E). Wave resistance is the energy lost due to generating waves as the ship interacts with the water. Moreover, the swirling of water and reverse current created when a ship moves through a viscous fluid, particularly at the aft of the ship, is called the eddy resistance. This effect can often be observed behind large rocks in rapid rivers, for example. The residual resistance can be written as

$$R_R = 1/2 C_R \rho_w S V_s^2 \quad (2.4)$$

where C_R is the residual resistance coefficient, and depends on the Froude number F_n [5, p.5]

$$C_R = \frac{R_R}{\frac{1}{2}\rho_w S V_s^2} = f(F_n) \quad (2.5)$$

$$F_n := \frac{V_s}{\sqrt{gL}} \quad (2.6)$$

$$(2.7)$$

where L is the overall submerged length of the craft and g is the acceleration of gravity.

Remark 2.1. *At low speeds the wave resistance is approximately proportional to the square of the speed. For high speeds, however, the wave resistance grows much faster. The dominating resistance form for low speed ships is therefore frictional resistance, whereas wave friction is dominating for high speed. As a result of the rapid increase of wave friction at high speeds, a given hull design meets a “wave wall” when a further increase in propulsion power results in only a minor increase in ship speed, as most of the extra power is converted into wave energy [1].*

Air resistance (R_A) comes from the motion of the ship through air, and usually accounts for only a small part of the total resistance. Ships with a large superstructure or container ships will naturally have a higher air resistance than some other ship types resulting from a large wind exposed area. The following equation can be used for air resistance [1, p.11]

$$R_A = \frac{1}{2} 0.9 \rho_a A_T V_a^2 \quad (2.8)$$

where ρ_a is the density of air, A_T the cross-sectional area of the ship above the water and V_a the wind velocity.

The *total resistance* (R_T) on the ship is sometimes referred to as the total ship towing resistance (Figure 2.2), as it corresponds to the total force at given a speed (power) needed to tow the ship in smooth water.

$$R_T = R_F + R_W + R_E + R_A \quad (2.9)$$

In addition to depending on the fouling state and displacement variations of the ship, the total resistance also depends on the sea state and water depth. Strong wind, currents and big waves are sources of increased resistance. For instance, navigating in head-on seas will increase the resistance drastically compared to calm weather conditions. Shallow waters have the effect that the displaced water underneath the ship will have more difficulty in moving aft-wards, creating higher residual resistance. Sometimes it is usual to leave an engine power margin available for an increase in resistance as a consequence of bad weather, this is referred to as a *sea margin*.

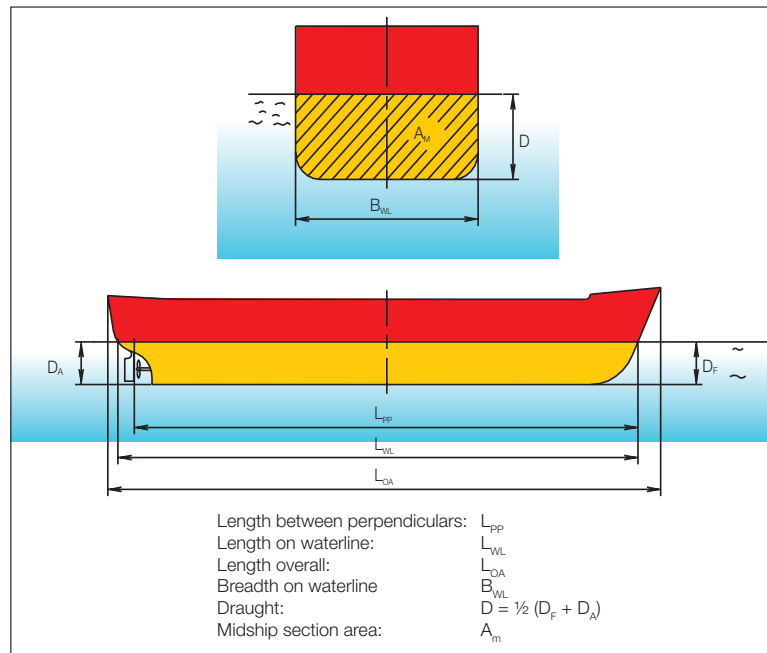


Figure 2.1: Ship hull dimensions [1].

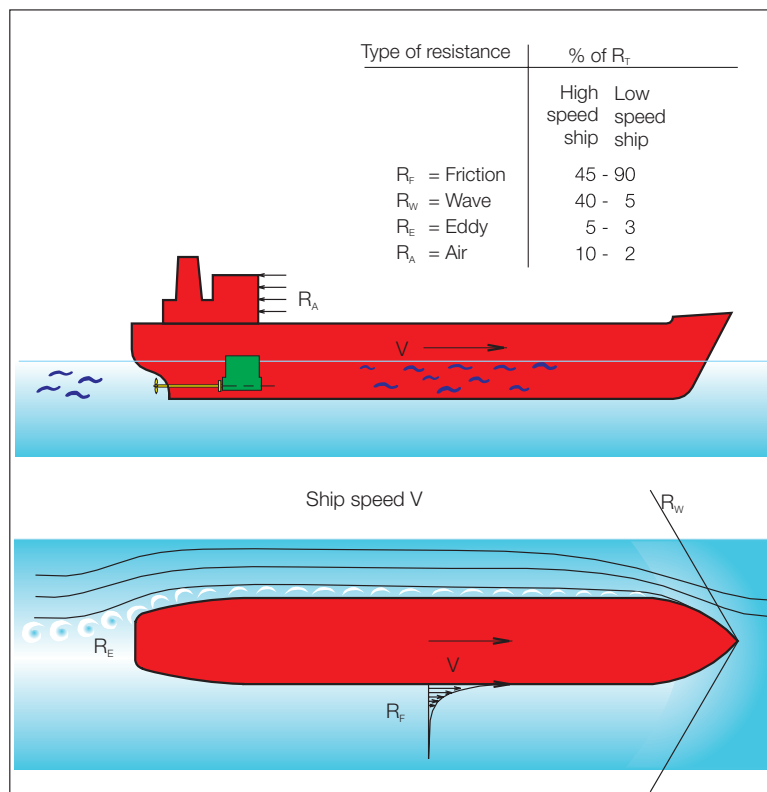


Figure 2.2: Total ship towing resistance $R_T = R_F + R_W + R_E + R_A$ [1].

Not only is the hull surface fouling, but the propeller surface will also become rough and fouled leading to thrust loss. The total resistance increase caused by fouling may be in the region of 25-50% throughout the lifetime of a ship [1]. Increased resistance will result in a greater need for propulsion power, or consequently a loss of speed. For this reason, engines installed on new ships are often overpowered to account for future fouling of the hull and propeller.

The effective power P_E required to move the ship through water at the current ship speed is

$$P_E = V_s R_T \quad (2.10)$$

2.1.2 Propeller Propulsion

The objective of a propeller is to translate rotational power from the engine to thrust moving the ship forward. Conventionally, the propeller's thrust and torque characteristics are found from tests in water tanks. As the propellers usually are fitted on the stern of a ship, the performance will be influenced by varying water conditions generated by the hull and weather conditions.

Propeller Pitch

The propeller can either be a fixed pitch propeller (FPP) or a controllable pitch propeller (CPP). The FPP has a fixed orientation of the propeller blades, while the CPP has hydraulic control of the pitch of the blades.

The propeller pitch is defined as the distance traveled per revolution when advancing the propeller as a screw with screw angle equal to the blade angle at $0.7R$ (providing there is no slip) [6]. The pitch can vary along the blade's radius so the ratio is normally related to the pitch at $0.7R$, where R is the blade's radius. See Figure 2.4 for an illustration of the pitch.

For a CPP the propeller performance curve can be altered by controlling the pitch of the blades. The FPP, by contrast, follows the physical laws and the propeller curve can not be altered. Ships without need for good maneuverability are usually equipped with the FPP, as it is less expensive and the smaller hub (CPP must fit the actuation mechanism) gives a slightly better efficiency. Additionally, as the CPP is more complicated it leads to a higher risk of problems in service.

Remark 2.2. *For simplicity this thesis will only consider FP-propellers. Extensions to CP-propellers can, nonetheless, easily be done.*

Propeller Characteristics

The propeller thrust force T_p and torque Q_p can be found as function of the shaft speed (n) (in revolutions-per-second), the propeller diameter (D) and the water

density (ρ_w) [7]

$$T_p = K_T \rho_w D^4 n^2 \quad (2.11)$$

$$Q_p = K_Q \rho_w D^5 n^2 \quad (2.12)$$

K_T and K_Q are the dimensionless thrust and torque coefficients [8]

$$K_T = f_1(J_a, P/D, A_E/A_O, Z, R_n, t/c) \quad (2.13)$$

$$K_Q = f_2(J_a, P/D, A_E/A_O, Z, R_n, t/c) \quad (2.14)$$

which are dependent on the advance ratio (J_a), the Reynolds number (R_n) and various geometric properties of the propeller; the pitch to diameter ratio (P/D), blade area ratio (A_E/A_O), the number of propeller blades (Z) and the ratio of the maximum propeller blade thickness to the length of the cord (t/c). The propeller consumed power is

$$P_p = 2\pi n Q_p = 2\pi K_Q \rho_w D^5 n^3 \quad (2.15)$$

The expressions for K_T and K_Q are found from *open water tests*, meaning they are found from tests in water tanks without a ship hull involved. The thrust and torque coefficients are estimated for a deeply submerged propeller subject to an in-line inflow.

The advance ratio J_a is a dimensionless expression of the propeller's speed of advance V_a . Speed of advance is essentially the same as the inflow velocity to the propeller.

$$J_a = \frac{V_a}{nD} \quad (2.16)$$

The corresponding open-water efficiency η_0 is given as the ratio between delivered thrust power P_T and the mechanical rotational power provided to the propeller by the shaft P_D .

$$\eta_o = \frac{P_T}{P_D} = \frac{T_p V_a}{2\pi n Q_p} = \frac{K_T J_a}{K_Q 2\pi} \quad (2.17)$$

An example of propeller open water characteristics is shown in Figure 5.3 on page 60.

Propeller-Hull Interaction

Installing the propeller on a hull of a ship will cause the propeller characteristics to deviate from its open water characteristics. The open-water relations between thrust, torque and propeller revolutions can not be assumed when variable flow conditions occur due to interactions with the hull.

When a ship moves through water friction of the hull will drag water along with the ship's motion, therefore water around the stern will acquire speed in the same direction as the ship moves. This forward-moving water is called *wake*. In addition to wake from friction, the ship makes wake waves because of displacing

water. The effect of the wake is that the propeller flow field is not homogeneous. The wake velocity V_w has the same direction as the ship's speed V_s . In propeller calculations we are often interested in the velocity of the arriving water at the propeller V_a , called the advance speed of the propeller

$$V_a = V_s - V_w \quad (2.18)$$

which is the average velocity of water arriving over the propeller disc. It can also be written by the help of Taylor's wake fraction number w [7, p.67]

$$w := \frac{V_w}{V_s} = \frac{V_s - V_a}{V_s} = 1 - \frac{V_a}{V_s} \quad (2.19)$$

Normally $w \in [0.20, 0.45]$ for a single propeller ship [9]. The advance speed can then be written as

$$V_a = (1 - w)V_s \quad (2.20)$$

The wake field is dependent on the form of the hull, therefore the same propeller will perform differently behind individual ships. The wake field will also increase with fouling of the hull, as the hull's surface gets more rough and the flow field less homogeneous. Moreover, the location and size of the propeller also influence the wake field it operates in.

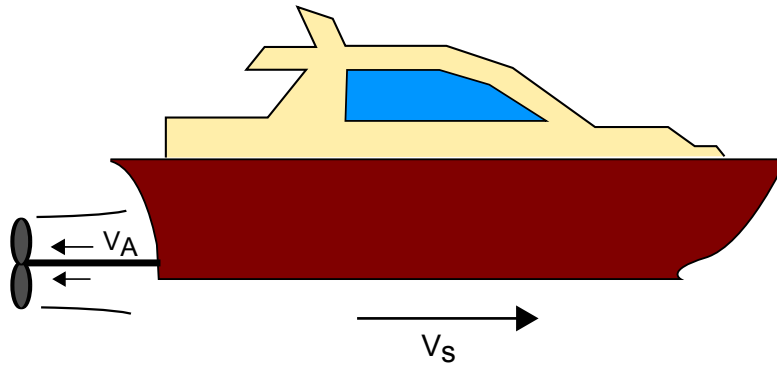


Figure 2.3: Definition of speed of advance V_a and ship speed V_s .

On the whole, to find the propeller characteristics independent of the ship, it is necessary to make the propeller work in a homogeneous wake field undisturbed by the hull, in so-called open water. The open water characteristics refers to the thrust, torque and efficiency produced given the speed of advance and rate of revolution in open water, as opposed to the behind-hull properties.

When the propeller produces thrust it sucks water back along the hull, altering the pressure and velocity distributions around the hull, resulting in extra resistance. Consequently the required thrust to maintain ship speed exceeds the total

towing resistance by an increased friction force F . This augmented thrust loss is introduced via the thrust deduction coefficient t_d

$$t_d = \frac{F}{T_p} \Leftrightarrow F = t_d T_p \quad (2.21)$$

which is normally in the range of 0.12-0.30 for a ship with one propeller, and increases with increasing wake [1]. Thrust loss can be reduced by designing the hull in a proper form.

The torque coefficient for the propeller behind the hull (K_{QB}) will be reduced in comparison to the open water torque coefficient. The thrust coefficient, on the other hand, is normally assumed to remain unchanged [6]. If thrust remains the same and absorbed torque behind the ship is Q_B , the efficiency behind the ship becomes

$$\eta_B = \frac{T_p V_a}{2\pi n Q_B} \quad (2.22)$$

So the *relative rotative efficiency* can be found as the ratio of the behind ship efficiency to the open water efficiency

$$\eta_R = \frac{\eta_B}{\eta_0} = \frac{K_Q}{K_{QB}} = \frac{Q_p}{Q_B} \quad (2.23)$$

lying between 1.0 and 1.1 for most single screw ships [10], but usually quite close to 1.

Thrust Losses

The ideal conditions for a propeller is when it is deeply submerged and in calm water. Nonetheless, effects that introduce thrust losses to the propeller often come about. The losses can be divided into losses that mainly affect the propeller loading, which includes fluctuations of the in-line water inflow, ventilation and in-and-out-of-water effects. Losses that affect the propeller wake includes transverse water inflow and thruster-hull interaction. Another loss effect that does not involve single propeller ships is thruster-thruster interaction.

- In-line velocity fluctuations occur as a result of the vessel motion, waves and currents creating a time-varying velocity field around the propeller. The changes in the in-line (axial) flow component induces changes in the advance velocity and consequently the K_T and K_Q coefficients, leading to thrust and torque losses. The water flow to the propeller is not constant nor at an optimal in-line angle.
- Ventilation (air suction) may occur when the propeller is heavily loaded and in high waves, during reduced propeller submergence. Low pressure on the propeller causes air being drawn in from the free surface, creating a less optimal propeller environment. A fully ventilated propeller may lose as much as 70-80% of its thrust and torque [11].

- In-and-out-of-water effects is the emergence of the propeller in extreme weather conditions, causing sudden loss of load torque and may result in propeller racing and critical engine overspeed, moreover reducing thrust.

Propeller cavitation is the formation and immediate implosion of cavities in the water caused by rapid changes of pressure. Cavitation causes small liquid-free zones, like bubbles, that can damage the propeller and reduces the propulsion efficiency. The risk of propeller cavitation is increased by more inhomogeneous propeller conditions (higher wake velocity) [1]. Cavitation is closely related to ventilation.

The optimum propeller speed depends on the number of propeller blades and the diameter of the propeller. Generally, the more blades and the larger the blades, the lower the optimal speed is. Additionally, the larger the blades and the less number of blades the propeller has, the higher efficiency it can achieve. However, when using a larger propeller, there is a bigger risk of out-of-water effects and ventilation. Furthermore, an engine capable of running low speeds must be installed, in addition to sufficient space on the hull for larger blades.

Slip

An indication to how much load is applied to the propeller can be found from the propeller slip. If the propeller operates in an unyielding medium, like a screw in a wall, the forward velocity of the propeller V would be decided by the geometric pitch P and the angular velocity n in the following manner

$$V = Pn \quad (2.24)$$

Unlike the screw, a propeller does not operate in a solid material. The propeller will move through water and accelerate it backwards, causing a slip. The slip is the difference between the speed the propeller would travel in a solid material and the speed it travels in the water, also called the advance speed V_a . The slip becomes $Pn - V_a$, and the slip ratio is defined as

$$S_R := \frac{Pn - V_a}{Pn} = 1 - \frac{(1 - w)V_s}{Pn} \quad (2.25)$$

Slip is illustrated in Figure 2.4. When the propeller is heavily loaded (increased resistance), e.g. sailing against wind or waves, in shallow waters, with a fouled hull, with a heavily loaded ship or when accelerating, the slip will increase. For this reason, propeller speed has to be increased to maintain the required ship velocity.

2.1.3 Engine Layout and Load Diagrams

To match the engine and propeller to the ship it is important to sketch the expected propeller load curves with the power and speed restrictions of the engine. The

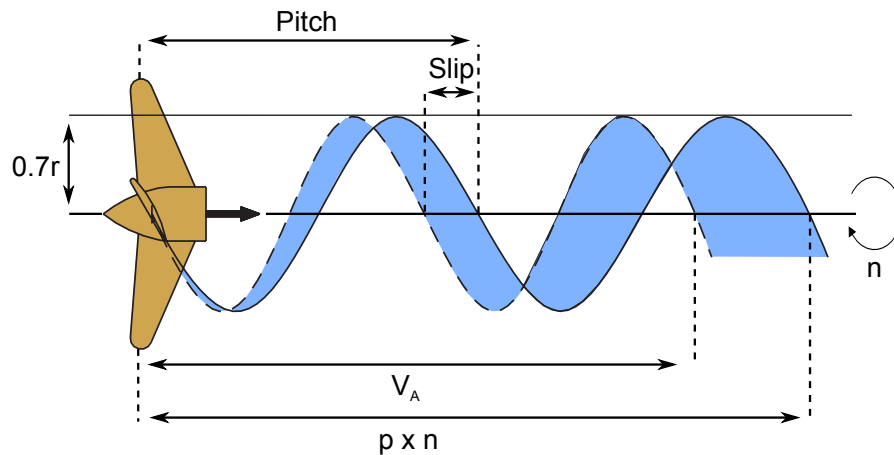


Figure 2.4: Illustration of propeller pitch and slip.

engine layout and load diagrams are composed in logarithmic scale to achieve simple diagrams with straight lines.

The brake power of the engine P_b is proportional to the brake mean effective pressure \bar{p}_b and engine speed n , see [4]

$$P_b = c\bar{p}_b n \quad (2.26)$$

and c is a proportionality constant. The propeller consumed power is a function of the shaft speed cubed, see (2.15), so the engine brake power can be written as

$$P_b = cn^3 \quad (2.27)$$

On a logarithmic load diagram this gives that lines of constant brake mean effective pressure has slopes of 1, and constant lines of power has slope 3.

Engine Layout Diagram

The engine layout diagram is a diagram showing the operating region for an engine. Referring to Figure 2.5, the propeller design point (PD) is the combination of power and speed for the engine that is optimum for the projected ship and expected operating profile. The design point is on a so-called *light running propeller curve*, which represents a ship with clean hull and in good weather. To include the fact that bad weather is encountered, an alternative propeller design point (PD') is occasionally used instead.

An extra power margin (sea margin) is often incorporated to cope with conditions of strong currents, wind and waves where extra ship resistance is met. The speed and power combination after adding the sea margin, is called the continuous service point (SP), and is found on the *heavy running propeller curve*. This is where the engine/propeller is assumed to be working for the majority of time.

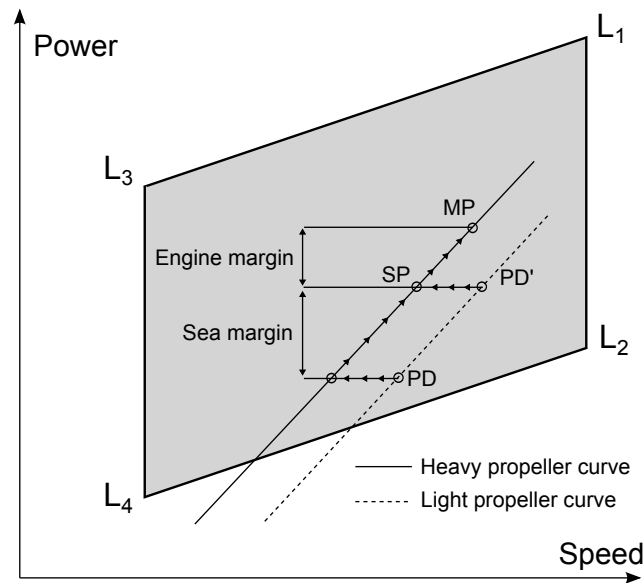


Figure 2.5: Ship propulsion running points and engine layout. (PD) Propeller design point, (PD') Alternative propeller design point, (SP) Service propulsion point, (MP) Specified propulsion point.

In addition to the extra resistance as a result of bad weather, fouling of the hull with time will promote a heavier running propeller curve. For this reason an extra engine margin is often added as an operational margin in addition to the sea margin. The new operational point (MP) is called the specified MCR for propulsion.

The engine limitations on the diagram are the two lines representing mean effective pressure (L_1-L_3 and L_2-L_4) and engine speed (L_1-L_2 and L_3-L_4). Point L_1 on the diagram is the engine's point of maximum continuous rating, *MCR*, which is the maximum power and speed the engine is capable of running for longer periods of time. The specified MCR is the maximum rating required by the yard or owner for continuous operation of the chosen engine, and can be freely chosen within the boundaries of the engine layout diagram. If it does not fit inside the boundaries of the current engine another main engine type or propeller speed will have to be chosen.

Remark 2.3. *The engine can produce higher power/speed outputs than MCR, by roughly 10%. Operating the engine above this limit for long periods of time will cause excessive wear on the engine and drastically reduce its service life time.*

Remark 2.4. *The optimal specific fuel consumption is usually in the region 70-80% of the the engine's nominal MCR (L_1).*

Engine Load Diagram

The engine load diagram defines the power and speed limits as well as overloaded operation of the engine. The diagram shows the allowed operational region of the engine and the expected load by the propeller. Figure 2.6 show an engine load diagram.

Electronic governors¹ used in diesel engines protect the engine from thermal and mechanical overload by including a scavenge air pressure limiter and a torque limiter. The scavenge air pressure limiter ensures that enough air is fed to the cylinders during acceleration to provide a perfect combustion. This is done by limiting the amount of fuel administered if the scavenge air pressure is too low. Engine mechanical overload is averted by limiting the injected fuel according to the current engine speed, this is done by the torque limiter. The torque limiter is shown as line 4 in Figure 2.6, the scavenge limiter on is not illustrated in the figure.

A heavily loaded propeller will shift the load line towards the left of the diagram. In light running conditions, on the other hand, the shift is towards right.

Remark 2.5. *Mean effective pressure is proportional to the fuel index. Then lines of mean effective pressure is also an indication of the corresponding fuel index.*

Remark 2.6. *The specified MCR of the engine can usually be exceeded by more than the typical 10% overload limit. It is the limits according to the nominal MCR speed and power that should not be surpassed. It is still considered overloading, nonetheless. Additionally the torsional vibration limits must not be exceeded.*

2.2 Turbocharger Maps

A turbocharger consist of a compressor and a turbine connected on a common shaft. The compressor's task is to lead air from outside the engine to the intake manifold, and at the same time increase its pressure and density. Increased air density in the combustion cylinders means that more oxygen is able to fit in the limited cylinder space, leading to the ability of efficiently burning more fuel.

The turbine is the component between the exhaust manifold and the outside of the engine. The exhaust gas energy provides power to the turbine making the common shaft rotate. Generally, the faster the turbocharger rotates, the more air is drawn into the cylinders from the compressor.

Turbocharger performance is usually described by experimental maps supplied by the turbocharger manufacturer. This section gives a brief introduction to compressor maps and turbine characteristics. Some information is excluded as explanation of turbocharger modeling and maps is contained in the earlier project work [4].

¹A governor is a device used to measure and regulate the speed of a machine

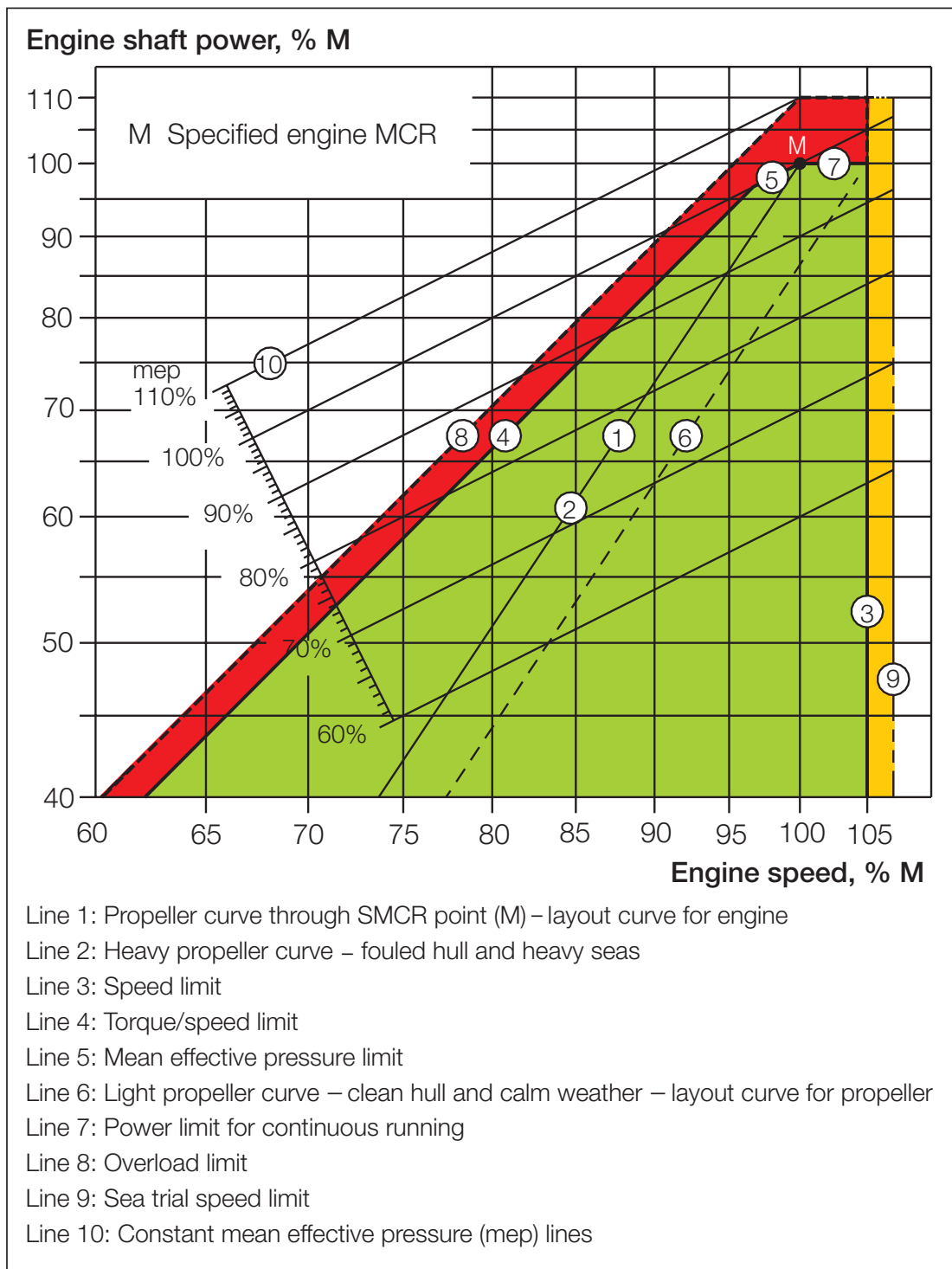


Figure 2.6: Engine load diagram [1].

2.2.1 Compressor

A conceptual compressor map is shown in Figure 2.7. The four performance variables of the compressor map are mass flow rate \dot{m}_c , pressure ratio Π_c , turbocharger shaft speed N_{tc} and the adiabatic efficiency η_c . As an alternative to the mass flow rate, occasionally volume flow rate is used. Flow rate and speed are often provided in *corrected quantities*. The purpose of using corrected quantities is to make the performance map valid for other conditions than the particular testing conditions, i.e. the temperature and pressure during performance tests. The corrected values scales the performance variables based on current ambient temperature T_{amb} and pressure p_{amb} . Corrected mass flow rate is given as

$$\dot{m}_{c,corr} = \dot{m}_c \frac{\sqrt{\frac{T_{amb}}{T_{amb,0}}}}{\frac{p_{amb}}{p_{amb,0}}} \quad (2.28)$$

where $T_{amb,0}$ and $p_{amb,0}$ indicate the ambient temperature and pressure during testing of the compressor. Corrected shaft speed is

$$N_{tc,corr} = N_{tc} \frac{1}{\sqrt{\frac{T_{amb}}{T_{amb,0}}}} \quad (2.29)$$

Compressor pressure ratio is the relationship between the intake manifold pressure and the ambient pressure

$$\Pi_c = \frac{p_{im}}{p_{amb}} \quad (2.30)$$

The isentropic efficiency is the ratio between the ideal enthalpy change across the compressor and the real enthalpy change. The real enthalpy change is larger due to losses, e.g. heat loss.

$$\eta_c = \frac{\Delta h_{ideal}}{\Delta h} = \frac{\text{work into ideal compressor}}{\text{work into actual compressor}} \in [0, 1] \quad (2.31)$$

The two axes on the compressor diagram are the corrected mass flow rate and pressure ratio. Curves of constant corrected turbocharger speed is shown in the diagram, as well as contours for constant compressor efficiency.

The curves of constant speed span the region between the *surge line* and the *choke line*. Surge is the highest pressure and lowest mass flow achievable for each constant speed. If the surge line is crossed there is a complete loss of compression, resulting in a reversal of flow. Consequently, instability and large flow fluctuations occurs. Surge is characterized by cyclic periods of backflow through the compressor.

Choking is the rightmost point of the speed curve. If the flow is choked, a further reduction of pressure ratio will not increase the flow. This is a consequence of the flow speed reaching supersonic conditions at some cross-section in the compressor. At this point the slope of the pressure becomes infinite.

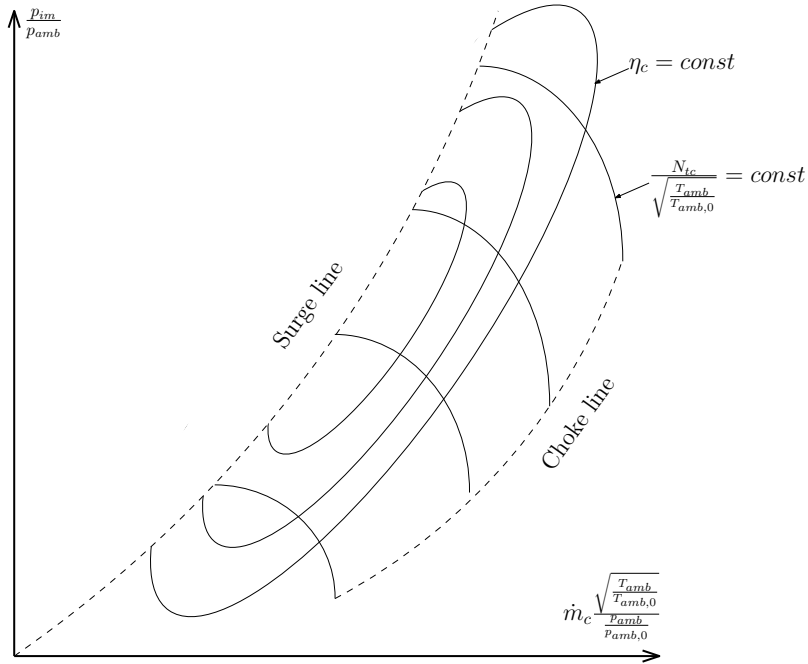


Figure 2.7: Conceptual compressor performance map.

2.2.2 Turbine

Flow through a turbine can be found from the pressure p_{em} and temperature T_{em} in the exhaust manifold, or more specifically, on the inlet to the turbine. An example of a turbine flow characteristic is seen in Figure 2.8. Instead of using the corrected turbine mass flow rate

$$\dot{m}_{t,corr} = \dot{m}_t \frac{\sqrt{\frac{T_{em}}{T_{em,0}}}}{\frac{p_{em}}{p_{em,0}}} \quad (2.32)$$

the reduced turbine flow parameter is commonly adopted

$$\dot{m}_{t,red} = \dot{m}_t \frac{\sqrt{T_{em}}}{p_{em}} \text{ [kg}\sqrt{\text{K}}/(\text{s Pa})] \quad (2.33)$$

The corrected shaft speed

$$N_{tc,corr} = N_{tc} \frac{1}{\sqrt{\frac{T_{em}}{T_{em,0}}}} \quad (2.34)$$

is usually exchanged with the reduced turbine speed parameter

$$N_{tc,red} = N_{tc} \frac{1}{\sqrt{T_{em}}} \text{ [(r/min)/}\sqrt{\text{K}}] \quad (2.35)$$

Lastly, the turbine expansion ratio is given by

$$\Pi_t = \frac{p_{em}}{p_{ep}} \quad (2.36)$$

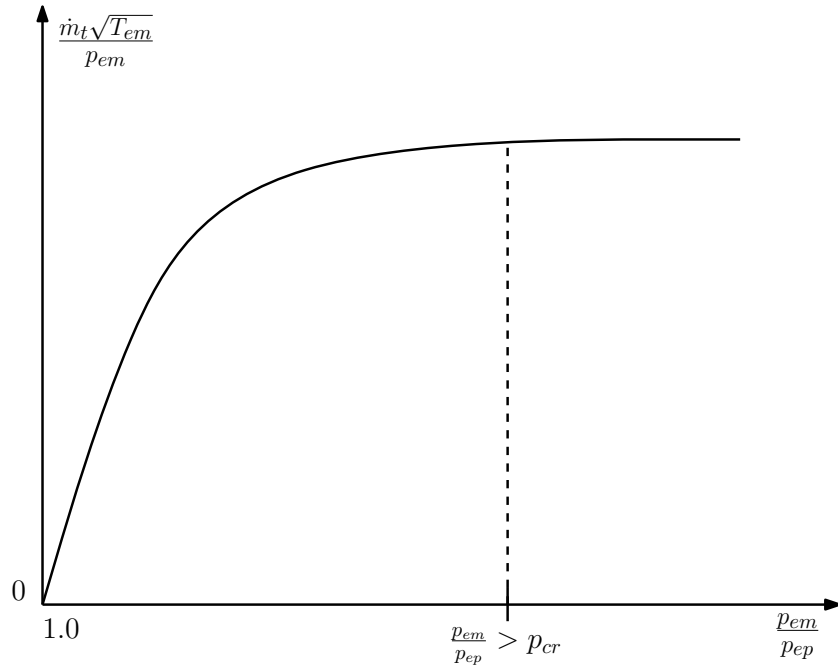


Figure 2.8: Conceptual turbine flow rate map.

where p_{ep} is the pressure in the exhaust pipe on the outlet from the turbocharger. Sometimes the ambient pressure p_{amb} is used if the exhaust pipe pressure is unknown. The turbine flow exhibits choked properties as well.

2.3 Least Squares Curve Fitting

The least squares method is a popular approach to fit parameters of a function to a set of measured data. The method is used several times in the thesis and an explanatory introduction to the behavior of the algorithm is given here. The curve fit is done such that the estimated parameters give the least squared error between the measured data and the model. To apply the least squares method the system should be *overdetermined*, i.e. there are more measurements than unknown parameters. Let x be the independent variable and let $f(x)$ denote the unknown function of x that we want to approximate.

$$y = f(x) \tag{2.37}$$

Given a set of n input data x_1, \dots, x_n , the i -th output is

$$y_i = f(x_i), \quad i = 1, \dots, n \tag{2.38}$$

With the parameters θ , the estimate of the function is

$$\hat{y}_i = f(x_i, \theta) \tag{2.39}$$

The corresponding estimation error is

$$e_i = y_i - \hat{y}_i \quad (2.40)$$

The least squares cost criterion is given as the square of the estimation error

$$J = \sum_{i=1}^n e_i^2 = \sum_{i=1}^n (y_i - f(x_i, \theta))^2 \quad (2.41)$$

We want to find the parameters θ that minimize this cost criterion

$$\hat{\theta} = \arg \min_{\theta} J(\theta) = \arg \min_{\theta} \sum_{i=1}^n (y_i - f(x_i, \theta))^2 \quad (2.42)$$

This is achieved by setting $\frac{\partial J}{\partial \theta} = 0$, which gives

$$-\sum_{i=1}^n 2(y_i - f(x_i, \theta)) \frac{\partial f(x_i, \theta)}{\partial \theta} = 0 \quad (2.43)$$

$$\Downarrow$$

$$\sum_{i=1}^n y_i \frac{\partial f(x_i, \theta)}{\partial \theta} = \sum_{i=1}^n f(x_i, \theta) \frac{\partial f(x_i, \theta)}{\partial \theta} \quad (2.44)$$

If the function $f(x, \theta)$ is linear in its parameters (not necessarily in x) the equation (2.44) can be solved analytically. If, on the other hand, the problem is nonlinear it is usually solved by iterative refinement. This is for example done by the use of Gauss-Newton method or the Levenberg-Marquardt algorithm. See [12, 13] for further information on least squares and solution methods.

One drawback of using the squared error is that outliers is given a disproportionately large weighting. A choice of minimizing the *unsquared* sum of deviations might seem like a more appropriate choice. The use of absolute values, however, make the derivatives discontinuous and they cannot be treated analytically.

Example 2.1 (Linear Least Squares). *A set of samples (x, y) is given in Figure 2.9. The samples seem to follow a curve similar to*

$$f(x, \theta) = a + bx + cx^2 \quad (2.45)$$

The function is linear in its parameters and can therefore be written as

$$f(x, \boldsymbol{\theta}) = \begin{bmatrix} a & b & c \end{bmatrix} \begin{bmatrix} 1 \\ x \\ x^2 \end{bmatrix} = \boldsymbol{\theta}^T \boldsymbol{\phi}(x) \quad (2.46)$$

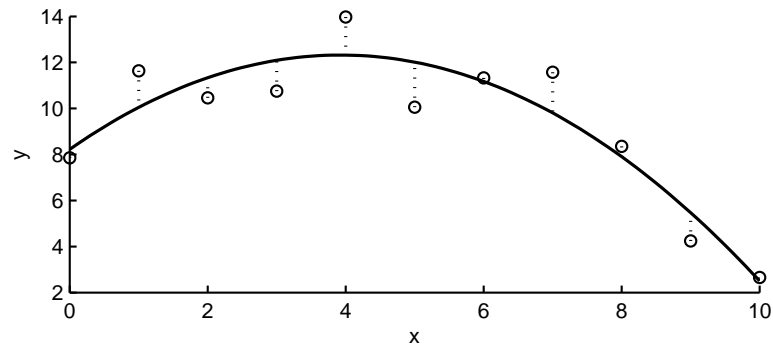


Figure 2.9: Samples (circle), the least squares curve fit (solid) and the vertical deviations (dotted).

where $\boldsymbol{\theta}$ is the vector of parameters and $\boldsymbol{\phi}$ is the regressor. Using (2.44) we find the least square parameters $\hat{\boldsymbol{\theta}}$ as

$$\sum_{i=1}^n y_i \boldsymbol{\phi}(x_i) = \sum_{i=1}^n \boldsymbol{\phi}(x_i) \boldsymbol{\phi}(x_i)^T \boldsymbol{\theta} \quad (2.47)$$

\Downarrow

$$\hat{\boldsymbol{\theta}} = \left(\sum_{i=1}^n \boldsymbol{\phi}(x_i) \boldsymbol{\phi}(x_i)^T \right)^{-1} \sum_{i=1}^n y_i \boldsymbol{\phi}(x_i) \quad (2.48)$$

In this particular case, giving the optimized function

$$\hat{y} = 6.59 + 2.54x - 0.32x^2 \quad (2.49)$$

Chapter 3

Compressor Map Modeling

For the reason that the turbocharger model partly failed in the project work, a compressor map has been acquired and this chapter demonstrates how to incorporate the map into the engine simulation model. Surely it is imperative to have a precise turbocharger model so that the correct amount of air is induced to the engine and consequently the correct engine torque is produced. An accurate turbocharger model may be used for applications such as transient air-to-fuel ratio control and control of turbocharger speed by the use of wastegate and variable area turbine. Furthermore pollutants may be reduced by feeding some of the exhaust back in the intake manifold by the use of exhaust gas recirculation control.

The compressor map is usually generated based on compressor rig test results. The physical processes in the turbocharger are complicated. Obtaining perfect models representing this operation is difficult or even impossible. A very precise model is often too complex to be evaluated efficiently and numerous, often difficult obtainable, parameters must be found. An overview on how the variables relate are found by measuring the variables of interest during the test and plotting them together in a compressor map. *Interpolation*-methods can then be used to estimate the unknown regions amidst the measurements, although quite general and perhaps wrongfully. Another possibility is to make simple functional relationships (models) by observing the connection between variables and trying to see the general guidelines, thereon adapting the model parameters to fit the measured data. Both approaches are put to use in this chapter.

A compressor map for a *MAN Diesel & Turbo TCA55*-turbocharger is shown in Figure A.1 on page 98. The unknown compressor map variables from the engine model are air flow rate and efficiency. Accordingly, the supplied compressor map is used to determine the air volume flow rate Q_c [m³/s] given the known pressure ratio Π_c over the compressor and the speed of the turbocharger N_{tc} [r/min]. Moreover, the compressor efficiency η_c , which was considered a constant, is also found from the information in the map. Several samples are collected from the supplied compressor map to regenerate the map in the simulation software.

The chapter starts by reproducing the flow rate with interpolation of samples

from curves of constant turbocharger speed. Following is the development of two flow models based on exponential functions. Thereafter a commonly used model is presented and various arguments in favor of and against the different approaches are discussed. Finally, the efficiency contours are fitted by the use of polynomials.

3.1 Flow Rate Interpolation

Interpolation is the method of constructing new data points within the range of a set of discrete samples. Considering that only a finite number of samples can be taken from a distinct compressor map, a method of reproducing the regions between those samples must be employed. Interpolation methods make educated guesses of the functional value for an intermediate input. *Linear* interpolation is commonly practiced in cases where precision is not crucial, for the reason of being the simplest and computationally fastest. In linear interpolation the unknown regions between each sample are described by straight lines, see Figure 3.1. A disadvantage with the straight line approach is that it is discontinuous at each sample, often a smooth interpolating function is desirable.

Due to the flow through the compressor being nonlinear (e.g. the constant speed curves are bent, and the shape of the curve differs from one speed to another) achieving satisfactory performance is done either by taking an abundance of samples for the linear method, or applying a nonlinear interpolation method. *Piecewise cubic Hermite* interpolation utilizes an approximation to the derivative of the function at the samples, hence giving a better approximation of the real function (normally). For other interpolation methods, e.g. splines and Gaussian processes consult [14, 15].

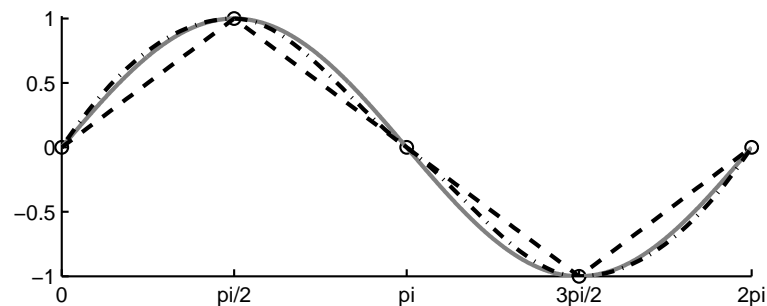


Figure 3.1: Linear interpolation (dashed) and piecewise cubic Hermit interpolation (dash-dot) of the nonlinear function $y = \sin x$ (solid).

To reproduce the constant speed curves the Hermite interpolation method is utilized on the samples (Figure 3.3). By setting the ambient temperature to the same as the compressor map reference temperature ($T_{\text{amb},0} = 293.2\text{K}$), having to correct the modeled flow due to temperature differences is avoided. The ambient pressure is assumed at the atmospheric value.

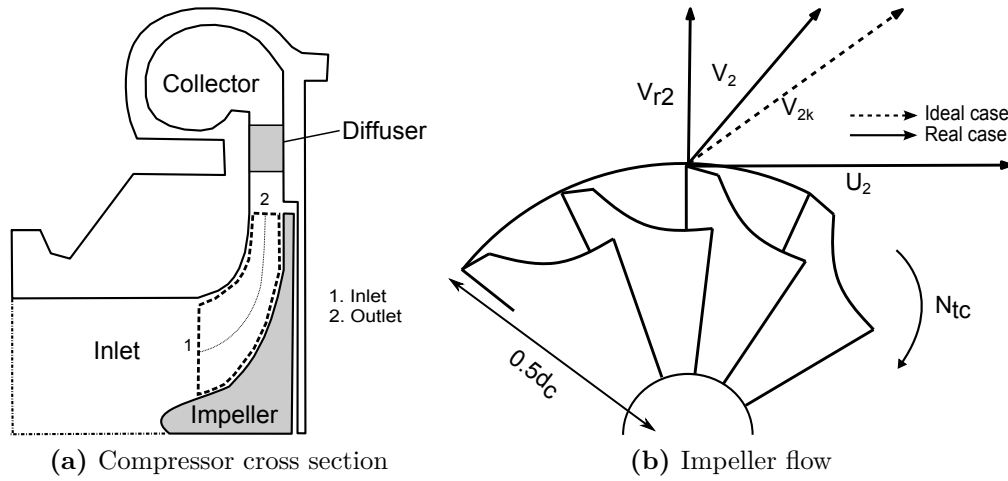


Figure 3.2: Cross section of a centrifugal compressor (a) showing the impeller and diffuser. The compressor impeller (b) showing ideal air flow velocity (V_2), real air flow velocity (V_{2k}) and blade tip speed (U_2).

Instead of supplying the constant speed curves by corrected speed, they are given by the compressor *blade tip speed*

$$U_c = \frac{\pi}{60} d_c N_{tc} \text{ [m/s]} \quad (3.1)$$

where N_{tc} is the turbocharger speed [r/min] and d_c is the compressor diameter [m]. The air flow through the compressor is as follows (Figure 3.2); air is available in the *inlet*. The rotating turbocharger shaft induce air to the connected *impeller*. The velocity of the air at the inlet (V_1) is increased through the impeller as the rotating shaft and the geometry of the impeller forces the flow to spin faster and faster. At the impeller exit the air velocity is V_2 . The tangential speed of impeller blades are different for the inlet (U_1) and exit (U_2) due to the impeller blade design (the radius changes along the flow path). The increase in flow velocity results in a rise of kinetic energy. This kinetic energy is converted to a static pressure increase (potential energy) as the flow is gradually slowed (diffused) through the *diffuser*. The *collector* gathers the flow from the diffuser and delivers to a downstream pipe.

Remark 3.1. *The symbols U_c and U_2 are used interchangeably for the compressor blade tip speed throughout the thesis. This is due to U_2 being used in the compressor map and flow descriptions, whilst the subscript c indicates compressor.*

For a given speed, the compressor flow rate may be decided by interpolation with pressure ratio as the independent variable. However, during simulation the speed is at no time the exact same value as one of the provided speeds. As a result, the regions between every supplied speed curve is unknown. Seeing as there are

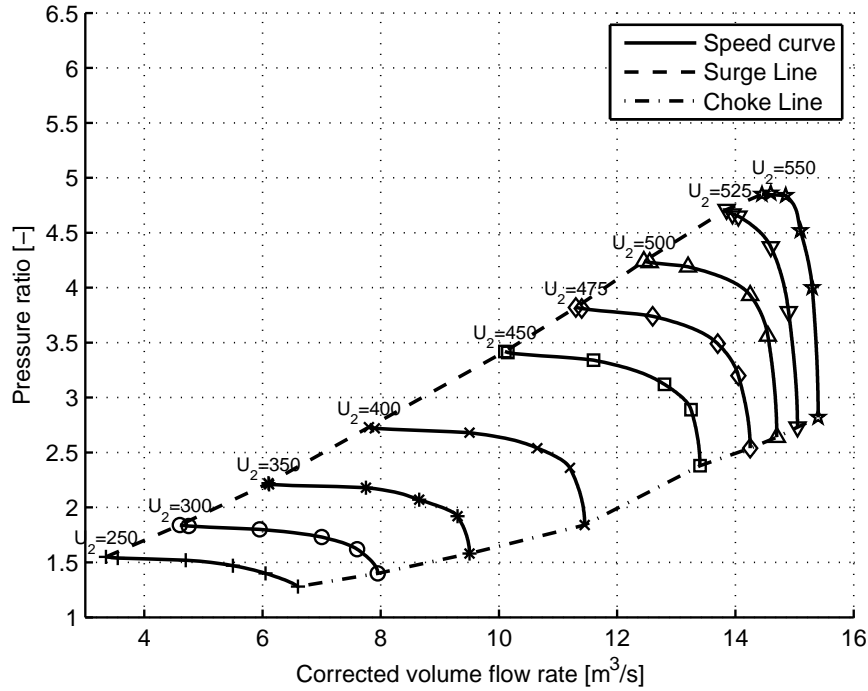


Figure 3.3: A compressor map with constant speed curves, surge line and choke line. Samples are taken from a real compressor map and speed curves are regenerated by Hermite interpolation.

two inputs (Π_c, U_c) needed to decide a flow rate, a two-dimensional interpolation has to be carried out.

The result of a cubic two-dimensional interpolation is seen in Figure 3.4. The compressor flow rate can be found by giving any input of pressure ratio and turbocharger speed within the region. Inputs of pressure ratio and turbo speed outside the specified domain, however, are invalid and there is no output. This is because extrapolation (determining values outside of the valid data set) is unreliable or unavailable depending on the interpolation method used.

A two-dimensional interpolation is also entitled a surface fit. This can be illustrated by plotting the compressor flow map in three dimensions, with U_c as the z-axis (Figure 3.5). Interpolation of the samples create a surface in the three-dimensional (Q_c, Π_c, U_c)-space. The more common map representation is shown as a projection in the (Q, Π)-plane.

3.2 Flow Rate Modeling

Although interpolation in the previous section gave pleasing results there are some subtleties related to interpolation. A compressor map developed by interpolation is

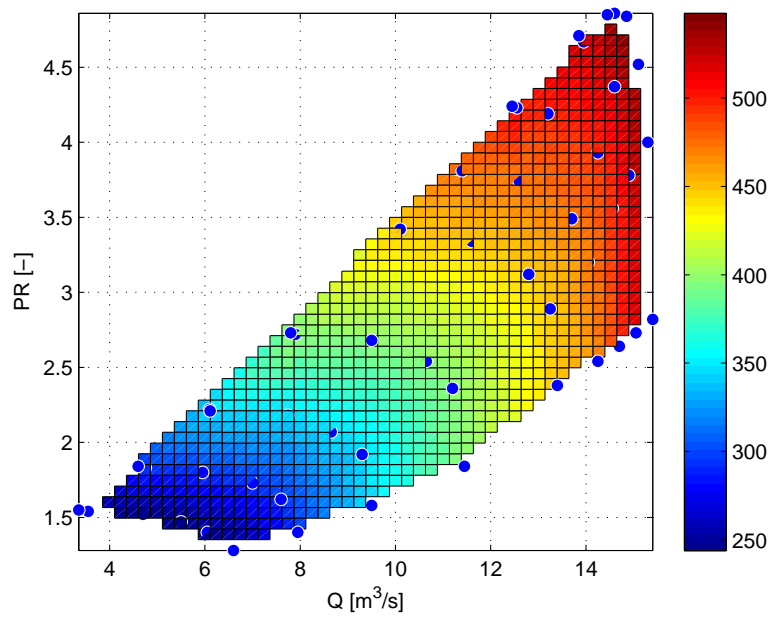


Figure 3.4: Cubic interpolation of speed samples (blue circles) with color-coded turbocharger speed.

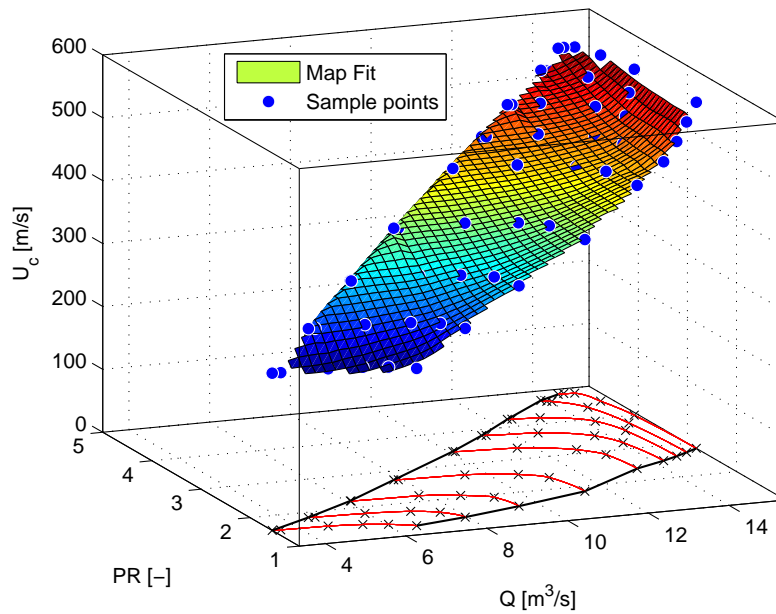


Figure 3.5: Surface fit of the compressor map samples (blue circles) with constant speed curves (solid red) projected into the (Q, PR) -plane. The projected samples are also shown (black cross).

not always well suited for dynamic system simulations. For instance, the standard interpolation methods are not continuously differentiable, the non-linear characteristics of the turbocharger makes linear interpolation unreliable, and lastly, experimental data are usually unavailable for low speed/pressure ratios therefore extrapolation capabilities are occasionally desired. Interpolation with lookup tables may for these reasons give unacceptable simulation performance. Additionally, the interpolation methods guarantee that the every sample is met exactly, which is disadvantageous if there are noisy samples. A parameter fit on a model will, on the other hand, depreciate noisy samples. See [16, 17] for further discussion on interpolation of compressor maps.

Experimental data at low pressure and flow values suffer from reduced accuracy of the flow [16]. Another cause of inaccurate measures at low compressor speed is the heat transfer from hot lubrication oil to the cool compressor. This effect can be seen in the compressor map as the efficiency collapses at small pressure ratios. At high speed the heat transfer may take place in the opposite direction, from the compressor to the lubricants.

The unknown volume flow rate through the compressor should be modeled as a function of the known pressure ratio and turbocharger speed

$$Q_c = f(\Pi_c, N_{tc}) \quad (3.2)$$

As previously discussed, corrected quantities are often used instead of normal flow rate and speed. These corrected values are derived from the dimensionless pressure head Ψ , the normalized compressor flow rate Φ and the inlet Mach number M given as [18, p.68]

$$\Psi = \frac{c_p T_{amb} \left(\Pi_c^{\frac{\kappa_a - 1}{\kappa_a}} - 1 \right)}{0.5 U_c^2} \quad (3.3)$$

$$\Phi = \frac{\dot{m}_c}{\rho_a \frac{\pi}{4} d_c^2 U_c} = \frac{Q_c}{\frac{\pi}{4} d_c^2 U_c} \quad (3.4)$$

$$M = \frac{U_c}{\sqrt{\kappa_a R_a T_{amb}}} \quad (3.5)$$

where the parameters are described in Table 3.1.

The motive for using *dimensionless* analysis is that changes in the environmental conditions (pressure and temperature) are included in the parameters. *Dimensional* investigation, on the contrary, is a beneficial approach to gain insight on what parameters affect the performance. A problem with dimensional analysis is the requirement of extra measurements to be taken during experimentation compared to a dimensionless approach. Furthermore the dimensionless concept gives a compact description of the performance.

The region of the compressor map that is mainly of interest is the region between the surge and choke lines, provided the engine turbocharger works with a

Table 3.1: Parameters used in conversion to dimensionless values.

Symbol	Description	Value	Unit
ρ_a	Density, air	1.23	kg/m ³
κ_a	Ratio of specific heats, air	1.4	
c_p	Specific heat at constant pressure, air	1005	J/(kg K)
R_a	Specific gas constant, air	287	J/(kg K)
T_{amb}	Ambient temperature	293.2	K
d_c	Compressor diameter	0.5	m

sufficient surge margin. The choke line represents the points of the map where maximum *flow* is achieved for every constant speed. Reducing the pressure ratio any further will not increase the flow, the choke line is therefore described by the rightmost sample of each speed curve in Figure 3.3. The choked flow varies by turbocharger speed.

In contrast to the choke line, the surge line represents the maximum *pressure* that is achieved for every constant speed. Reducing the flow rate at the surge line will not increase the pressure ratio. The surge line is described by the leftmost samples for each turbo speed.

The dimensionless choke and surge samples are given in Figures 3.7 and 3.8 as functions of turbocharger Mach speed number M . It is seen that a 2nd order polynomial fails to represent the choke line flow (Fig. 3.7a), but that a 3rd order polynomial makes a good fit for both the surge and choke line flow (Fig. 3.7b and Fig. 3.8b). It is therefore assumed that every flow line bounded by the surge and choke line can be adequately represented by a third order polynomial of M

$$\Phi = a_3M^3 + a_2M^2 + a_1M + a_0 \quad (3.6)$$

Equivalently a 4th order polynomial of M gives sufficiently good fit for the dimensionless choke and surge pressure (Fig. 3.7e and Fig. 3.8e). For this reason it is assumed that every pressure in the compressor map can be represented by a 4th order polynomial of M

$$\Psi = c_4M^4 + c_3M^3 + c_2M^2 + c_1M + c_0 \quad (3.7)$$

Increasing the polynomial order would make the fitted curve approach the samples more closely. However, increasing the order can generate an oscillatory curve as seen in Figure 3.6, leading to a less reliable rendition of the true functional relationship. Furthermore, a higher order polynomial will often produce more unreliable extrapolation.

Figure 3.9 demonstrates that the shape of the speed curves in dimensionless quantities resemble those of the original map. By visual inspection it is seen that the dimensionless speed curves can be approximated by a negative exponential

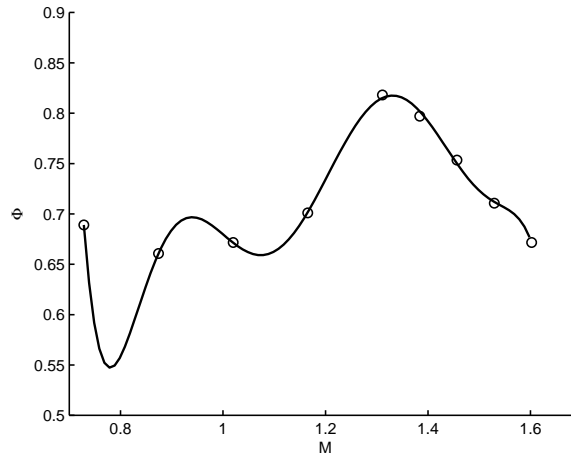


Figure 3.6: The choke line pressure as a 7th order polynomial of Mach number.

function of pressure ratio, i.e. the flow rate decreases by an exponential function of pressure. The choked flow compares to the (approximately) flat start of the exponential function. As the pressure increases the flow quickly decreases (the speed curve flattens out), which is comparable to a negative exponential growth.

3.2.1 Exponential Method

The dimensionless flow through the compressor can be expressed by the following exponential function of dimensionless pressure

$$\Phi(\Psi) = -e^{\Psi} \quad (3.8)$$

For the reason that $\Phi(0) = -1$ the function is shifted such that a zero input gives a zero output

$$\Phi(\Psi) = 1 - e^{\Psi} \quad (3.9)$$

$$\Phi(0) = 0 \quad (3.10)$$

Considering that the choked flow varies with turbocharger speed, the value of $\Phi(0)$ should be adjusted differently for each speed curve. Consequently, the flow function is expanded with a parameter a to describe the flow value in choked conditions

$$\Phi(\Psi) = a + (1 - e^{\Psi}) \quad (3.11)$$

Giving

$$\Phi(0) = a \quad (3.12)$$

Figure 3.10a shows the function (3.11) for $a = 8$ and $a = 10$. Seeing as the choked flow increases with speed, and that the choke line can be described by a third order

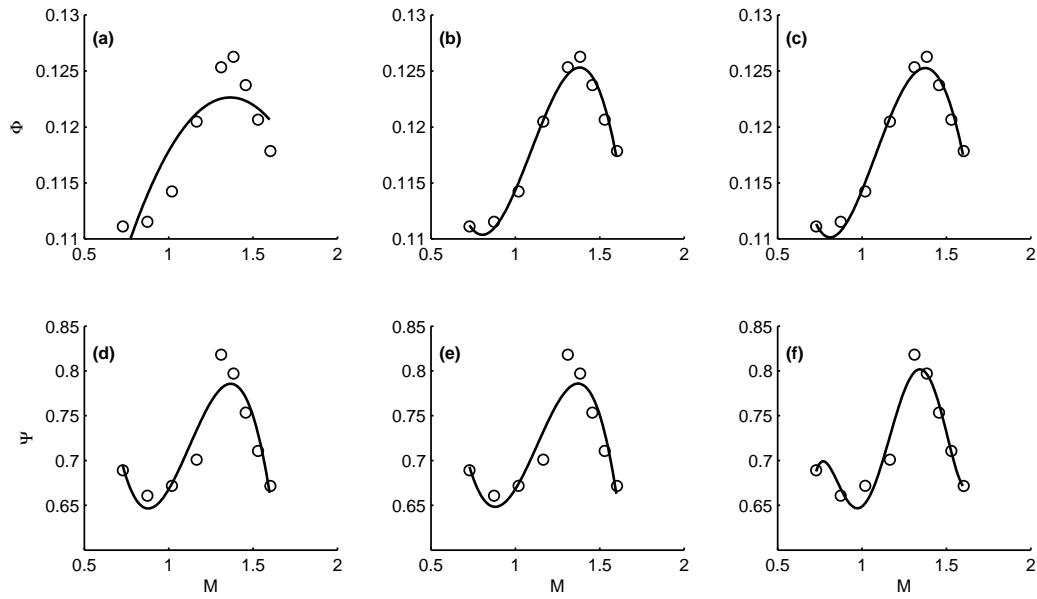


Figure 3.7: Choke line samples represented with dimensionless parameters, the *choke flow* is fitted to a (a) 2nd, (b) 3rd, (c) 4th order polynomial of M . The *choke pressure* is fitted to a (d) 3rd, (e) 4th, (f) 5th order polynomial of M .

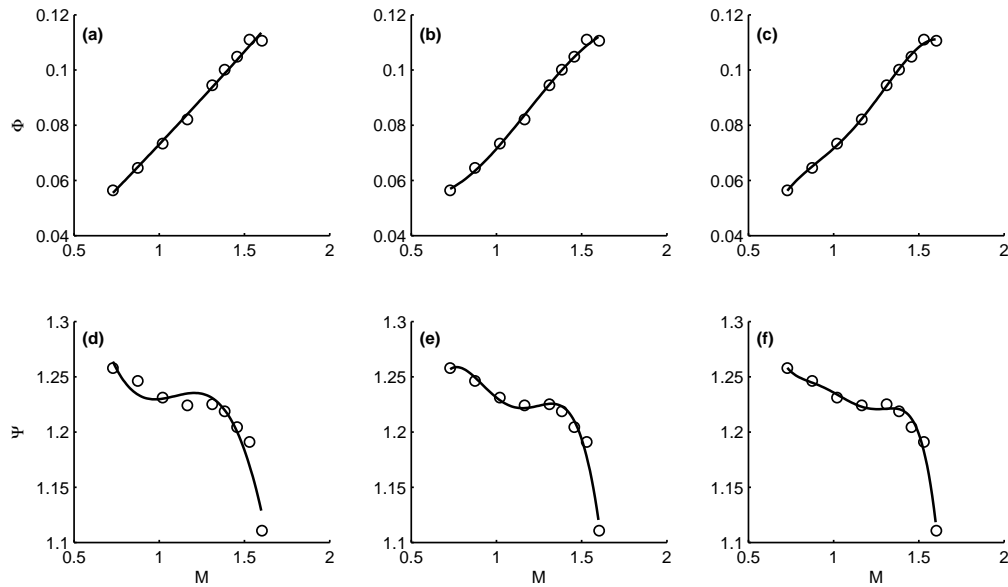


Figure 3.8: Surge line samples represented with dimensionless parameters, the *surge flow* is fitted to a (a) 2nd, (b) 3rd, (c) 4th order polynomial of M . The *surge pressure* is fitted to a (d) 3rd, (e) 4th, (f) 5th order polynomial of M .

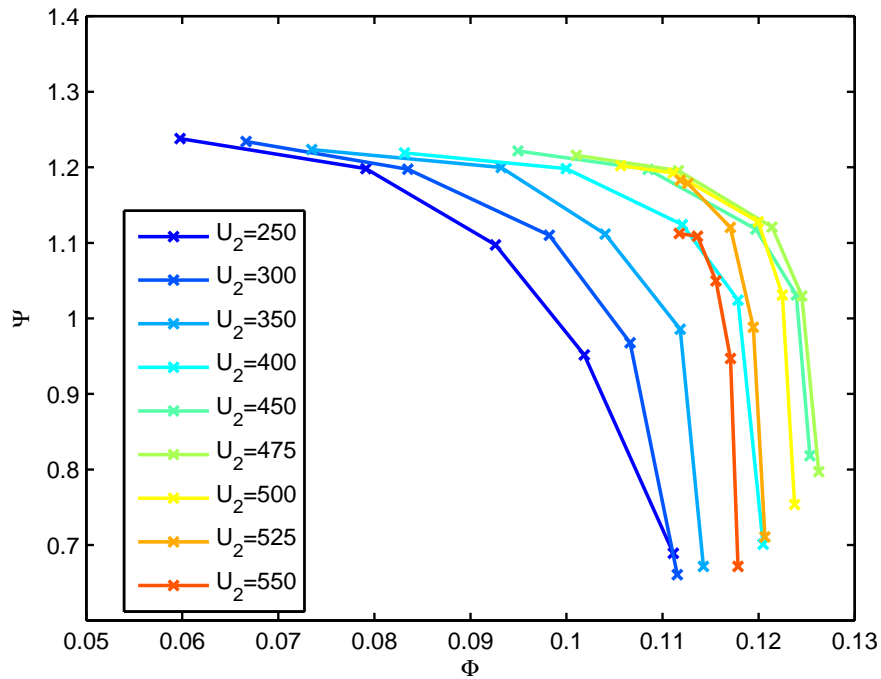


Figure 3.9: Compressor speed curves given in dimensionless (Φ, Ψ) -coordinates.

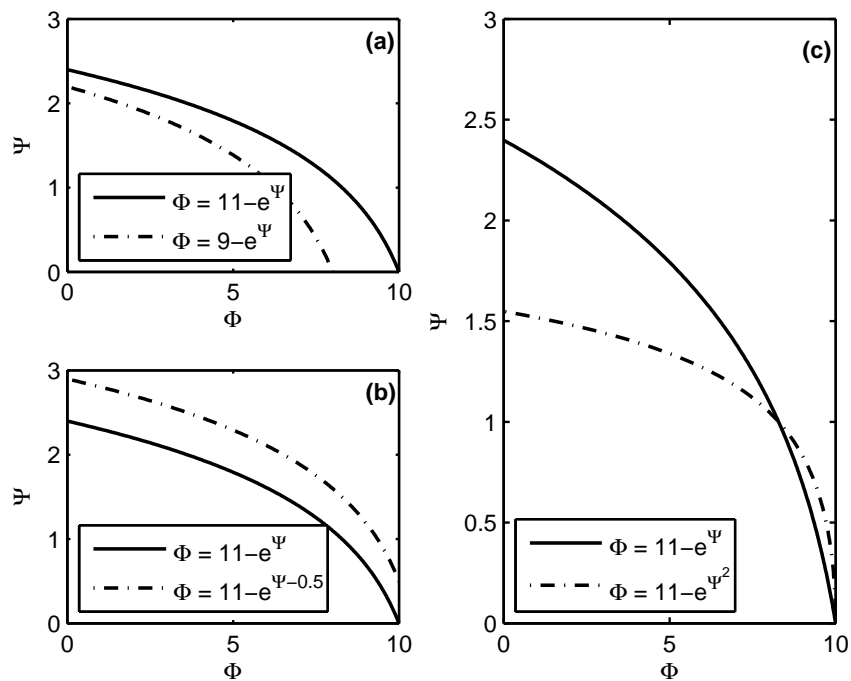


Figure 3.10: Properties of the exponential function.

polynomial of Mach speed, as previously discussed, the parameter a is set to

$$a = a_3M^3 + a_2M^2 + a_1M + a_0 \quad (3.13)$$

Choking of the flow does, however, not start at $\Psi = 0$. Choking begins at a pressure ratio $\Pi_c > 1$. A shift in the pressure ratio should therefore be exercised to originate the choked flow at the correct pressure value. This is achieved by shifting Ψ by b

$$\Phi = a + (1 - e^{\Psi-b}) \quad (3.14)$$

or equivalently

$$\Phi = a + \left(1 - \frac{e^{\Psi}}{e^b}\right) = a + (1 - ke^{\Psi}) \quad (3.15)$$

where $k = e^{-b}$. Setting $b \neq 0$ will shift the exponential function up or down. A positive b shifts the curve up, whilst a negative value of b shifts the curve down (Figure 3.10b). The value of b corresponds to the pressure when $\Phi = a$, i.e. b is the choke line pressure. As a consequence the choke line can be described by alternating a and b .

In addition to determine the choke pressure, the b -coefficient can affect the surge pressure due to the height of the curve being adjusted. The pressure lines in the map was argued to be represented by a fourth order polynomial of M , however, a third order polynomial also gives a good fit and can be used for reducing the number of model coefficients. By examination of the graphs in Figures 3.8d-f and Figure 3.9 it is seen that the surge pressure for the highest speed is somewhat of an outlier. Neglecting the outlier, a second-order polynomial can be argued to be applied, giving

$$b = b_2M^2 + b_1M + b_0 \quad (3.16)$$

Adjusting the choke pressure and curve height by only one parameter, b , is not sufficient. Also, the speed curves at high speeds tend to show a more abrupt transition between choke and surge, this could be included in the model by raising Ψ to the power of a speed dependent coefficient c

$$\Phi = a - e^{\Psi^c+b} \quad (3.17)$$

where

$$c = c_2M^2 + c_1M + c_0 \quad (3.18)$$

The effect of changing c can be seen in Figure 3.10c. A larger value of c makes the choked part of the curve more vertical and the transition towards surge faster. The final compressor flow model becomes

$$\Phi = a + (1 - e^{\Psi^c+b}) \quad (3.19)$$

Another method is to use a to adjust the shift in Ψ in addition to Φ

$$\Phi = a \left(1 - e^{\Psi^c+b}\right) \quad (3.20)$$

A negative aspect by this approach is that it makes the value of a not directly correspond to the choked flow.

3.2.2 Exponential Threshold Method

An alternative approach to modeling the flow rate by exponential functions is to assume that the transition between choking and flattening of the flow can be seen as crossing a threshold. The exponential function grows moderately until reaching the pressure threshold, where choking behavior seizes. When traversing the threshold the flow starts decreasing more quickly. The relationship is described by

$$\Phi = 1 - e^{\left(\frac{\Psi}{\Psi_{th}} - 1\right)} \quad (3.21)$$

The effects of the threshold are

$$\Psi < \Psi_{th} \Rightarrow \frac{\Psi}{\Psi_{th}} - 1 < 0 \Rightarrow 0 < \Phi < 1 \quad (3.22)$$

$$\Psi = \Psi_{th} \Rightarrow \frac{\Psi}{\Psi_{th}} - 1 = 0 \Rightarrow \Phi = 0 \quad (3.23)$$

$$\Psi > \Psi_{th} \Rightarrow \frac{\Psi}{\Psi_{th}} - 1 > 0 \Rightarrow \Phi < 0 \quad (3.24)$$

Until the pressure reaches the threshold the exponent is negative, the result is an almost constant flow, i.e. decreasing very slowly with increased pressure. At the threshold both the exponent and the flow is zero. As the pressure rises above the threshold the exponents becomes positive and the flow starts to decrease fast. The threshold pressure is assigned the same polynomial degree as the choke pressure fit in Figure 3.7-e

$$\Psi_{th} = c_4 M^4 + c_3 M^3 + c_2 M^2 + c_1 M + c_0 \quad (3.25)$$

The same speed-dependent coefficient, as used earlier, is adopted to introduce that the choked flow rate varies with speed

$$\alpha = a_3 M^3 + a_2 M^2 + a_1 M + a_0 \quad (3.26)$$

Such that

$$\Phi = \alpha \left(1 - e^{\left(\frac{\Psi}{\Psi_{th}} - 1\right)}\right) \quad (3.27)$$

The pressure input Ψ has a smaller effect than in the previous model as a result of being scaled by the threshold value Ψ_{th} . Therefore a gain (β) is included in the exponent to achieve a faster response, and additionally make the curves more speed dependent. The β -factor is a second order polynomial of the Mach number.

$$\beta = b_2 M^2 + b_1 M + b_0 \quad (3.28)$$

The final model becomes

$$\Phi = \alpha \left(1 - e^{\beta \left(\frac{\Psi}{\Psi_{th}} - 1\right)}\right) \quad (3.29)$$

3.2.3 Results and Discussion

All the coefficients a_i , b_i and c_i of the two models are regression coefficients obtained by least squares curve fitting of the compressor data. The resulting coefficient for the models (3.20) and (3.29) are given in Tables B.1 and B.2 in Appendix B. The corresponding air volume flow rate can be found by using (3.4), giving

$$Q_c = \Phi \frac{\pi}{4} d_c^2 U_c \quad (3.30)$$

Or alternatively, the mass flow rate

$$\dot{m}_c = \Phi \frac{\pi}{4} d_c^2 U_c \rho_a \quad (3.31)$$

Figure 3.12 displays that both models produce curves that fit the samples appropriately. The threshold method tend to choke a little early for slow speeds, where the other method performs satisfying. On the other hand, the threshold method looks to produce better results at higher speeds. The difference between the methods are, however, slight and almost insignificant. Both models supply convincing results.

The flow for $U_c = 425$ is plotted for an extended pressure region to demonstrate how the models perform outside the specified map region. It shows that the models are capable of providing credible outputs for unconventional inputs. For instance, in the choke region the flow is virtually constant and independent of the pressure ratio, like anticipated. Moreover, if the input to the models is in the surge area, the typical surge dynamics are simplified by a near horizontal line. This is a result of the exponential function eventually generating a large drop in the flow rate by a small increase in pressure.

For a real compressor, entering the surge region would result in a decreased flow and pressure ratio leading to subsequent oscillations. In the model, the surge region is simplified by a roughly leveled line. The lower the speed, the more horizontal the modeled surge region is. This is a consequence of the shape of the curve in the specified region between the surge and choke. Low speed curves are flatter and high speed curves are more vertical.

A problem that occurs by approximating the surge region with an exponential function is that a slight pressure increase could result in a drastically reduced flow rate. This is due to the almost flat lines that follow from the exponential function. Flow values in simulation may therefore fall below realistic values, they might even become negative.

A solution to prevent unrealistic flow values in the surge region is to limit the flow rate to the surge flow

$$Q_c = \max(Q_c, Q_{\text{srsg}}(U_c)) \quad (3.32)$$

The surge line flow rate $Q_{\text{srsg}}(U_c)$ can be found by a polynomial of turbocharger speed. Figure 3.11 shows the surge line for a second and third order polynomial

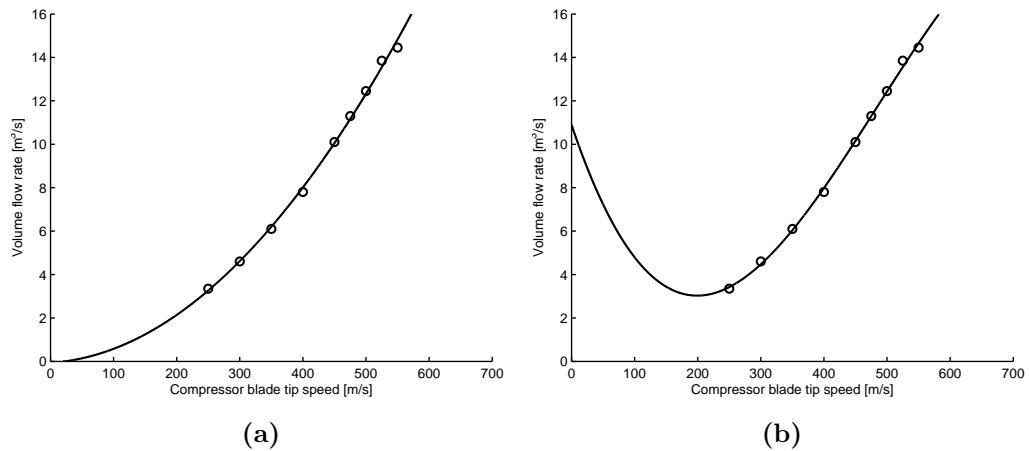


Figure 3.11: Surge volume flow rate fit as a second order (a) and third order (b) polynomial compressor blade tip speed.

fit. For this particular compressor a second order polynomial provides an excellent fit. The two polynomials give more or less the same fit inside the specified region. However, the second order model demonstrates realistic extrapolation potential, the third order fit does not. To conclude; if the compressor should go into the surge region - either because real surging occurs or as a result of simulation errors - the effect is simply ignored and the flow is placed on the surge line. Ignoring the surge region is a fair assumption considering that the ship is presumed to operate with a sufficient surge margin. The limitation provides a safety to cope with potential simulation misbehavior.

Extrapolation capabilities of the two exponential flow models are investigated by mapping a speed curve for $U_c = 200$. This is lower than the minimal speed in the supplied map ($U_c = 250$). The plot (Figure 3.12) shows that the first exponential method yields a credible representation of the flow. The threshold method, on the other hand, produces extrapolation results that are irrational. Despite both methods giving solid results within the specified region, the first exponential method is chosen for its ability to extend the compressor map to lower speed regions. Extrapolation beyond $U_c = 550$ is not an issue considering the mechanical speed limit of the compressor.

The reason for the failure of the threshold methods extrapolation may be that the parameter polynomials are of higher order than the other method. As seen above, a higher order polynomial may produce unrealistic extrapolation.

3.2.4 Alternative Method (Rectangular Hyperbolas)

In this section the developed model is compared with one frequently occurring in literature. The reason for developing a new flow model in the first place was

because the least squares curve fit gave incorrect results, due to some issues discussed in this chapter. The method is presented in Moraal and Kolmanovsky [16]. The authors compare four different models on three different compressors. They conclude that the following method perform best for a model using pressure ratio and speed to compute mass flow

$$\Psi = \frac{k_1 + k_2\Phi}{k_3 - \Phi} \quad (3.33)$$

$$k_i = k_{i1} + k_{i2}M, \quad i = 1, 2, 3 \quad (3.34)$$

where the dimensionless parameters Ψ , Φ and M are given in (3.3)-(3.5). As a result of the equation (3.33) being invertible the corresponding flow Φ can be solved as

$$\Phi = \frac{k_3\Psi - k_1}{k_2 + \Psi} \quad (3.35)$$

The coefficients k are determined through a least squares fit on the experimental data. Results of the curve fit is given in Table B.3 in Appendix B. Figure 3.13 shows that the modeling approach gives results inferior to that of the previous model. The samples are hardly matched by the model. Additionally the model fails to reproduce complete choking of the flow. On an attempt to improve the model the order of the coefficient polynomial k_i is increased from a first order to second order of M .

$$k_i = k_{i1} + k_{i2}M + k_{i3}M^2 \quad (3.36)$$

Figure 3.14 shows that the altered model indeed improves the output. The samples are matched better and it appears to provoke a more choking behavior. Nevertheless, the results from the exponential models (3.20) and (3.29) are favoured. Comparison of the exponential threshold method and the improved alternative model is shown in Figure 3.15.

The behavior and disadvantages of the function (3.35) are not properly explained in Moraal and Kolmanovsky [16], nor any of the other sources that discuss the model [19, 20, 21]. Plotting the function reveals a scaled and shifted *rectangular hyperbola* (Figure 3.16). The bottom left section of the plot resembles a speed curve and is suitable for flow modeling. The model has a singularity at $\Psi = -k_2$. During simulation it is crucial that this singularity is not crossed. Crossing the singularity would move the flow rate to the top right part of the plot, consequently exceeding the choke limit.

Another inconvenience of the model is that if the the initial coefficient values are not chosen appropriately the fit will approximate the curve in the right half to the samples. The curve fit then searches for a local minima instead of the global minima. The resulting model fails, illustrated in Figure 3.17.

Equation (3.33) shows that the model has another singularity at $\Phi = k_3$. For

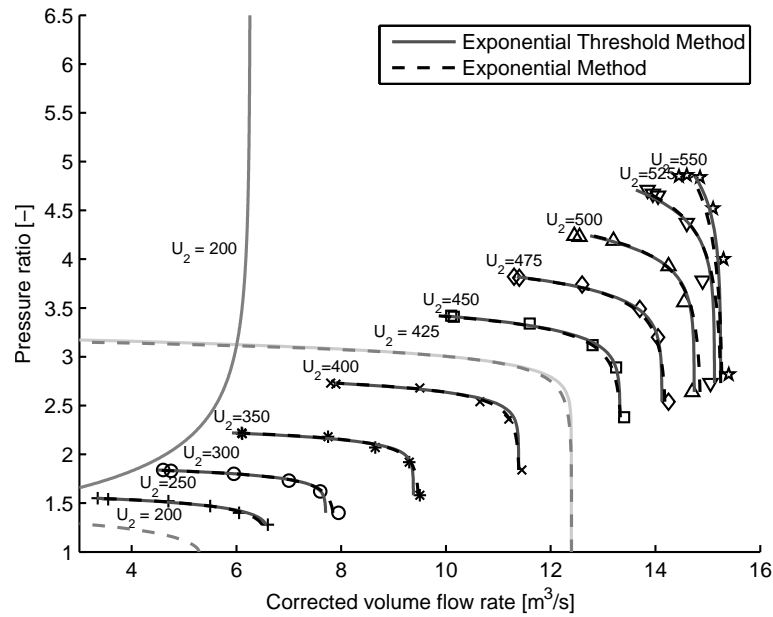


Figure 3.12: Comparison of the exponential method and the threshold method. In addition to the sampled speed curves, an extended speed curve for $U_c = 425$ and an extrapolated curve for $U_c = 200$ are shown.

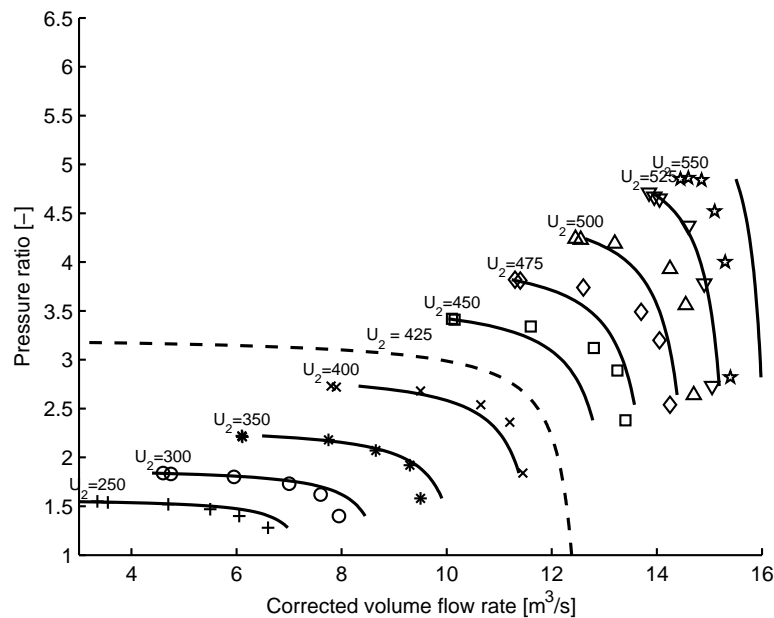


Figure 3.13: Modeled compressor volume flow rate at constant turbocharger speed with the alternative method. Solid curves represent the speed of the samples, the dashed curve indicates an extended speed curve for $U_c = 425$

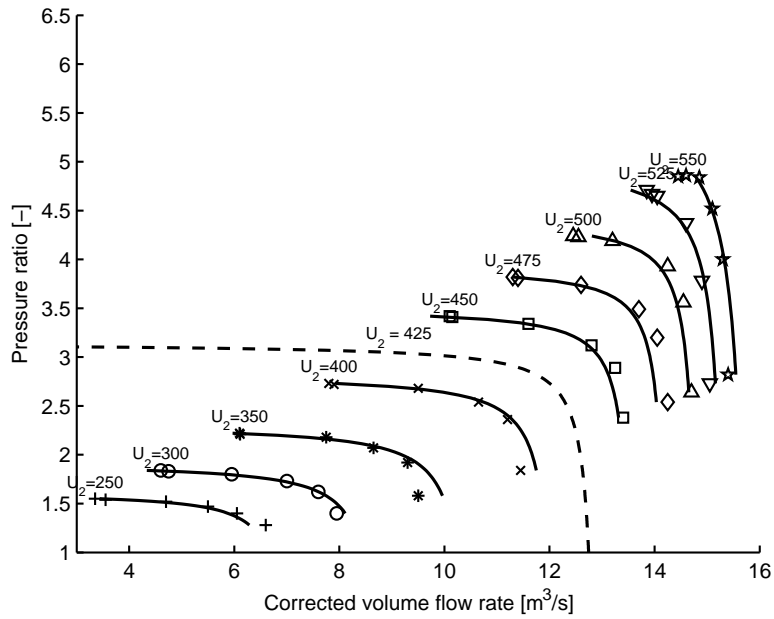


Figure 3.14: Modeled compressor volume flow rate at constant turbocharger speed with the *improved* alternative method. Solid curves represent the speed of the samples, the dashed curve indicates an extended speed curve for $U_c = 425$.

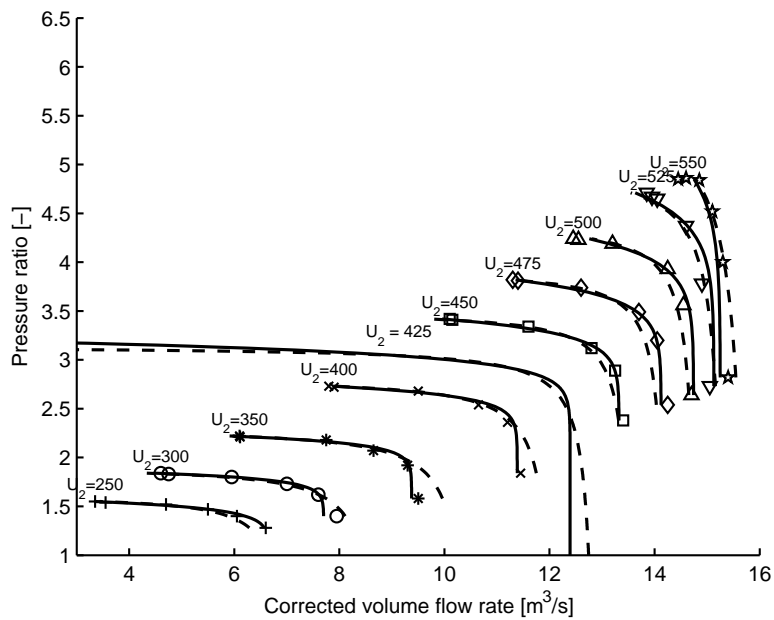


Figure 3.15: Comparing the exponential threshold flow model (solid) and the hyperbola model (dashed).

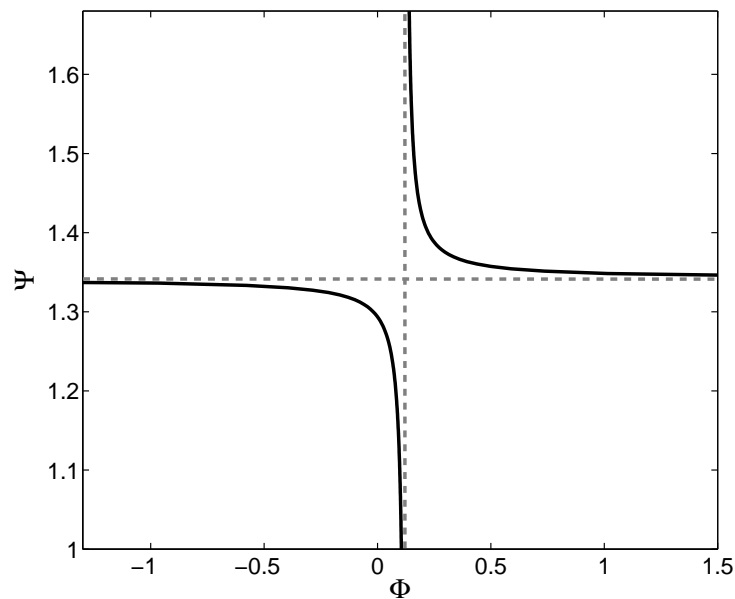


Figure 3.16: Normalized flow function $\Phi = \frac{k_3\Psi - k_1}{k_2 + \Psi}$ for $M = 0.874$. The lower left part of the graph resembles a speed curve. Asymptotes are showed as dashed lines.

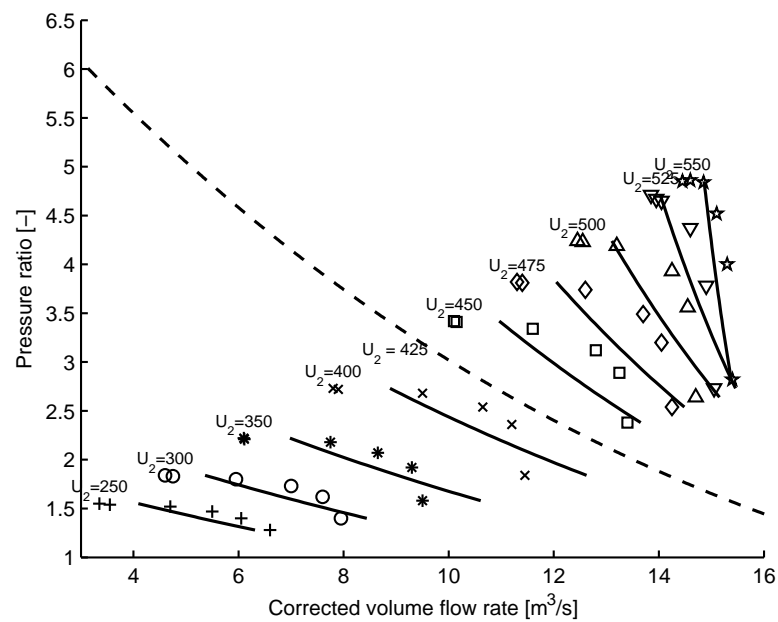


Figure 3.17: The alternative flow model with poor choice of initial coefficient values. Solid curves represent the speed of the samples, the dashed curve indicates an extended speed curve for $U_c = 425$.

this reason the initial coefficients for the curve fit has to be chosen such that

$$k_2 < 0, \quad (3.37)$$

$$k_3 > 0 \quad (3.38)$$

for all M .

Other possible modeling approaches exists. In [16, 22, 23] the compressor flow rate is modeled by neural networks. Ellipses is used in [19, 18]. Malkhede [24] uses a third order polynomial of speed and pressure ratio. If modeling of surge behavior is of interest, the reader can consult [25, 19, 20, 26].

3.3 Efficiency

There are multiple approaches to modeling efficiency curves of a compressor map. All of the following functional relationships may be used as a basis for a model

$$\eta_c = f_1(Q_c, \Pi_c)$$

$$\eta_c = f_2(Q_c, U_c)$$

$$\eta_c = f_3(\Pi_c, U_c)$$

Alternatively, corrected or dimensionless numbers may be used. In [16, 21] compressor efficiency is modeled as a second order polynomial of dimensionless flow (Φ) with coefficients depending on the speed (U_c)

$$\eta_c = a_2(U_c)\Phi^2 + a_1(U_c)\Phi + a_0(U_c) \quad (3.39)$$

A disadvantage of this model is the possibility of taking samples only at points where a speed curve cuts across an efficiency contour. Moreover, the real efficiency is directly linked to the pressure ratio.

3.3.1 Polynomial Fit

Efficiency curves in the supplied map is given in the (Q_c, Π_c) -coordinate system. By using flow and pressure as inputs to the model one is free to collect an arbitrarily amount of samples in the provided map. Thus sampling is not limited to intersections between curves of constant speed and efficiency. As a consequence more samples can be taken and a better fit can be achieved. The basis for the model becomes

$$\eta_c = f(Q_c, \Pi_c) \quad (3.40)$$

By visual inspection it is difficult to suggest a functional relationship between the variables, particularly since there are two independent variables. A polynomial

approach is attempted. By trial and error it was found that a 5th order polynomial of $Q_c = x$ and $\Pi_c = y$ was sufficient to portray the real efficiency curves

$$\begin{aligned} \eta_c = f(x, y) = & p_{00} + p_{10}x + p_{01}y + p_{20}x^2 + p_{11}xy + p_{02}y^2 \\ & + p_{30}x^3 + p_{21}x^2y + p_{12}xy^2 + p_{03}y^3 \\ & + p_{40}x^4 + p_{31}x^3y + p_{22}x^2y^2 + p_{13}xy^3 + p_{04}y^4 \\ & + p_{50}x^5 + p_{41}x^4y + p_{32}x^3y^2 + p_{23}x^2y^3 + p_{14}xy^4 + p_{05}y^5 \end{aligned} \quad (3.41)$$

3.3.2 Six Parameter Efficiency Model

After implementing the polynomial method, reading more literature revealed that a common method to parametrize the efficiency is by a quadratic decreasing function

$$\eta_c = \eta_c^* - \chi^T Q \chi \quad (3.42)$$

where $Q \in \mathfrak{R}^{2 \times 2}$ and η_c^* is the optimum efficiency. Q must be a symmetric and positive definite matrix in order to give the quadratic form a maximum. In [20, 26] χ is a vector of pressure ratio and corrected mass flow

$$\chi^T = \left[\Pi_c - \Pi_c^*, \dot{m}_{c,\text{corr}} - \dot{m}_{c,\text{corr}}^* \right] \quad (3.43)$$

The parameters that has to be fitted are the maximum efficiency (η_c^*), maximum pressure ratio (Π_c^*), maximum flow rate ($\dot{m}_{c,\text{corr}}^*$) and the three parameters of the Q -matrix

$$Q = \begin{bmatrix} q_{11} & q_{12} \\ q_{21} & q_{22} \end{bmatrix}, \quad q_{12} = q_{21} \quad (3.44)$$

The results of the fitting can be improved by rescaling the ordinate [20]

$$\Pi_c \Rightarrow 1 + \sqrt{\Pi_c - 1} \quad (3.45)$$

The model is often referred to as the *six parameter efficiency model* for the reason that it contains six unknown parameters. In [19], the six parameter model is implemented using a quadratic function of dimensionless flow and corrected speed

$$\chi^T = \left[\Phi - \Phi^*, N_{c,\text{corr}} - N_{c,\text{corr}}^* \right] \quad (3.46)$$

3.3.3 Results and Discussion

A least squares method is applied to obtain the polynomial coefficients $p_{i,j}$ of the model (3.41). The coefficients are found in Table B.4 in Appendix B. Samples and the resulting efficiency surface are seen in Figures 3.18 and 3.19. In addition to producing an excellent fit, the polynomial approach appears to give good extrapolation. For all realistic input values the efficiency polynomial does not resurface

above the lowest provided efficiency in the map. This was warned could happen when using a high degree polynomials (Figure 3.11). However, the polynomial extends nicely in the lower region towards a pressure ratio of 1, and in the higher region towards a pressure ratio of 5.5.

Modeled efficiency contours in the (Q_c, Π_c) -plane are plotted in Figure 3.20, together with samples from the real map. It is seen that the polynomial provides a good fit to the samples. The fully regenerated compressor map with speed and efficiency curves is shown in Figure 3.21. By comparison with the original compressor map (Figure A.1 in Appendix A) it is seen that they are indeed very much alike, and that the compressor map has successfully been reproduced in the simulation software.

As the polynomial approach worked satisfactorily, the six parameter efficiency model was never tested. It was, however, included in the report for sake of reference and possible comparison in the future. Even though the model was not implemented, some general discussion can be done.

The polynomial model (3.41) contains far more parameters than the six-parameter approach (3.42). Consequently the polynomial approach requires more samples. Additionally it will require some more computing time. Performance-wise the polynomial fit is very accurate in the specified domain, and it would be difficult to exceed the performance of the polynomial model. Extrapolation-capabilities are more difficult to compare without implementation of the six-parameter model.

3.4 Concluding Remarks

- Compressor flow rate was found from both interpolation and parameter fitting of models. Modeling surpassed interpolation by the cause of better extrapolation capabilities and being more suited for simulation.
- Two analogous compressor flow models was developed with using an exponential function as the basis for curves of constant speed. Performance of the two models was almost equal, with the exception of one model giving better extrapolation results.
- The developed flow model was compared with a model popular in literature. The new model showed improved performance for the provided compressor map. However, the models has to be compared over a wider range of compressors to give a definite conclusion.
- Compressor efficiency was modeled by a 5th order polynomial. The resulting fit was excellent, and extrapolation in the nearby region of probable inputs was good.

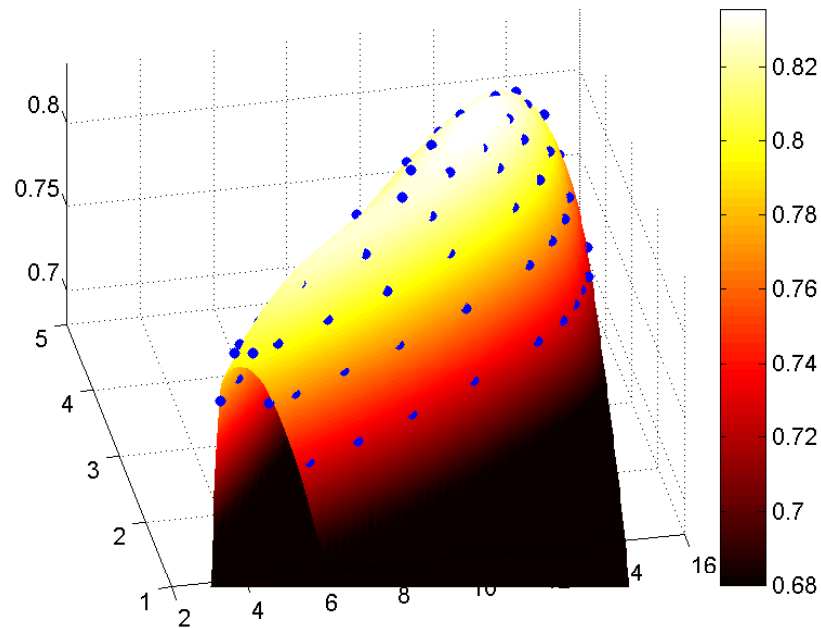


Figure 3.18: Compressor efficiency samples (blue dots) with a 5th order polynomial surface fit. The compressor pressure ratio and volume flow rate are inputs.

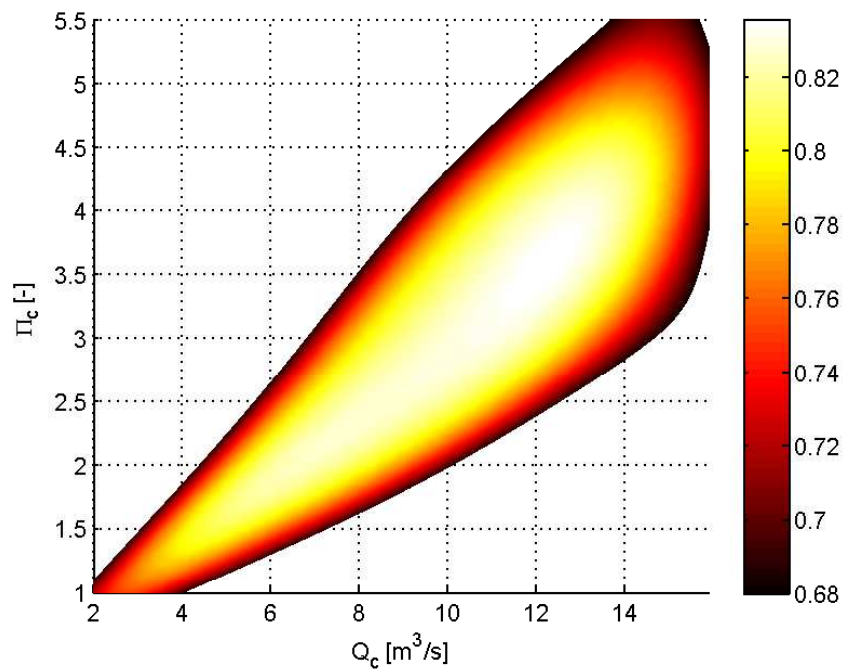


Figure 3.19: Polynomial fit of the compressor efficiency in the (Q_c, Π_c) -plane. Efficiency is color-coded.

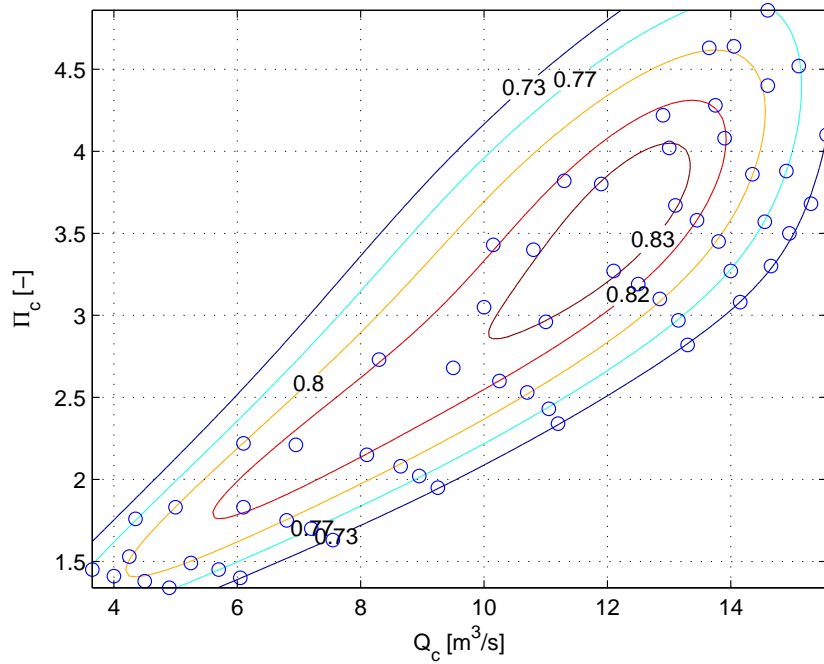


Figure 3.20: Contours of constant efficiency from the 5th order polynomial fit of Q_c and Π_c .

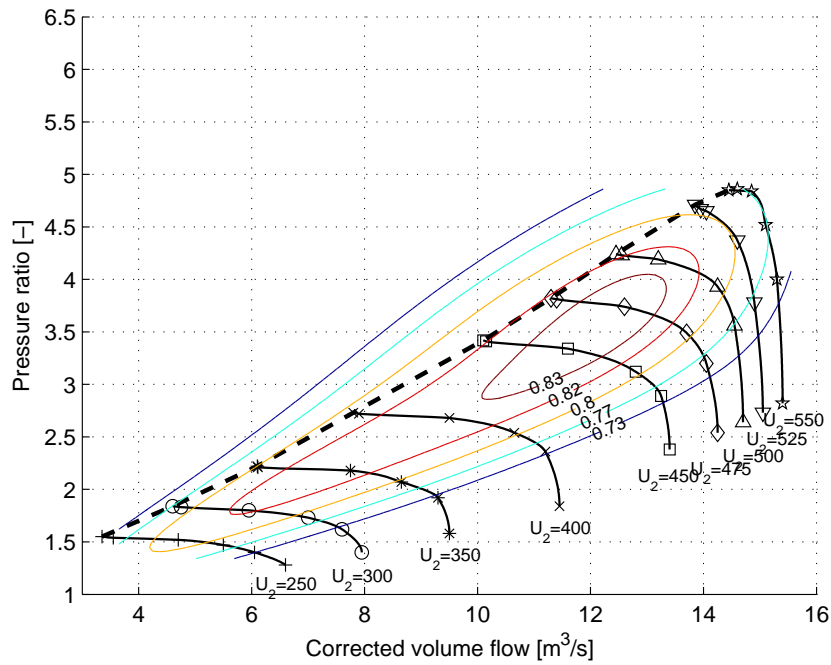


Figure 3.21: Regenerated compressor map with speed lines (solid black), surge line (dashed black) and efficiency contours (colored).

Chapter 4

Turbine Modeling

Accurate modeling of the turbine performance is important to find the correct driving torque to the turbocharger shaft, so that correct compressor speed and consequential air-fuel ratio is modeled. The exact modeling of the turbine flow and efficiency is motivated by the possibility of using variable area turbine control for manipulation of the turbocharger speed and thus the airflow to the engine cylinders. Additionally, a rigorous description of the turbine is beneficial for the implementation of a turbine wastegate to relieve the turbocharger of excessive torque stress and also reduce speed.

A turbine flow rate map for a MAN Diesel & Turbo TCA55 turbocharger is provided in Figure A.2 in Appendix A. The two unknown turbine variables that need to be established are the turbine flow and efficiency. Seeing that the turbine pressure ratio $p_{ep}/p_{em} < 1$, the *expansion* ratio is adopted instead

$$\Pi_t = \frac{p_{em}}{p_{ep}} \quad (4.1)$$

Flow in the map is described by an adjusted volume flow rate

$$\hat{Q}_t = \frac{Q_t}{\sqrt{T_{em}}} \text{ [m}^3\text{/(s } \sqrt{\text{K}}\text{)]} \quad (4.2)$$

Conversion from the unit used in the map to the reduced turbine flow rate

$$Q_{t,\text{red}} = Q_t \frac{\sqrt{T_{em}}}{p_{em}} \quad (4.3)$$

will be shown in this section.

For turbine calculations the dimensionless expressions are of higher importance than for the compressor considering the more extreme variations in the inlet conditions. Exhaust gas temperatures may vary from 500K up to 1300K [27].

The chapter starts by fitting the turbine map data to a turbine flow rate model, second a fix is introduced to guarantee that Lipschitz conditions are fulfilled for flow through a restriction, lastly modeling the turbine efficiency is performed.

4.1 Turbine Flow

In the project work [4], turbine flow rate was determined by flow through a restriction. The flow equation was

$$\dot{m}_t = c_t A_{T_{eq}} \frac{p_{em}}{\sqrt{R_e T_{em}}} \Psi(1/\Pi_t) \quad (4.4)$$

where p_{em} is the exhaust manifold pressure, T_{em} the exhaust manifold temperature, R_e the specific gas constant for exhaust gas, $A_{T_{eq}}$ the equivalent effective turbine area calculated from geometrical data, c_t the turbine correction factor and Ψ (not to be confused with dimensionless flow) is found from

$$\Psi(1/\Pi_t) = \begin{cases} (1/\Pi_t)^{\frac{1}{\kappa_e}} \sqrt{\frac{2\kappa_e}{\kappa_e-1} \left[1 - (1/\Pi_t)^{\frac{\kappa_e-1}{\kappa_e}} \right]} & \text{for } \Pi_t \leq \left(\frac{\kappa_e+1}{2} \right)^{\frac{\kappa_e}{\kappa_e-1}} \\ \sqrt{\kappa_e \left(\frac{2}{\kappa_e+1} \right)^{\frac{\kappa_e+1}{\kappa_e-1}}} & \text{for } \Pi_t > \left(\frac{\kappa_e+1}{2} \right)^{\frac{\kappa_e}{\kappa_e-1}} \end{cases} \quad (4.5)$$

Choking of the flow occurs at

$$\Pi_t > \left(\frac{\kappa_e + 1}{2} \right)^{\frac{\kappa_e}{\kappa_e-1}} \quad (4.6)$$

Rearranging the terms in (4.4) the expression becomes

$$\frac{\dot{m}_t \sqrt{T_{em}}}{p_{em}} = \frac{c_t A_{T_{eq}}}{\sqrt{R_e}} \Psi(1/\Pi_t) \quad (4.7)$$

The left side is recognized as the reduced turbine flow parameter $\dot{m}_{t,\text{red}}$ from (2.33). The relation between *mass* flow and *volume* flow is

$$Q_t = \frac{\dot{m}_t}{\rho_e} \quad (4.8)$$

and density of an ideal gas is

$$\rho_e = \frac{P_{em}}{R_e T_{em}} \quad (4.9)$$

Converting from the reduced volume flow (4.7) to the compressor map specified flow (4.2) is done by multiplying the left hand side with $\rho_e/\rho_e = 1$

$$\frac{\dot{m}_t \sqrt{T_{em}} \rho_e}{p_{em} \rho_e} = \frac{c_t A_{Teq}}{\sqrt{R_e}} \Psi(1/\Pi_t) \quad (4.10)$$

\Downarrow (4.8)

$$\frac{Q_t \sqrt{T_{em}}}{p_{em}} \rho_e = \frac{c_t A_{Teq}}{\sqrt{R_e}} \Psi(1/\Pi_t) \quad (4.11)$$

\Downarrow (4.9)

$$\frac{Q_t \sqrt{T_{em}}}{p_{em}} \frac{p_{em}}{R_e T_{em}} = \frac{c_t A_{Teq}}{\sqrt{R_e}} \Psi(1/\Pi_t) \quad (4.12)$$

\Downarrow

$$\frac{Q_t}{\sqrt{T_{em}}} = c_t A_{Teq} \sqrt{R_e} \Psi(1/\Pi_t) \quad (4.13)$$

The left hand side now represents the flow in the supplied turbine map \hat{Q}_t [$\text{m}^3/(\text{s} \sqrt{\text{K}})$]. The right hand side can be used as a model for the flow rate through the turbine. By setting

$$c_0 = c_t A_{Teq} \sqrt{R_e} \quad (4.14)$$

the model can be written

$$\frac{Q_t}{\sqrt{T_{em}}} = c_0 \Psi(1/\Pi_t) \quad (4.15)$$

The coefficient c_0 can then be fitted to the data provided in the manufacturer turbine flow map. The result is shown in Figure 4.1. It is seen that the modeled flow chokes at the critical pressure ratio of

$$\Pi_{cr} = \left(\frac{k_e + 1}{2} \right)^{k_e/(k_e-1)} \approx 1.86 \quad (4.16)$$

where $k_e = 1.34$ is the specific heat ratio for exhaust gas in typical exhaust temperatures [28]. The samples, on the contrary, does not show similar choking behavior. An augmented method is suggested where the model coefficient depend on the expansion ratio

$$\frac{Q_t}{\sqrt{T_{em}}} = \left(\frac{c_1}{\Pi_t} + c_2 \right) \Psi(1/\Pi_t) \quad (4.17)$$

The new model eliminates premature choking of the flow (Figure 4.1). Another approach is to fit data to the following equation [18]

$$\frac{Q_t}{\sqrt{T_{em}}} = c_3 \sqrt{1 - \Pi_t^4} \quad (4.18)$$

Comparing the three models; the first model (4.15) is unsuitable for use as it chokes too early. It gives a too large flow for low pressure values, and a too small

flow for high pressure values. The two latter models (4.17), (4.18) performs almost equally. Model (4.18) shows a more correct behavior for the highest pressures, thus it looks to give better extrapolation abilities. All models fulfill that

$$\Pi_t = 1 \Rightarrow Q_t = 0 \quad (4.19)$$

From (4.18) the volume flow rate can be written

$$Q_t = c_3 \sqrt{T_{em}(1 - \Pi_t^{c_4})} \quad (4.20)$$

Volume flow rate for different exhaust manifold temperatures are plotted in Figure 4.2. The flow rate increases with a rise in temperature and pressure.

Table 4.1: Regression coefficients from least squares fit of the turbine flow models.

Parameter	Value
c_0	0.5503
c_1	-0.1389
c_2	0.6179
c_3	0.3904
c_4	-3.3792

4.2 Modification of Mass Flow Calculation

The nonlinear function Ψ of flow through a restriction has an infinite gradient at $p_{ep} = p_{em}$, rendering the system non-Lipschitz. Numerical simulation problems can occur as the system will be difficult to integrate for values close to this limit. The problem can be avoided by an approximation of the gradient at pressure ratios below a chosen threshold Π_{th}

$$\Pi_{th} = \left. \frac{p_{ep}}{p_{em}} \right|_{th} < 1 \quad (4.21)$$

An approximation is given in [20] as

$$\Psi(\Pi) = a(\Pi - 1)^3 + b(\Pi - 1) \quad (4.22)$$

with

$$a = \frac{\Psi'_{th}(\Pi_{th} - 1) - \Psi_{th}}{2(\Pi_{th} - 1)^3} \quad (4.23)$$

$$b = \Psi'_{th} - 3a(\Pi_{th} - 1)^2 \quad (4.24)$$

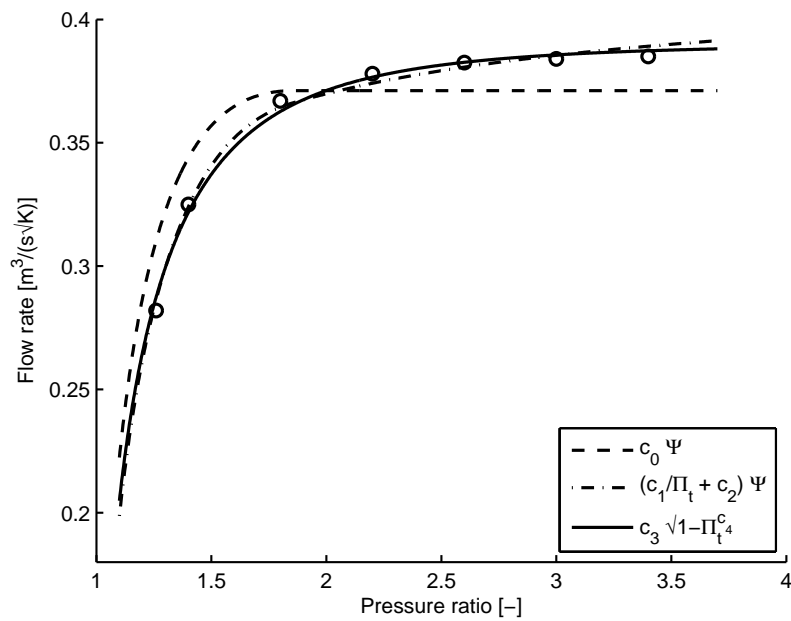


Figure 4.1: Samples (dots) from the provided turbine flow map together with three different model fits.

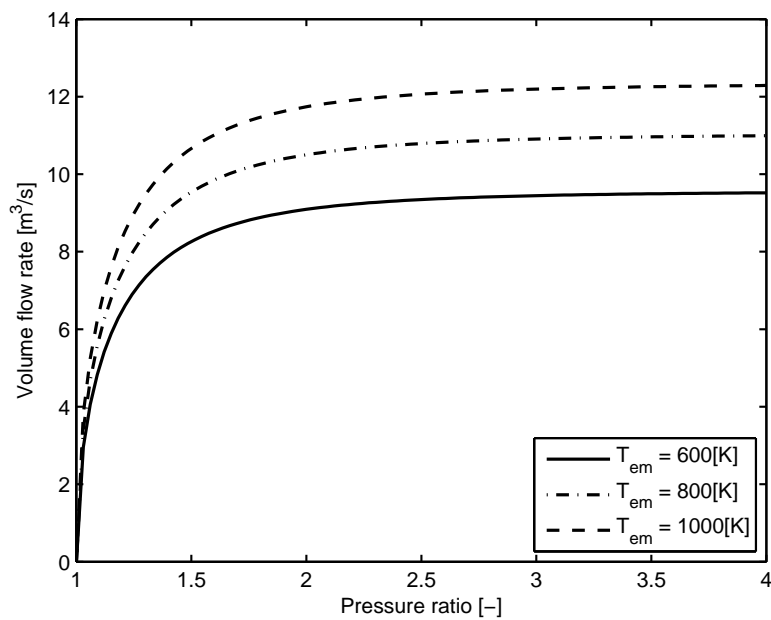


Figure 4.2: Volume flow rate for the turbine given different exhaust manifold temperatures.

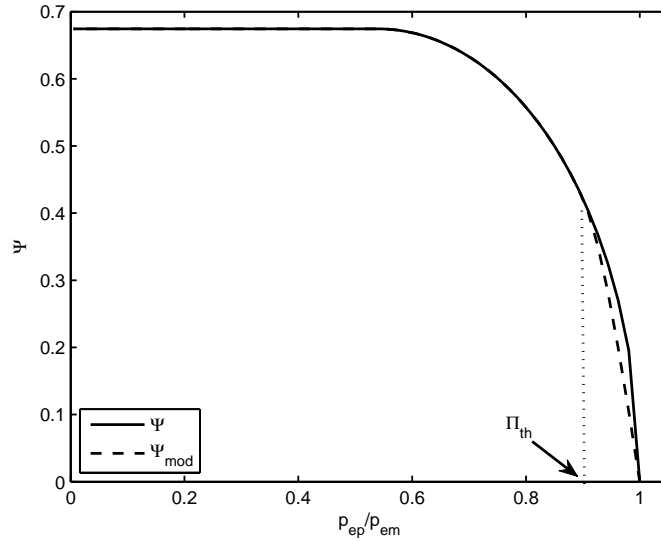


Figure 4.3: Flow through a restriction for a compressible fluid. Ψ shows the usual flow function, Ψ_{mod} is an approximation to the flow around pressure ratio of 1 to make it Lipschitz.

where Π_{th} is the specified threshold pressure, Ψ_{th} the corresponding flow rate and Ψ'_{th} the derivative of Ψ_{th} . Figure 4.3 shows the modified flow function with an unrealistically large threshold $\Pi_{th} = 0.9$, for clarification. The extension can be justified by physics, since the flow is laminar for low flow velocities and turbulent as the velocity increases.

The fix is applied to flow through the turbine if equation (4.17) is used, but more importantly for flow through the engine cylinders where pressure ratios normally are smaller.

4.3 Turbine Efficiency

Usually the turbine efficiency is found from a manufacturer delivered map, however, as the author did not get the hold of a turbine efficiency map a more general approach is performed. Turbine efficiency at the layout point for the particular turbine was, on the other hand, obtained

$$\eta_{t,\max} = 0.81 \quad (4.25)$$

The turbine efficiency is mainly dependent on the blade speed ratio U_t/C_s . Where U_t is the velocity of the turbine blade tip and C_s is the exhaust gas velocity

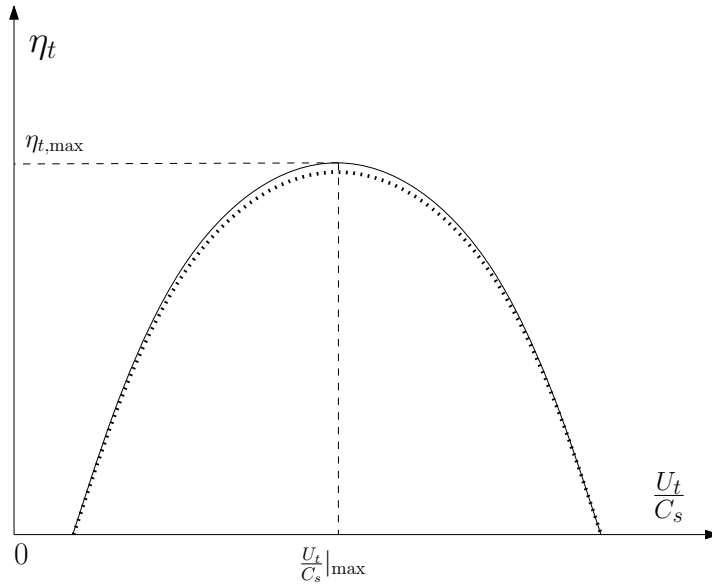


Figure 4.4: Typical turbine efficiency curve. The dotted line represents a higher exhaust manifold pressure.

[20]

$$U_t = 0.5d_t\omega_{tc} \quad (4.26)$$

$$C_s = \sqrt{2c_p T_{em} \left[1 - \left(\frac{p_{em}}{p_{ep}} \right)^{\frac{1-\kappa_e}{\kappa_e}} \right]} \quad (4.27)$$

and d_t is the turbine blade diameter and ω_{tc} the turbocharger angular frequency. A qualitative example of a turbine efficiency curve is given in Figure 4.4, resembling that of [29, Fig.9] and [30, Fig. 6-56]. The peak efficiency can take place in the region $0.4 < U_t/C_s < 0.8$ depending on turbine design and application [30]. The turbine isentropic efficiency can therefore be approximated by a simple model on the form

$$\eta_t = \eta_{t,\max} \left[1 - c_t \left(\frac{U_t}{C_s} - \frac{U_t}{C_s} \Big|_{\max} \right)^2 \right] \quad (4.28)$$

where c_t is a model parameter and $\frac{U_t}{C_s} \Big|_{\max}$ is the blade speed ratio corresponding to the maximum turbine efficiency. Since the values of the two parameters c_t and $\frac{U_t}{C_s} \Big|_{\max}$ are unknown, they are adjusted to provide good simulation performance. The efficiency is dependent on the pressure ratio in addition to blade speed ratio, a higher pressure ratio gives a slightly less efficient turbine. The effect of varying pressure is, however, small so for our general purpose model it can be neglected.

4.4 Concluding Remarks

- Turbine flow rate was reproduced by fitting a flow model to the turbine flow rate map supplied by a turbocharger manufacturer. Three different turbine flow models were suggested. One failed due to premature choking while the two others gave pleasing results.
- A modification of the mass flow calculation was performed due to numerical problems arising from pressure ratios close to unity.
- A general purpose approach to efficiency modeling was done as no turbine efficiency map was obtained. The outcome of the model has to be verified in upcoming engine simulations.

Chapter 5

Propeller, Ship and Engine

To control the marine propulsion engine one must have an idea on how the propeller load behaves. It is difficult to properly control the engine speed without knowledge of the applied load. To calculate how much load the propeller incurs the propellers speed of advance must be known. A ship surge model must then be included as the propeller advance speed relies on the speed and shape of the ship.

This chapter starts with modeling the propeller. Next, a simple model for the ship surge is developed. And lastly, parts of the engine model that lacked in the previous work is added. This includes an intercooler, shaft friction and overload control via a torque and scavenging air limiter.

5.1 Interaction of Submodels

The exchange of signals between the substructures of the total marine propulsion system is shown in Figure 5.1. From the fuel index (u) the engine states are calculated. The propeller uses the speed of revolution from the engine (n) to calculate the load torque (Q_p). Additionally the propeller's advance speed is needed to calculate the torque and thrust (T_p) of the propeller. This is found from the ship velocity (V_s). The propeller load torque is then used to recalculate the engine speed, and the propeller thrust to decide a new ship speed.

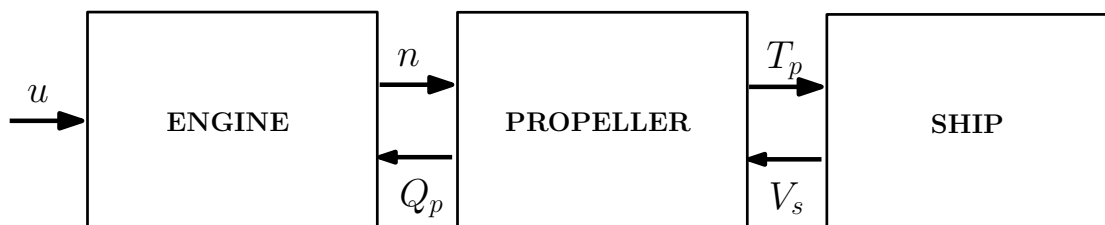


Figure 5.1: Interaction the simulation model subsystems.

5.2 Propeller Modeling

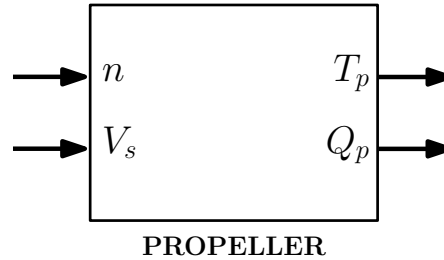


Figure 5.2: Inputs and outputs of the propeller model.

This section explains how the propeller is modeled. The propeller thrust and load torque is calculated from the shaft speed and ship velocity. The Wageningen B-screw series is chosen as the propeller of choice for the reason that it is perhaps the most extensive and widely used subcavitating open-propeller series [7], and therefore experimental data was easily available.

Propellers are usually designed to produce thrust in one direction, i.e. propel the ship ahead. Nonetheless, the ship sometimes has to produce thrust in the reverse direction, propelling the ship astern. Furthermore the propeller may be used to decelerate by running in the opposite direction of the advance speed. The four quadrants of propeller operation is decided by the positive or negative advanced speed (V_a) and by the positive or negative propeller rotation (n), see Table 5.1. Only the most regular propulsion situation for normal forward propulsion will be examined, i.e. situations with positive propeller speed ($n \geq 0$) and positive advance speed ($V_a \geq 0$).

Table 5.1: Propeller quadrants of operation.

	1	2	3	4
n	≥ 0	< 0	< 0	≥ 0
V_a	≥ 0	≥ 0	< 0	< 0

5.2.1 Thrust and Torque

The equations for propeller produced thrust and torque, (2.11) and (2.12), are repeated here for convenience

$$T_p = K_T \rho D^4 n^2 \quad (5.1)$$

$$Q_p = K_Q \rho D^5 n^2 \quad (5.2)$$

Table 5.2: Propeller geometrical data.

D	Z	P/D	A_E/A_O
6.5m	5	0.665	0.57

The unknown variables are the dimensionless thrust and torque coefficients

$$K_T = \frac{T_p}{\rho D^4 n^2} \quad (5.3)$$

$$K_Q = \frac{Q_p}{\rho D^5 n^2} \quad (5.4)$$

The open water characteristics of the Wageningen B-series has been found to be adequately represented by the following polynomial (for a Reynolds number of 2×10^6) [7]

$$K_T = \sum_{n=1}^{39} C_n(J_a)^{S_n}(P/D)^{t_n}(A_E/A_O)^{u_n} Z^{v_n} \quad (5.5)$$

$$K_Q = \sum_{n=1}^{47} C_n(J_a)^{S_n}(P/D)^{t_n}(A_E/A_O)^{u_n} Z^{v_n} \quad (5.6)$$

Where C_n are polynomial coefficients, J_a is the propeller advance coefficient, P/D the propeller pitch to diameter ratio, A_E/A_O the disk area coefficient and Z is the number of propeller blades. The polynomial coefficients C_n are given in Table B.5 in Appendix B. Figure 5.3 shows the open-water characteristics for a propeller with the propeller data presented in Table 5.2

The largest values of K_T and K_Q occurs when $J = 0$, i.e. when the propeller is revolving without advancing through the water. The open water efficiency η_0 is zero when the propeller operates with zero or 100 percent slip.

Example 5.1. *The large power and torque fluctuations for a real operating situation can be illustrated by plotting the thrust for three different thrust coefficient values K_T arising from different operating conditions. First we assume bollard pull conditions, $J_a = 0$*

$$\begin{aligned} T_0 &= K_T(0)\rho_w D^4 n^2 \\ &= 0.2896 \cdot 1.025 \cdot 6.5^4 \cdot n^2 \\ &= 529.80n^2 \end{aligned}$$

given in [kN]. Next we assume an increase in vessel speed leading to an advance coefficient of $J_a = 0.3$

$$\begin{aligned} T_1 &= K_T(0.3)\rho_w D^4 n^2 \\ &= 0.1956 \cdot 1.025 \cdot 6.5^4 \cdot n^2 \\ &= 357.85n^2 \end{aligned}$$

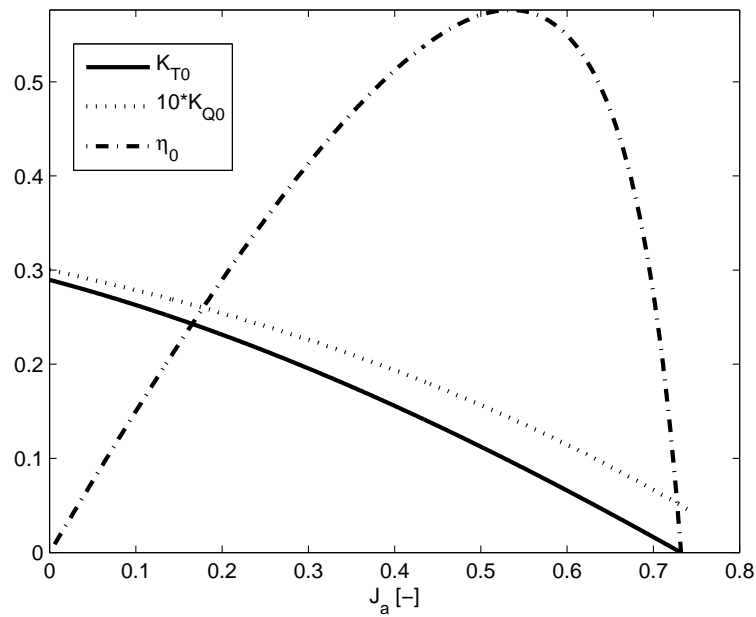


Figure 5.3: Open-water characteristics for a Wageningen B propeller with $D = 6.5\text{m}$, $Z = 5$, $P/D = 0.665$, $A_E/A_O = 0.57$ and $R_n = 2 \times 10^6$.

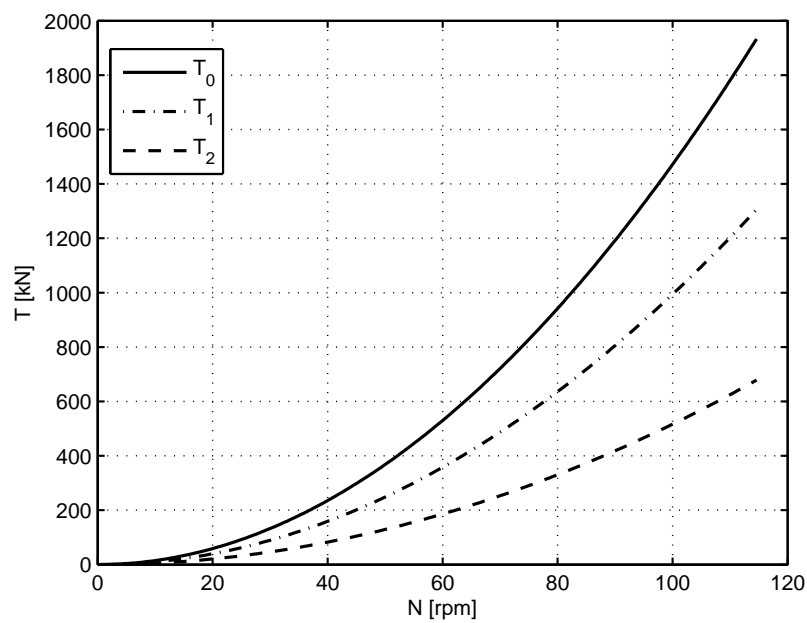


Figure 5.4: Propeller thrust characteristics for $K_{T0} = 0.2896$, $K_{T1} = 0.1956$ and $K_{T2} = 0.1016$.

Finally we assume full speed ahead and a calm weather situation giving $K_T = 0.101$

$$\begin{aligned} T_2 &= K_T \rho_w D^4 n^2 \\ &= 0.1016 \cdot 1.025 \cdot 6.5^4 \cdot n^2 \\ &= 120.45n^2 \end{aligned}$$

The three propeller load curves are shown in Figure 5.4. It is seen that a change in the propeller thrust coefficient has a large influence on the generated thrust.

Remark 5.1. The thrust and torque coefficients may be written as

$$K_Q = \frac{Q}{\rho n^2 D^5} = \frac{Q}{\rho V_a^2 D^3} \quad (5.7)$$

showing the disadvantage of becoming infinity for $V_a = 0$, which may occur in practice such as for a tug pulling at a stationary bollard or ship. These situations will however not occur in the simulation. Another representation of the propeller torque and thrust being continuous for V_a can be found in [11].

Remark 5.2. During simulation the values of K_T and K_Q are found from pre-calculation of the polynomials (5.5) and (5.6) and performing linear interpolation from the generated tables. Performing on-line calculations of the polynomials for each time step make for an unnecessary computational burden. By contrast to the compressor map, the propeller thrust and torque coefficient has nearly linear behavior, thus interpolation will not create the same discrepancies as with the nonlinear compressor map curves.

5.2.2 Propeller Inertia

Propellers traveling in water has properties arising from interaction with the water, leading to an augmentation of their volumetric mass properties. In the axial direction the propeller carries water along with it as the ship moves forward, causing an element of added mass in the longitudinal motion. There is also an element of added mass in the axial direction, because the propeller carries the water with the blades as it rotates. Thus giving rise to an added moment of inertia. The total mass of the propeller is therefore the sum of the propeller mass (m_p) and the added mass of the entrained water (m_{ew}). The total moment of inertia is that of the propeller itself (J_p) plus the *entrained water inertia* (J_{ew}).

The mass moment of inertia of the propeller can easily be found by volumetric calculations. The entrained water inertia, on the other hand, varies according to the current propeller environment. The variation of the entrained water inertia is in the range 5-30% of the propellers inertia in air [28]. Propellers with a small blade area ratio or pitch will be in the lower end, while propellers with high blade area or pitch will normally be in the upper end.

The propeller's entrained water inertia is calculated according to the Schwanecke's estimates [31]

$$J_{ew} = \frac{0.0703(P/D)^2(EAR)^2}{\pi Z} \rho_w D^5 \quad (5.8)$$

The total inertia of the shafting system is that of the engine, the propeller and the entrained water

$$J_{tot} = J_e + J_p + J_{ew} \quad (5.9)$$

5.3 Ship Surge Model



Figure 5.5: Inputs and outputs of the ship model.

A forward speed model for the ship is [32]

$$(M_s + M_a)\dot{V}_s = (1 - t_d)T_p - R_T(V_s) - T_{ext} \quad (5.10)$$

where M_s is the ship's mass, M_a is the added mass (hydrodynamic force) due to acceleration of a body in water, V_s is the speed of the ship, T_p is the propeller generated thrust, t_d the thrust deduction coefficient, T_{ext} external forces due to weather conditions and fouling and R_T is the total ship towing resistance. Ship speed is usually measured in knots which is equal to one nautical mile per hour.

$$[\text{kn}] = \frac{1852}{3600} [\text{m/s}] \quad (5.11)$$

Remark 5.3. *The added mass is set to a fraction of the ship mass. The real dynamics of added mass are complicated, while the purpose of the surge model is only to get the ship speed to help in calculating the propeller load. A more detailed explanation of added mass calculations can for example be found in Fossen [33]. An incorrect added mass will only affect the time constant of the ship's surge speed response, not the steady state value.*

The friction, residual and air resistance can be merged and the total ship resistance can then be written as a function of ship speed V_s , surface area S , water density ρ_w and the resistance coefficient C_T .

$$R_T = 0.5C_T\rho_wSV_s^2 \quad (5.12)$$

Table 5.3: Ship data for a large “Handymax” type bulk carrier [3].

Parameter	Symbol	Value	Unit
Size (at scantling draught)		55000	dwt
Length overall	L_{oa}	190	m
Length between perpendiculars	L_{pp}	183	m
Breadth	B	32.26	m
Draught (scantling)	D_s	12.7	m
Draught (design)	D_d	11.5	m
Mass	M_s	6.358×10^6	kg
Added mass	M_a	$0.25M_s$	kg

The number of parameters can be reduced by introducing the new coefficient \hat{C}_T

$$\hat{C}_T = 0.5C_T\rho_w S \quad (5.13)$$

Giving

$$R_T = \hat{C}_T V_s^2 \quad (5.14)$$

The resistance coefficient \hat{C}_T can be estimated by calculating the resistance at the a typical design ship speed of $V_{s,\max} = 15$ knots. At this maximum speed, the ship is in steady state

$$\dot{V}_s = 0 \quad (5.15)$$

Inserting equations (5.14), (5.15) and $T_{\text{ext}} = 0$ (calm weather) into (5.10) gives

$$(1 - t_d)T_p = \hat{C}_T V_{s,\max}^2 \quad (5.16)$$

Rearranging for \hat{C}_T gives

$$\hat{C}_T = \frac{(1 - t_d)T_p}{V_{s,\max}^2} = \frac{(1 - t_d)K_T(J_a)\rho_w D^4 n_{mcr}^2}{V_{s,\max}^2} \quad (5.17)$$

where n_{mcr} is the maximum propeller revolutions [r/s], and K_T is found from (5.5) with the following advance coefficient

$$J_a = \frac{(1 - w)V_{s,\max}}{n_{mcr}D} \quad (5.18)$$

5.4 Engine Model Extensions

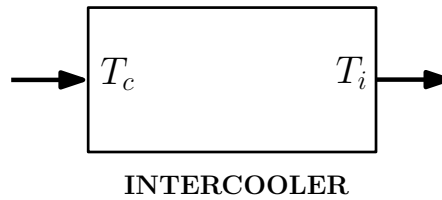
The engine mean value model is extended with the inclusion of an intercooler, shaft friction and overload protection by means of a torque limiter and a scavenge air pressure limiter.

Engine parameters are given in Table 5.4. The exhaust pipe pressure is simplified by setting $p_{ep} = p_{amb}$ and exhaust pipe temperature $T_{ep} = 500$ K taken from the performance curves in Figure A.3.

Table 5.4: Engine parameters of a MAN 6L60MC mk6 marine diesel engine.

Parameter	Symbol	Value	Unit
MCR Power (L1)	P_{MCR}	11520	kW
MCR Speed (L1)	N_{MCR}	123	r/min
Specified MCR power	P_{SMCR}	9177	kW
Specified MCR speed	N_{SMCR}	114.7	r/min
Number of cylinders	z_c	6	
BMEP	\bar{p}_b	16	bar
Engine/propeller inertia	$J_e + J_p$	59800	kg m ²

5.4.1 Intercooler

**Figure 5.6:** Inputs and outputs of the intercooler.

The intercooler is a heat exchanger used to cool the heated compressed air back to near ambient temperature. The intercooler increases the air density, which is advantageous for combustion. In the previous work an intercooler was not included, leading to an increased intake manifold temperature. This again led to an increased exhaust manifold temperature and consequently a raised exhaust gas enthalpy. By not including an intercooler the turbine torque will be unrealistically high, thus provoking an excessive turbocharger speed. The efficiency of a heat exchanger is given by [27]

$$\eta_i = \frac{T_c - T_i}{T_c - T_w} \quad (5.19)$$

where T_c is the temperature after the compressor, T_i is the temperature after the intercooler and T_w the temperature of the cooling water. The efficiency is reduced with a higher engine load. This is a result of an enlarged air flow through the intercooler. A simple model including this matter can be

$$\eta_i = 1 - k_{ic}\dot{m}_a \quad (5.20)$$

where \dot{m}_a is the air flow to the cylinders and k_{ic} is a constant fitted to experimental data. For the reason that the intercooler efficiency is very high (above 90%) for most loads, the efficiency can be approximated by a constant without losing much accuracy. In fact $T_i \approx T_w$ anyhow. The model of the intercooler becomes

$$T_i = (1 - \eta_i)T_c + \eta_i T_w \quad (5.21)$$

where $\eta_i \approx 0.95$ is the constant intercooler efficiency. Note that a small pressure drop in the air pressure is incurred by the intercooler, however the pressure drop is small enough to be neglected [28].

5.4.2 Shaft Friction

The shaft dynamical equation is dependent on the engine torque Q_e and propeller load torque Q_p . Still, it can be further extended to incorporate shaft friction

$$\omega_e = \frac{Q_e - Q_p - Q_f(\omega_e)}{J_{tot}} \quad (5.22)$$

Shaft friction is a sum of static friction Q_s and a linear component depending on the shaft speed

$$Q_f(\omega_e) = Q_s + K_\omega \omega_e \quad (5.23)$$

5.4.3 Overload Protection

Engine overload protection is about limiting fuel input costumed to the current torque conditions and level of boost pressure. The two types of fuel limiters frequently encountered in marine diesel engines are the torque limiter and scavenge air pressure limiter.

Torque Limiter

The engine torque limiter decides a maximum allowed fuel rack index to sustain the mechanical limits of the engine. The following illustrates how torque and fuel rack index is related; Engine brake power is given by the product of engine torque and rotational frequency

$$P_b = Q_e \omega_e \quad (5.24)$$

which gives that torque is the fraction of power to speed

$$Q_e = \frac{P_b}{\omega_e} \quad (5.25)$$

For the reason that engine power is proportional to the fuel rack position, the torque can be large enough to damage the engine provided the engine speed is low. Consequently, a torque limiter must put a restrain on the fuel rack position according to the current engine speed. The torque limiter is in the following form

$$u_{\max} = \begin{cases} a, & n_m \leq c \text{ of } n_{mcr} \\ b, & n_m \geq d \text{ of } n_{mcr} \\ e \frac{n_m}{n_{mcr}} + f, & \text{otherwise} \end{cases} \quad (5.26)$$

Parameters e and f can be found from

$$e = \frac{b - a}{d - c} \quad (5.27)$$

$$f = b - de \quad (5.28)$$

The following values are implemented in the engine and illustrated in Figure 5.7

$$u_{\max} = \begin{cases} 0.4, & n_m \leq 40\% \text{ of } n_{mcr} \\ 1, & n_m \geq 80\% \text{ of } n_{mcr} \\ \frac{1.5n_m}{n_{mcr}} - 0.2, & \text{otherwise} \end{cases} \quad (5.29)$$

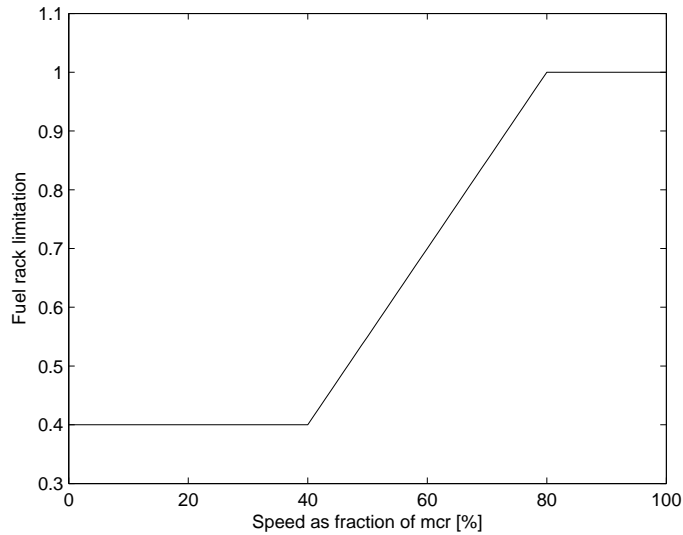


Figure 5.7: Torque limiter.

Scavenging Air Fuel Limiter

The scavenge air pressure limiter ensures that air-fuel ratio is maintained at sufficient values to retain perfect combustion and to avoid high thermal stresses in the engine. Additionally it averts environmentally hazardous smoke and emissions.

In similar fashion as the torque limiter, the scavenge air limiter can be found by supplying two limits (a, b) for two input manifold pressure ratios (c, d)

$$u_{\max} = \begin{cases} a, & \Pi_c \leq c \\ b, & \Pi_c \geq d \\ e\Pi_c + f, & \text{otherwise} \end{cases} \quad (5.30)$$

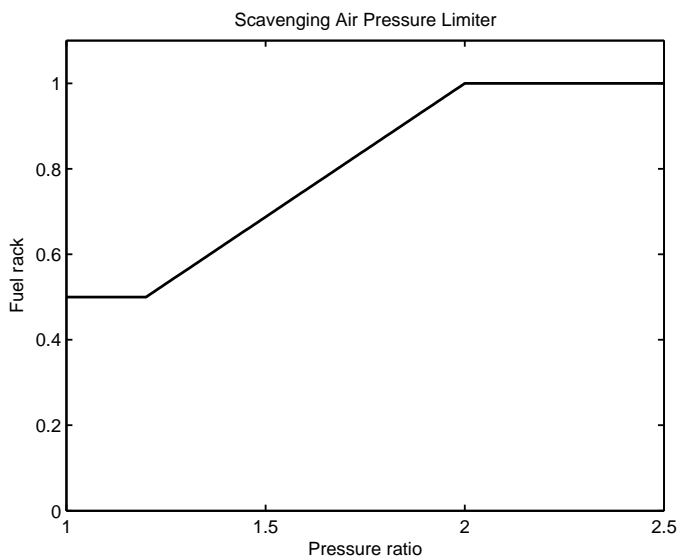


Figure 5.8: Scavenging air pressure limiter.

The linear correspondence between the points can be found by

$$e = \frac{b - a}{d - c} \quad (5.31)$$

$$f = b - de \quad (5.32)$$

Figure 5.8 shows a limiter with the following parameters

$$u_{\max} = \begin{cases} 0.5, & \Pi_c \leq 1.2 \\ 1, & \Pi_c \geq 2.0 \\ 0.625\Pi_c - 0.25, & \text{otherwise} \end{cases} \quad (5.33)$$

Remark 5.4. *Engine developers usually provide the limiter values. Since none was obtained, the limiters are chosen at best guess.*

Chapter 6

Simulation of Engine and Turbocharger

As the engine is extended with new features and the turbocharger is fitted to a performance map by a novel approach, validation of the model is done by simulating the engine and turbocharger responses. First the response is investigated by applying small steps in the fuel rack position. Next, a larger fuel rack step is applied to examine how the engine reacts to low air-to-fuel ratios and how limiters are incorporated to prohibit torque loss due to insufficient air flow.

Simulation is performed in Matlab and Simulink version R2010b, with a variable step ode45 (Dormand-Prince) solver. All simulation parameters are given in the initialization file included in Appendix C.

6.1 Step Responses

The engine steady state performance is examined by adjusting the fuel index from 30-100% in steps of 10%. The intent is to verify the engine and turbocharger systems, therefore propeller and ship subsystems are neglected. Engine load is determined by the theoretical propeller curve

$$Q_l = K_Q N_e^2 \quad (6.1)$$

where the torque coefficient K_Q [Nm/(r/min)²] can be found by

$$K_Q = \frac{Q_{\text{mcr}}}{N_{\text{mcr}}^2} = \frac{60 P_{\text{mcr}}}{2\pi N_{\text{mcr}}^3} \quad (6.2)$$

The overall Simulink diagram for the engine step response simulation is seen in Figure 6.1. The engine and load subsystems are implemented using embedded Matlab functions. Discussion of the simulation results given in Figure 6.2 follows;

- As the fuel rack index is increased the engine bmep grows and accordingly the produced torque increases. With extra torque the engine accelerates and

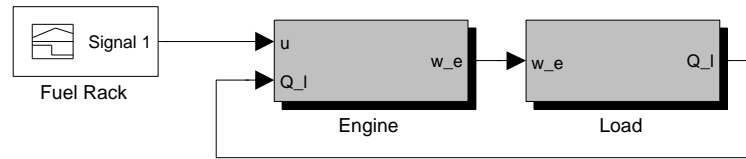


Figure 6.1: Simulink diagram for engine step responses with standard propeller curve load.

speed increases. An adjustment of the fuel rack from $u = 0.3$ to $u = 0.4$ gives an additional speed of $71.3 - 61.4 = 9.9$ r/min. A change from $u = 0.9$ to $u = 1$, on the other hand, increases speed by only $114.5 - 105.5 = 6$ r/min. Surely a higher initial engine speed reduces the effect of a fuel increase. The change in fuel rack causes a nonlinear speed response. This is mainly due to the fact that produced engine torque is modeled as linear in bmep and load torque is a function of the squared engine speed.

- With more fuel injected in the cylinders, exhaust gas enthalpy increases and turbine torque grows. The increased driving torque results in an acceleration of the turbocharger. Additionally, the extra fuel in combustion gives an increased exhaust gas temperature, and consequently a higher exhaust manifold temperature. Compared with the engine performance curves in Figure A.3 in Appendix A, it is observed that the exhaust manifold temperature (inlet to turbine) in simulation (710 K) is larger than in the performance curves (660 K). The discrepancy can be justified by a lack of exhaust manifold heat loss in the simulation model. With exhaust manifold temperature being quite large compared with the ambient temperature, heat loss should be implicated. In contrast, heat loss of the intake manifold and the surrounding volumes can be neglected due to the lower compressor temperatures and the high intercooler efficiency. This leads to a insignificant temperature difference between the intake manifold and ambient.
- Transient response of the exhaust manifold temperatures can be seen in light of the air-to-fuel ratio. A step in fuel rack position gives an instantaneous increase of fuel in the cylinders. Unlike the fuel, the turbocharger speed and the mass flow rate are not instantaneously increased due to the turbocharger inertia. As a result, the air-to-fuel ratio decreases immediately as the fuel rack is changed. A lower air-fuel ratio provokes a higher exhaust temperature, which again accelerates the turbocharger. With increased turbocharger speed more air is provided and the air-fuel ratio increases. Eventually, the air-fuel ratio, exhaust temperature and turbocharger speed attains new steady state values. Xiros [28] states that typical steady state air-fuel ratios are in the region of 30-40. Simulation shows that the same ratios are obtained for the high end loads. If the engine operating point was not

reduced, even more fuel could be injected and the air-fuel ratios would be more in the 30-40 region for all loads. Indeed the turbocharger supply the engine with an adequate amount of air in steady state and during small fuel rack changes. Engine response to a large fuel rack step will be investigated in the following section.

- At low fuel rack positions ($u = 0.3$ and $u = 0.4$) the simulated turbocharger speed is below the minimal speed provided in the compressor map

$$U_{c,\min} = 250 \text{ m/s} \quad (6.3)$$

$$\Downarrow$$

$$N_{tc,\min} = 9549 \text{ r/min} \quad (6.4)$$

It is therefore essential that the compressor model developed in Chapter 3 has good extrapolation capabilities for low load scenarios. It is observed that compressor mass flow rate and pressure ratio achieve sensible values from simulation under these circumstances. Due to the sufficing compressor performance during extrapolation, the engine model on the whole seem to behave satisfactorily during low load scenarios.

Figure 6.3 shows the compressor map with a steady state load line. The steady state line represent fuel rack values from $u = 0.3$ to $u = 1.1$. It is seen that the 6L60MC engine gives a load line similar to the load line of the smaller 6S46MC engine in the provided map. However, for a fuel rack value $u = 1.1$ the speed of the turbocharger exceeds that of the maximum permissible speed of the TCA55 turbocharger at 20000 r/min. Thus, for a 6L60MC engine without a reduced SMCR the turbocharger is too small. This is also emphasized by the fact that engine/turbocharger selection guides suggests the larger TCA66 for the simulated engine.

In addition, extrapolation for compressor efficiency seem to execute convincingly. A drop in efficiency is anticipated at lower speed, but it still maintains a fairly high value and does not collapse, which could be a problem when using a high polynomial for the efficiency fit.

- The ad hoc approach used for the turbine efficiency provides decent results. Compared to the compressor, the turbine efficiency behaves almost equally.

Remark 6.1. *It should be noted that simulation performance of the engine is not directly comparable with the engine performance curves given in the Appendix. This is a result of the engine in simulation not running at full nominal MCR and that a 100% fuel rack does not coincide for the two engine setups. Furthermore, the performance curves are for a newer engine version. Hence, the performance curves would be assumed to give stronger results.*

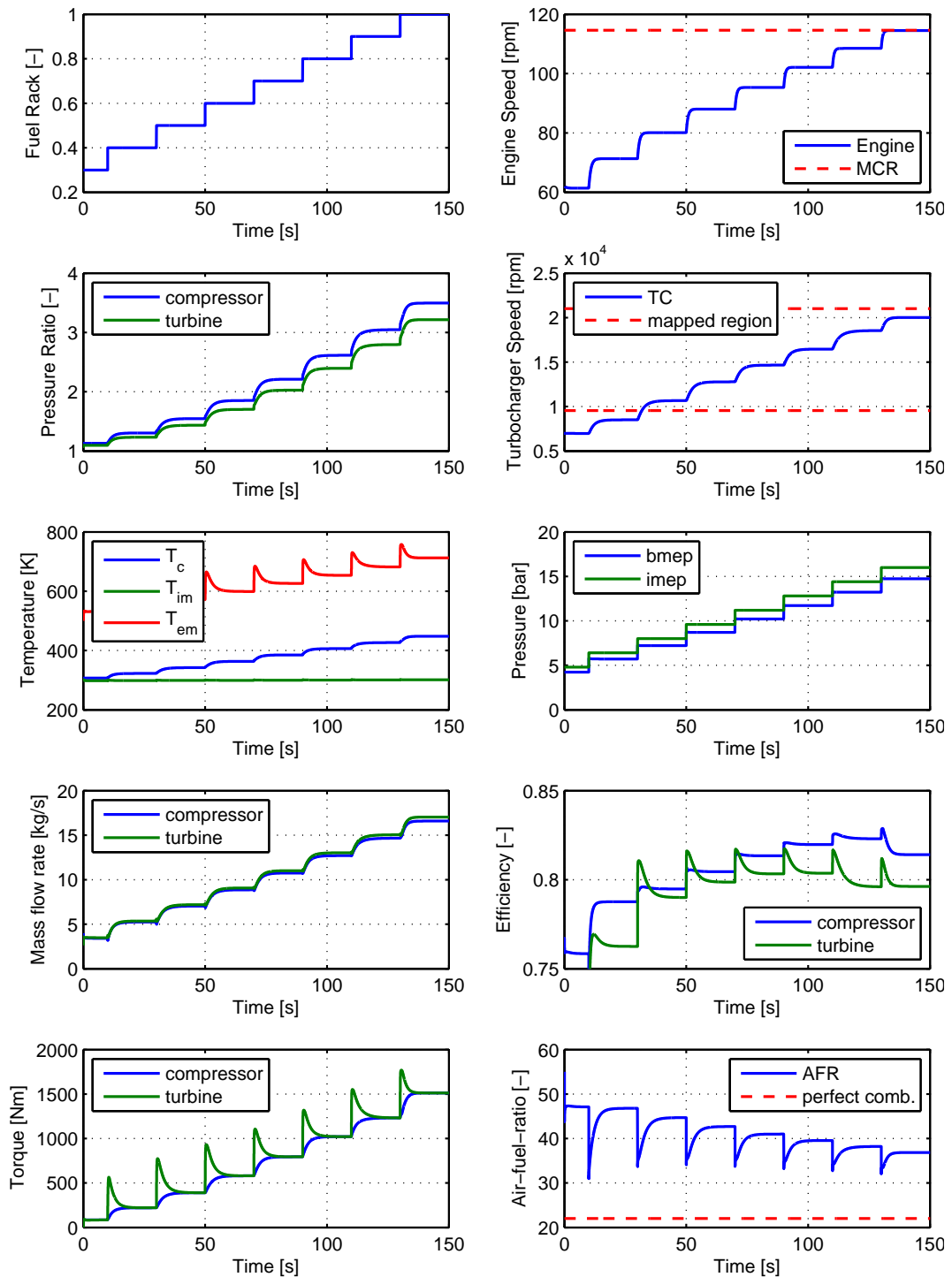


Figure 6.2: Simulation of the engine and turbocharger with the load following a theoretical propeller curve.

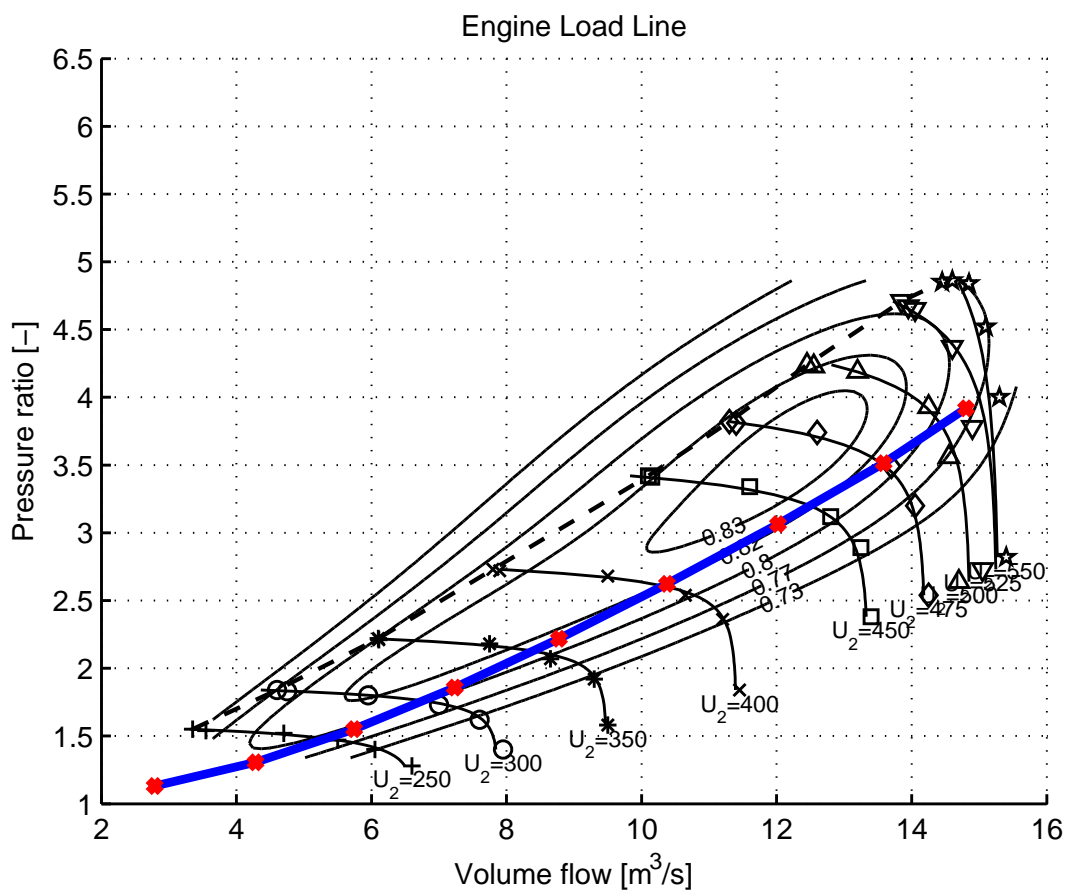


Figure 6.3: Compressor steady state load line. Samples represent fuel rack positions 0.3, 0.4, ..., 1.1.

6.2 Fuel Limiters

6.2.1 Inactive Limiters

The following simulation scenario illustrates the effect of a large step in fuel rack from $u = 0.3$ to $u = 1.0$ at $t = 5$ s with *disengaged* fuel limiters. The results of the simulation are given in Figure 6.4.

- The plots demonstrate that at the moment the fuel rack step is applied the air-to-fuel ratio dips beneath the perfect combustion limit at $\text{AFR} = 22$. Such a rapid adjustment of fuel rack index is, however, unrealistic for conventional engine practice. Large load changes does not take place in such a limited period of time. Nevertheless, at times of heavy acceleration, similar tendencies will occur. The lack of air in the cylinders results in degraded combustion and decreased engine torque. The produced engine torque with the current air-fuel ratio is lower than the load torque, leading to a retardation of the engine speed from 61.5 r/min to 58.5 r/min. A decreased compressor mass flow rate is also observed.

The additional fuel energy makes the turbine torque increase and the turbocharger accelerate, regardless of the engine speed being decreased. As the turbocharger speed increases more air is drawn into the cylinders and the air-to-fuel ratio begins to recover. Perfect combustion is regained after some 2 – 3 s and normal engine response is resumed. The higher the turbocharger inertia, the slower the response is and the more severe the lack of air becomes.

- The nonlinearity of the engine process can be perceived in the transient response. The shape of the speed response is reliant upon the amplitude of the response. For instance, the shape of the speed response differs between the large step in this simulation and the previous simulation with smaller fuel rack index steps. This implies latent dynamical terms activated under certain transient conditions [28]. Due to the inference of the air-fuel ratio the rise time for the plant signals depends upon the amplitude of the step. This is emphasized under scenarios with fuel limiters included, as seen next.

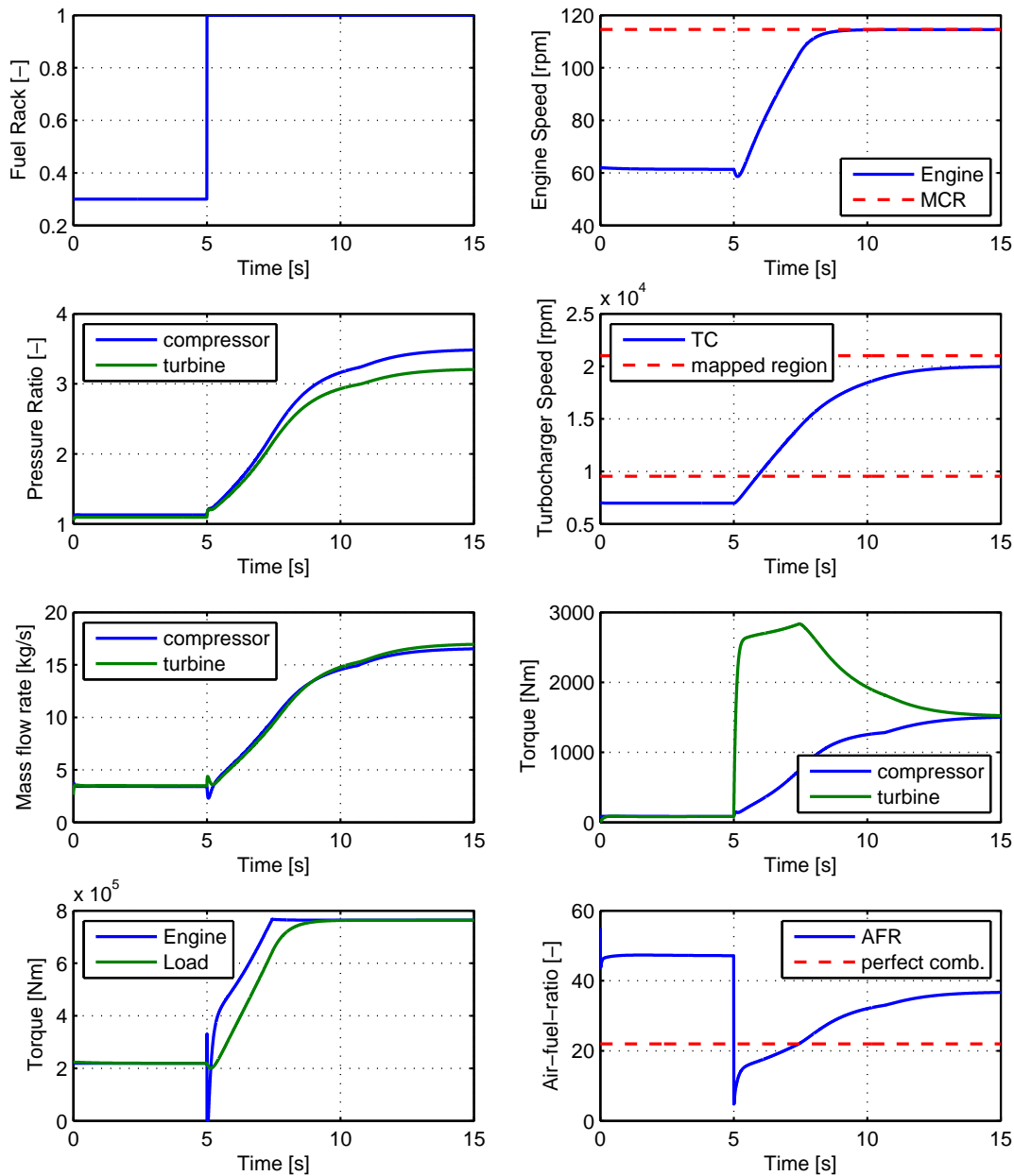


Figure 6.4: Simulation of the engine/turbocharger response for a fuel rack step from $u = 0.3$ to $u = 1.0$ with *inactive* fuel limiters.

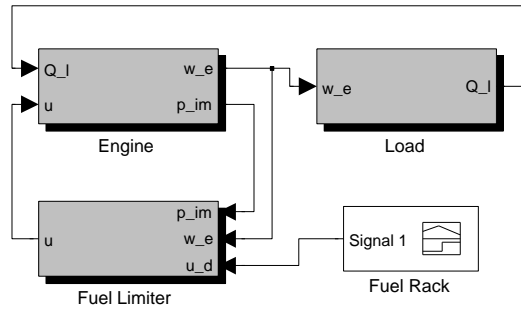


Figure 6.5: Simulink diagram of the simulation model with fuel limiters included .

6.2.2 Active Limiters

For the next scenario, two fuel limiters are incorporated in the simulation. The fuel limiter based on engine torque is to sustain the mechanical limits of the engine. The scavenge air limiter ensures that air-fuel ratio is maintained to retain perfect combustion and to avoid thermal stresses of the engine. The overall simulation diagram is shown in Figure 6.5. Simulation results with active fuel limiters are seen in Figure 6.6.

- The same step from $u = 0.3$ to $u = 1.0$ at $t = 5$ s is given as input to the system. However, the response is not the same as the limiters restrains the fuel rack step. At 5 s the insufficient boost pressure limits the step from $u = 0.3$ to $u = 0.5$. Gradually as the compressor pressure ration builds up more fuel is allowed. As a consequence, engine speed response is slowed down compared with the previous simulation. A positive note is that air-fuel ratio is maintained at perfect combustion values and black smoke and engine torque reduction is prevented.
- In simulations, the response of the engine has been examined at instantaneous steps in the supplied fuel to the cylinders. In reality, and change of fuel rack does not expedite an instantaneous change of delivered fuel. Firstly, the fuel according to the index must wait for the next cylinder to position itself at the crank angle where injection starts,

$$\tau \leq \frac{2\pi}{z_c \omega_e} \quad (6.5)$$

Moreover, the injection persists for a specified time (rotation) and combustion must take place. These two events lasts in total less than one fourth of a cycle

$$\tau \leq \frac{2\pi}{4\omega_e} \quad (6.6)$$

The maximum injection dead time is therefore

$$\tau \leq \frac{2\pi}{z_c \omega_e} + \frac{2\pi}{4\omega_e} \quad (6.7)$$

However, as the engine is a mean value model, the average value over one whole rotation is examined. The time delay is always less than one rotation

$$\tau < \frac{2\pi}{\omega_e}, \forall z_c \geq 2 \quad (6.8)$$

Hence, the engine torque delay can be neglected for the reason that the dead time is less than the sampling step of the model.

- In addition to dead time for generating torque, the fuel pumps have a dynamic response to a change of index. In control oriented models the actuator dynamics are usually implemented as a first order differential equation with time constant T_a , the transfer function of the actuator becomes

$$G_a(s) = \frac{1}{T_a s + 1} \quad (6.9)$$

However, as modern diesel engine fuel pumps are very fast and fuel index changes are usually rather small, the time delay due to actuator dynamics can be neglected. In fact, the same argument as above, with the sampling time being one revolution, still applies.

6.3 Concluding Remarks

- Performance of the combined engine and turbocharger subsystems was examined. Simulation showed that nonlinear properties of the engine is prominent, especially during large fuel changes and low air-to-fuel ratios.
- It is discovered that heat loss in the exhaust manifold should be included due to high temperature differences between the ambient and the exhaust manifold.
- For the reason that the model is a mean value model actuator dynamics and injection dead time can be neglected.
- At low engine load the turbocharger speed falls below the limit of the reference compressor map. The extrapolation proficiency of the developed compressor flow and efficiency models show to cope with the hindrance and the engine succeeds to provide good results in this uncharted speed region. In fact, performance for all turbocharger speeds is excellent.

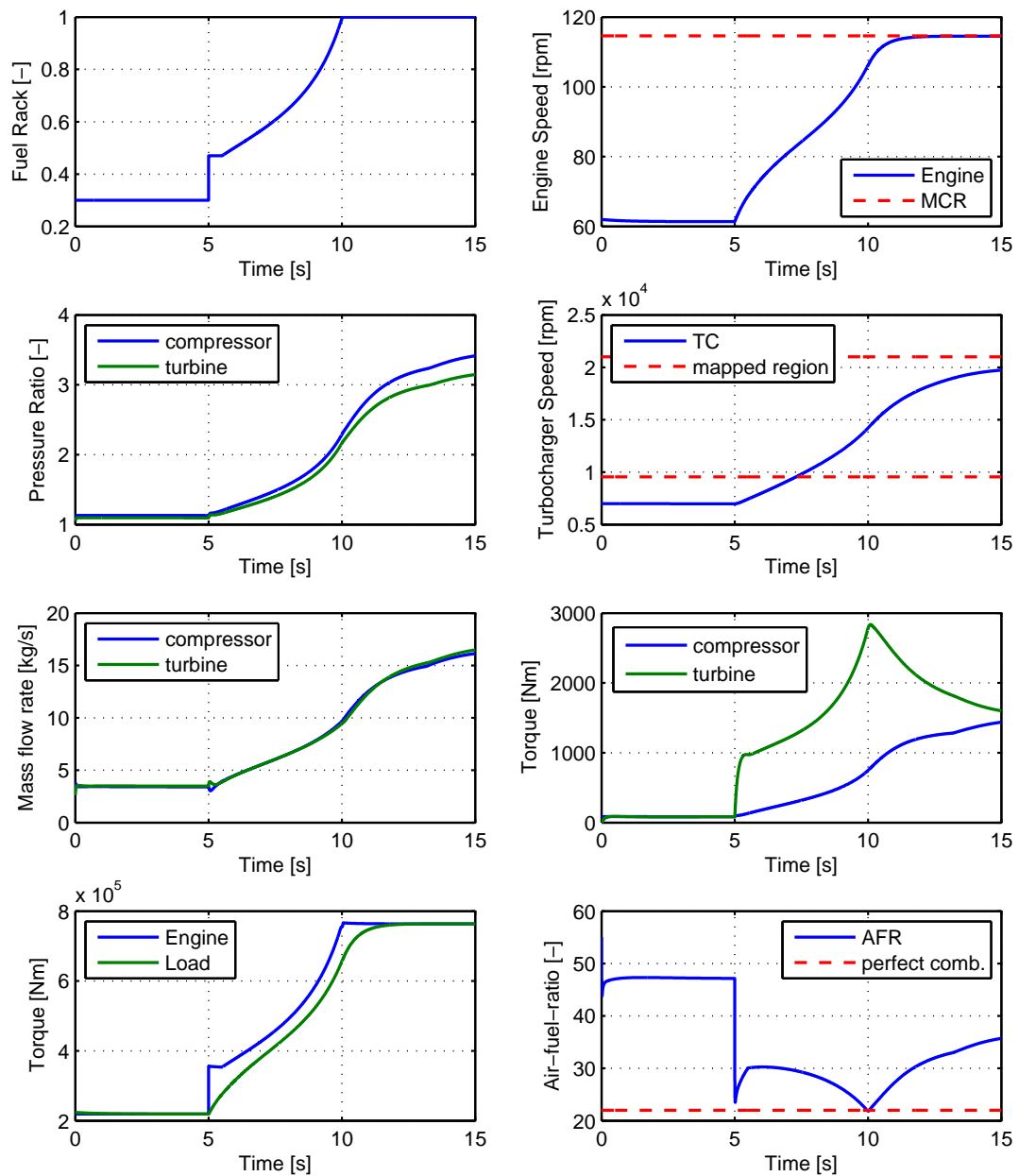


Figure 6.6: Simulation of the engine/turbocharger response for a fuel rack step from $u = 0.3$ to $u = 1.0$ with *active* fuel limiters.

- Fuel limiters showed to effectively avoid low air-to-fuel ratios and degeneration of torque at large fuel index steps. This is averted by reducing the fuel according to boost pressure (air flow). Nonetheless, the response time of the engine increases.
- Overall, performance of the engine and turbocharger is in accordance with the anticipated response.

Chapter 7

Control

Control of the engine is important to achieve the desired engine speed, avoid critical overspeed during load torque loss, minimize fuel consumption, achieve increased air-fuel ratio, avoid compressor surge, avoid excessive pollution, provide the ship with the required thrust, suppress varying environmental conditions and to provide a smooth and safe operation of the engine.

The mean value engine model developed in the specialization project [4], and further extended in this thesis, works as a basis for controller synthesis. The analysis of the uncontrolled simulation model helped gaining knowledge of the process and illuminates possible control strategies. Furthermore, the modeling approach revealed effects to be wary of, e.g. varying propeller inertia and time delay effects introduced by a turbocharger when accelerating.

This chapter starts with the implementation of a PI controller for engine speed and further provides simulation of the speed controlled engine in an environment including the ship and propeller.

7.1 Linear PI Controller

To control the engine speed a PI controller is used on the the shaft speed error

$$e(t) = N_d(t) - N_e(t) \quad (7.1)$$

where N_d is the desired shaft speed and N_e is the measured engine shaft speed. The PI controller equation is

$$\dot{u}(t) = K_p e(t) + K_i \int_{t_0}^t e(\tau) d\tau \quad (7.2)$$

or equivalently the Laplace transform

$$u(s) = \left(K_p + \frac{K_i}{s} \right) e(s) \quad (7.3)$$

Controller gains are the proportional gain K_p and the integral gain K_i . For the reason that the fuel index is limited between 0 and 1

$$u \in [0, 1] \quad (7.4)$$

integral anti-windup has to be included. When the minimum or maximum fuel rack limit is reached the feedback loop is broken and the plant remains independent of the speed measurement. If integral anti-windup is not included the error continues to be integrated regardless of the saturated actuator. As a result, the integrator will grow in size, or “wind up”. When the actuator desaturates and the error changes sign the system will take a long time to recover, it has to “wind down”. This leads to the fuel rack remaining at min/max until the integrated error is again integrated away. The effect is that the controller response becomes delayed and the actuator output during the wind-down may destabilize the system. To avoid integrator windup the difference between the controller output and the actuator output is fed back with an anti windup gain K_w . The block diagram for the PI-controller with anti-windup is seen in Figure 7.1.

Remark 7.1. *The derivative (D) term of the PID controller is excluded to avoid noise amplification (which can occur with noisy propeller torque and erroneous speed measurements) and to obtain robustness in the commanded speed.*

Remark 7.2. *The PI controller is a linear controller and the engine model is nonlinear. Therefore some controller parameters that work good at full load might give poor performance (or even be unstable) for low load. Optimally, the controller should be gain scheduled (using different controller gains in different operating regions). However, as parameter tuning is not the target of investigation for this simulation, gain scheduling and model linearization is ignored. Moreover, the set-point is varying slowly so the chance of potential instability is reduced.*

Table 7.1: Controller gains.

Gain	Value
K_p	1
K_i	0.1
K_w	1

7.2 Simulation

The PI speed controller is tested in a simulation involving the total ship propulsion system (Figure 7.2). The ship starts at full speed ahead (15 knots) with the engine

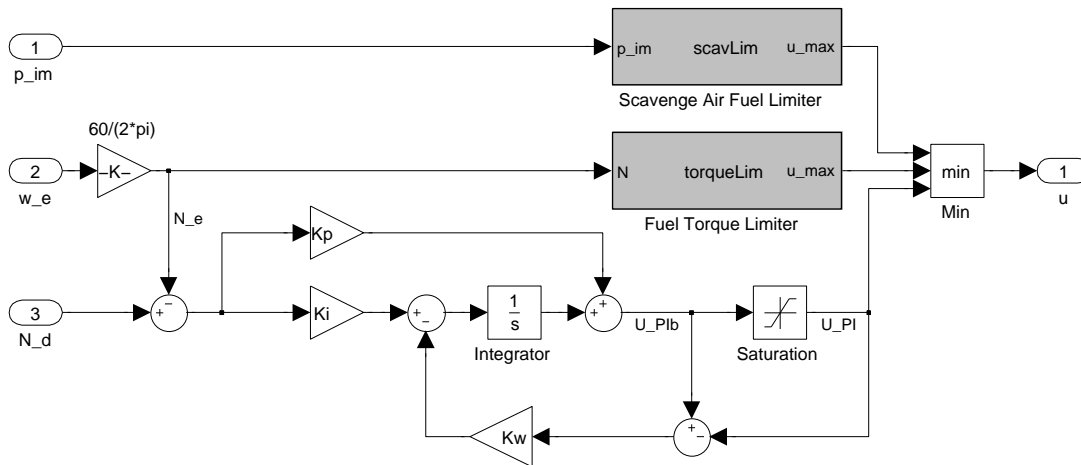


Figure 7.1: Simulink diagram of the engine governor. It includes a PI controller with integrator windup in addition to a scavenge air limiter and torque limiter (implemented as Matlab functions).

working at SMCR. Suddenly a storm blows up, giving rise to increased external resistance due to extra wind and wave resistance. The captain decides to slow down to a safe speed at $N_d = 85$ to avoid potential engine overspeed because of torque loss (large waves). After a while, the captain sees it safe to increase the speed back up to $N_d = 105$. The simulation events are summarized in Table 7.2. The results of the simulation are given in Figures 7.3 and 7.4

Table 7.2: Simulation events for a ship simulation with a PI controller for engine speed.

Event	Start time (s)	End time (s)
Full speed ahead ($N_d = 114.5$)	0	120
Resistance increase	120	180
Reduce speed	360	480
Constant engine speed ($N_d = 85$)	480	740
Increase speed	740	800
Constant engine speed ($N_d = 105$)	800	1000

- As the extra environmental resistance enters the system the total resistance on the ship grows, effectively slowing it down. The decreased ship velocity reduces the advance ratio of the propeller thus increasing the torque and thrust coefficients K_Q and K_T . With an increased torque coefficient the propeller load torque grows causing a reduced engine speed. Despite the engine slowing down, the produced thrust is seen to increase slightly due to the raised thrust coefficient. In total, the ship velocity decreases by almost 1 knot due to the external resistance.

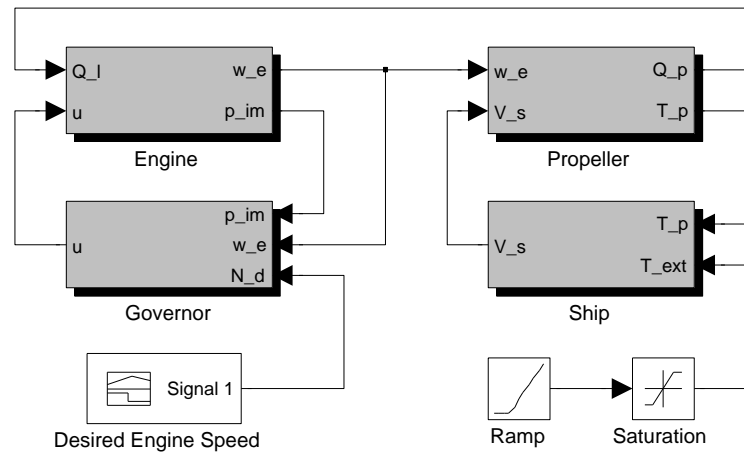


Figure 7.2: Simulink diagram for the engine/propeller/ship final simulation model.

- The slip ratio increases with the external resistance as the propeller load increases. This also leads to a lowered open water efficiency.
- As the ship resistance increases the controller can not keep up the desired engine speed at $N_d = 114.5$. The output of the PI controller is seen to grow to $u_{PI} \approx 1.2$. However, the output of the governor is $u = 1.0$ due to the limited fuel index position. Because of the integrator anti-windup feedback, the PI controller output is seen stop increasing after the engine comes to a steady state speed error. This is due to the integration reset time constant, which is the inverse anti-windup gain $\tau_w = 1/K_w$. Consequently, only a small portion of the total error is integrated. Therefore the PI-controller output is the proportional speed error plus a reduced integrated error.
- When the captain decides to gradually reduce the engine speed setpoint to $N_d = 85$ the PI-controller output returns to the value $u_{PI} = 1$ after about 1.5 s, in accordance to the anti-windup reset time constant. Without the anti-windup feedback the integrated error between $t = 120$ to $t = 360$ would have to be canceled by a corresponding negative error, thus the PI alone would give the fuel index $u = 1$ for quite some time after the setpoint is changed.
- As a result of the lowered engine speed setpoint the PI controller gives a smaller index, leading to less fuel in the cylinders. Reduced fuel gives reduced engine torque and consequently reduced engine speed. The engine speed decreases faster than the ship speed due to the slow ship surge dynamics. As a consequence, the propeller thrust falls behind the ship resistance and the ship decelerates to 10.3 knots.
- For the reason that propeller speed decreases faster than ship speed, the

propeller advance coefficient

$$J_a = \frac{V_a}{nD} \quad (7.5)$$

temporarily increases during rapid deceleration. This leads to a reduced slip ratio, which indicates a less loaded propeller. It also increases the open water efficiency. The opposite is observed during the acceleration phase ($t = 740$ to $t = 800$); the advance ratio temporarily decreases and the slip ratio increases as to indicate a heavily loaded propeller.

- The PI-controller follows the linear change in setpoint without problems. Further investigation and parameter tuning (and gain scheduling) for setpoint steps has to be done in future work.
- Investigation and control of propeller torque fluctuations are excluded in the thesis. This is a consequence of the analysis done of injection and actuator delays in the previous chapter. With an instant response in fuel and engine torque a controller would not have any problems suppressing load torque variations perfectly. Thus engine torque delays must be implemented for the analysis of propeller fluctuations and the overspeed problem.

Remark 7.3. *Fuel rack position of $u = 1.0$ corresponds to the specified MCR (SMCR point of the engine, not to the nominal MCR).*

7.3 Concluding Remarks

- Analysis of the transient behavior of a simulated ship process contributed to increased overall understanding of the dynamic performance of a propulsion plant and the interaction between the engine, turbocharger, ship and propeller.
- A PI engine speed controller with integrator anti-windup was implemented and proven successful in simulation. The anti-windup procedure prevented speed errors to be continuously integrated when the actuator was saturated.
- Linearization of the model and gain scheduling is proposed as future work as parameter tuning and step response analysis was not performed.
- Load fluctuations and overspeed could not be investigated as simplifications of the fuel dynamics prohibited this analysis.
- The effect of increased weather resistance was investigated and seen to reduce both engine speed and ship surge velocity.

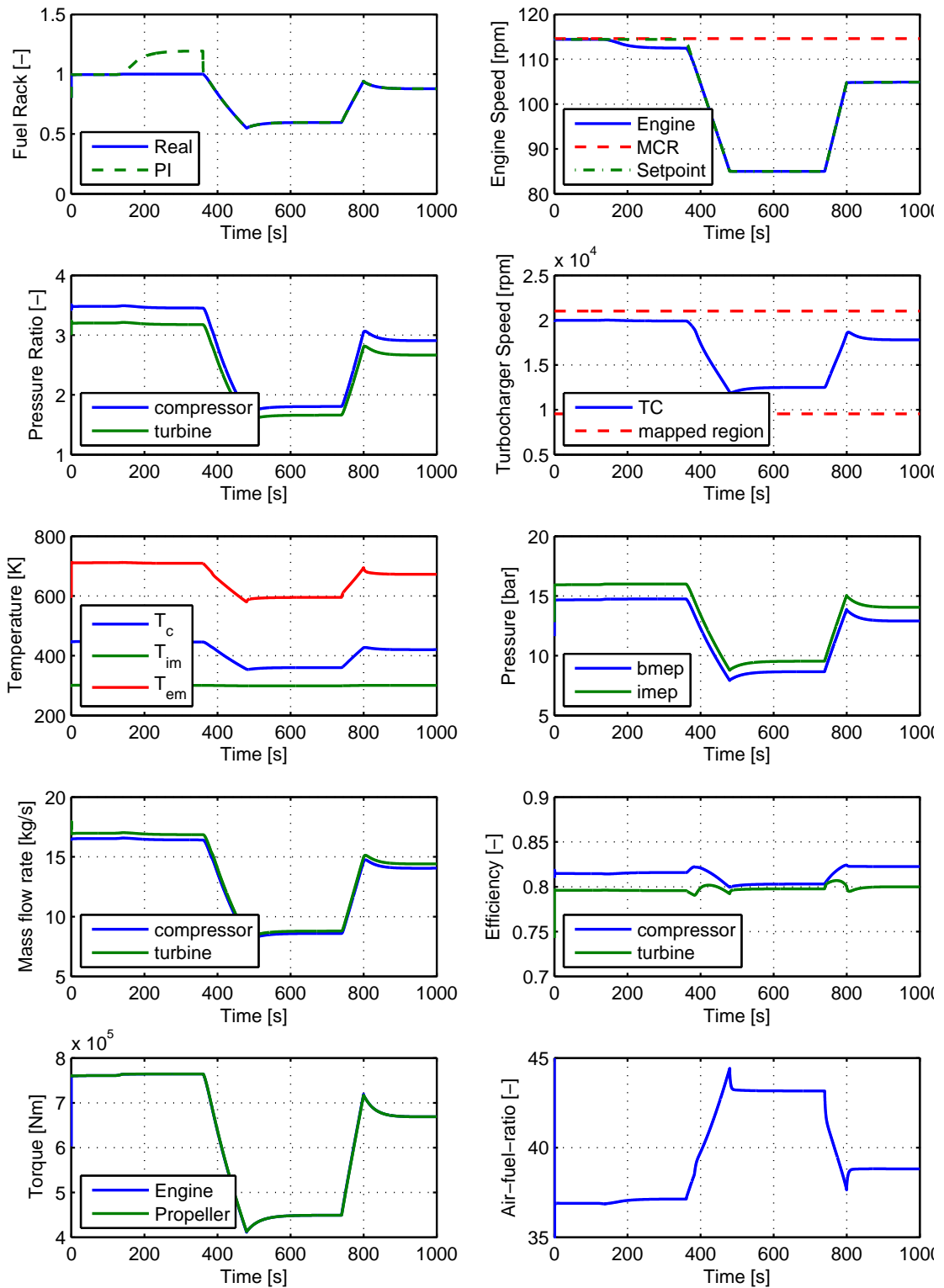


Figure 7.3: Simulation of the engine and turbocharger with PI-controller.

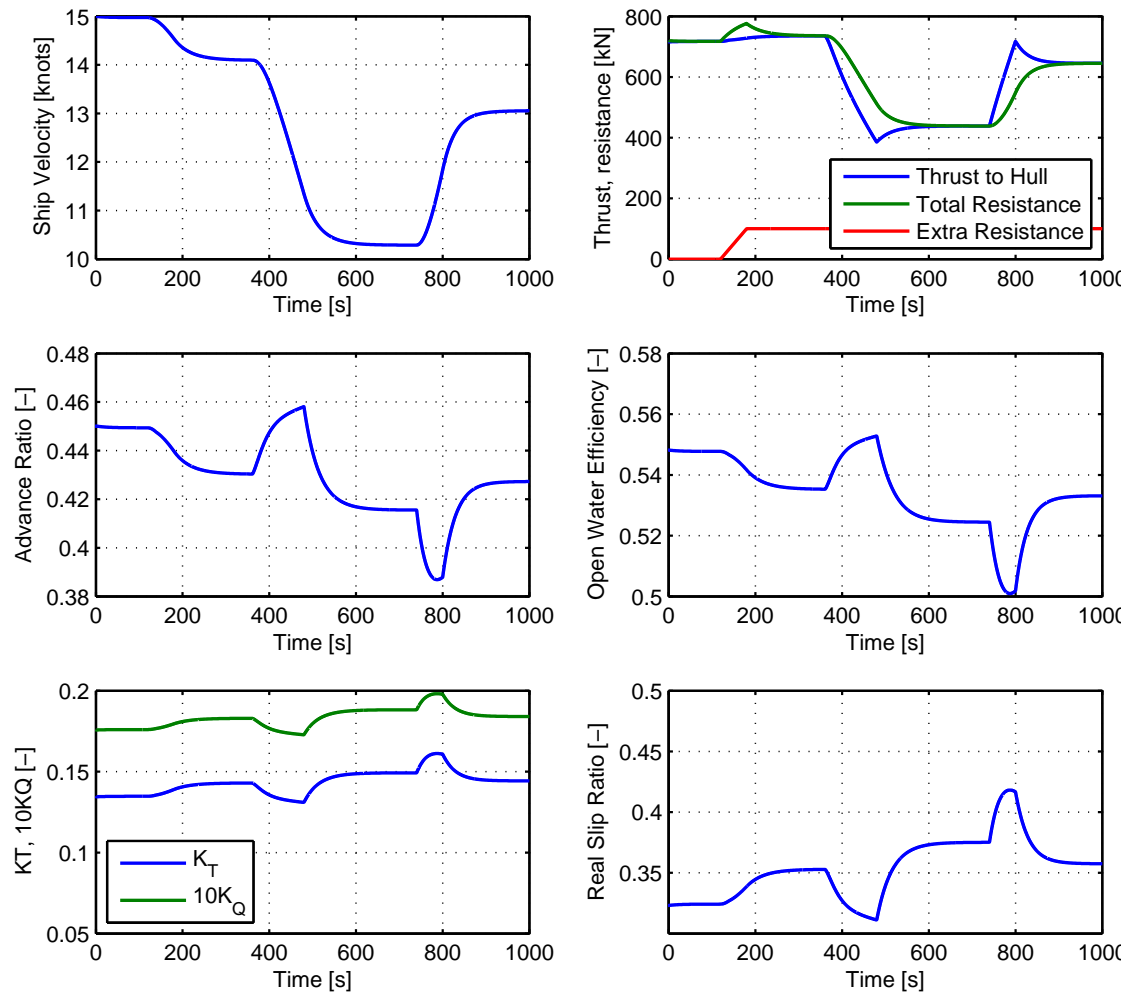


Figure 7.4: Simulation of the ship and propeller with PI-controller

Chapter 8

Final Conclusions and Future Work

8.1 Conclusions

This thesis focused on the modeling of a ship propulsion plant for the use in controller design of various applications. Moreover to be used in testing these controllers. Simulations were performed to verify that the models behaved as anticipated and that the interaction between the models functioned correctly.

In Chapter 3 modeling of the compressor map by curve fitting was done. A new and improved flow rate model was developed by the use of exponential functions. The new model showed to achieve better results than a commonly used method from literature. However, to prove that the results hold in general further testing on other compressor maps is needed. Due to the lack of experimental data at low turbocharger speeds a compressor model with adequate extrapolation capabilities is essential. Simulation in Chapter 6 showed that the developed model performed good during low engine loads and consequently low turbocharger speeds. Since linear interpolation is a normal approach and the fact that it can not extrapolate, these simulation results are an incentive to use parameter fitted models instead of linear interpolation of turbocharger maps. Furthermore, the accurate modeling of the turbocharger paves the way for development of transient air-to-fuel ratio control and exhaust gas recirculation.

Chapter 4 dealt with modeling of the turbine. The common turbine flow rate expression was successfully translated to the atypical flow rate provided in the map. Three different turbine flow rate models were tested, whereas two showed good performance and the last choked too early. As limited data on turbine efficiency was available a general purpose modeling approach was carried out. Simulations in Chapter 6 proved the efficiency model to work decently, and did not alter the engine performance in total. A modification of the equation regarding mass flow through a restriction was also done due to possible numerical problems arising at

low pressure ratios.

Modeling the propeller, ship surge and engine extensions were the subjects of Chapter 5. The propeller thrust, torque and entrained water inertia were examined. Restrictions were set to only include operations in the 1st propeller quadrant. To calculate the propeller thrust and torque coefficients the propeller advance speed was needed, thus a basic ship surge model was developed. Lastly, the engine was extended with an intercooler and fuel limiters based on torque and scavenging air pressure values.

Chapter 6 examined the engine and turbocharger performance through simulations. The simulations showed that heat loss in the exhaust manifold should be included as temperatures were a bit higher than in the engine performance curves. It was seen that nonlinear effects were present in the simulation, especially during rapid acceleration with reduced air-to-fuel ratio and because of slow turbocharger dynamics. Moreover, it was observed that overload protection prohibited low air-fuel ratios at the expense of a slower engine response. However, the appropriate implementation of EGR, VAT or wastegate control could render the need for overload protection unnecessary.

Chapter 7 addressed the issue of engine speed control. A PI controller was implemented with integrator anti-windup due possible saturation of the fuel index. Simulation of the total ship propulsion system was covered. In simulation it was shown that interaction between all subsystem worked and the simulation performance was realistic. The PI controller managed to follow a slowly varying setpoint and windup was avoided. However, further examination of the controller should be performed as the controller is linear and the system nonlinear. Moreover, the problem of load fluctuations and subsequent engine overspeed was not possible to analyze as simplifications in the fuel dynamics and engine torque creation prevented this. Nonetheless, the effect of varying weather conditions on engine speed was inspected.

All in all, the purpose of this thesis was to give an overview over the subject of ship propulsion modeling and to create a testing environment for controller design. Simulations showed that all subsystems functioned together and gave realistic results. The modeling procedure illuminated what parameters affect the engine performance and how those could be controlled. By contributing to better understanding of the process, safer operation of the engine can be proposed. The thesis bridges the gap between engine torque generation and propeller torque absorption. Furthermore, the successful implementation of the PI controller and the accurate performance of the turbocharger model leads to the conclusion that the propulsion model can be used in various controller design and to test controller performance. This avoids having to involve a large diesel engine and ship, at least in the initial stage, for testing the controller performance. This reduces testing costs and the potential harm of the environment and people in the event of bad controller performance.

8.2 Recommendations for Future Work

- Include a realistic heat loss model for the exhaust manifold.
- Extend the engine by adding EGR, VAT and/or wastegate.
- Develop control algorithms for EGR, VAT and/or wastegate to control the transient air-to-fuel ratio, to avoid the use of the scavenging air limiter and to reduce pollutants.
- Perform an analysis of the nature of propeller torque fluctuations and develop a robust control algorithm to prevent overspeed of the engine by suppression of torque loss.
- Extend the propeller model to all four quadrants.
- Include a propeller model for controllable pitch propellers.
- Perform linearization of the propulsion plant model and incorporate gain scheduling and parameter tuning.
- Develop a nonlinear controller for engine speed.
- Verify the exponential compressor flow model against other compressor maps. Further compare the performance to the method of rectangular hyperbolas suggested in literature.

Bibliography

- [1] MAN Diesel & Turbo, Copenhagen, Denmark, *Basic Principles of Ship Propulsion*, December 2011.
- [2] MAN B&W Diesel A/S, *L60MC-C Mk7 Project Guide*, 2001.
- [3] MAN Diesel & Turbo, Copenhagen, Denmark, *Propulsion Trends in Bulk Carriers*, December 2010.
- [4] A. T. Karlsen, “Mean value modeling of a two-stroke diesel engine,” project work, Norwegian University of Science and Technology, Department of Engineering Cybernetics, Trondheim, December 2011.
- [5] E. V. Lewis, ed., *Principles of Naval Architecture*. Society of Naval Architects and Marine Engineers, 1989.
- [6] A. J. Sørensen, “Marine control systems - propulsion and motion control of ships and ocean structures,” lecture notes, Norwegian University of Science and Technology, Department of Marine Technology, January 2011.
- [7] J. Carlton, *Marine Propellers and Propulsion*. Elsevier Butterworth-Heinemann, 2007.
- [8] M. W. C. Oosterveld and P. Van Oossanen, “Further computer-analyzed data of the wageningen b-screw series,” *International shipbuilding progress*, vol. 22, 1975.
- [9] G. P. Theotokatos, “A modelling approach for the overall ship propulsion plant simulation,” in *Proceedings of the 6th WSEAS international conference on System science and simulation in engineering*, ICOSSE’07, (Stevens Point, Wisconsin, USA), pp. 80–87, World Scientific and Engineering Academy and Society (WSEAS), 2007.
- [10] J. Ghose and R. Gokarn, *Basic Ship Propulsion*. Allied Publishers, 2004.
- [11] Ø. N. Smogeli, *Control of Marine Propellers : from Normal to Extreme Conditions*. PhD thesis, Norwegian University of Science and Technology, Department of Marine Technology, 2006.

-
- [12] C. Moler, *Numerical Computing With MATLAB*. Society for Industrial and Applied Mathematics, 2004.
- [13] C. Kelley, *Iterative Methods for Optimization*. Frontiers in Applied Mathematics, Siam, 1999.
- [14] C. De Boor, *A Practical Guide to Splines*. No. 27 in Applied Mathematical Sciences, Springer, 2001.
- [15] G. O. Kaasa, *Nonlinear output-feedback control applied for pneumatic clutch actuation in heavy-duty trucks*. PhD thesis, Norwegian University of Science and Technology, August 2004. Preliminary Draft.
- [16] P. Moraal and I. Kolmanovsky, “Turbocharger modeling for automotive control applications,” *SAE Technical Paper 1999-01-0908*, no. 724, 1999.
- [17] C. Rakopoulos and E. Giakoumis, “Review of thermodynamic diesel engine simulations under transient operating conditions,” *SAE Technical Paper 2006-01-0884*, no. 884, 2006.
- [18] O. Leufven, “Compressor modeling for control of automotive two stage turbochargers,” tech. rep., Linköping University, 2010. LiU-TEK-LIC-2010:32, Thesis No. 1463.
- [19] L. Eriksson, “Modélisation et contrôle de moteurs suralimentés à allumage commandé et à injection directe,” *Oil & Gas Science and Technology - Rev. IFP*, vol. 62, no. 4, pp. 523–538, 2007.
- [20] L. Guzzella and C. H. Onder, *Introduction to modeling and control of internal combustion engine systems*. New York, NY: Springer, 2 ed., 2009.
- [21] G. Martin, V. Talon, P. Higelin, A. Charlet, and C. Caillol, “Implementing turbomachinery physics into data map-based turbocharger models,” *SAE Int. J. Engines*, vol. 2, pp. 211–229, 2009.
- [22] K. Ghorbanian and M. Gholamrezaei, “An artificial neural network approach to compressor performance prediction,” *Applied Energy*, vol. 86, pp. 1210 – 1221, 2009.
- [23] Y. Yu, L. Chen, F. Sun, and C. Wu, “Neural-network based analysis and prediction of a compressor’s characteristic performance map,” *Applied Energy*, vol. 84, no. 1, pp. 48 – 55, 2007.
- [24] D. N. Malkhede, B. Seth, and H. Dhariwal, “Mean value model and control of a marine turbocharged diesel engine,” *SAE Technical Paper 2005-01-3889*, 2005.

-
- [25] J. Gravdahl and O. Egeland, *Compressor Surge and Rotating Stall: Modelling and Control*. Advances in Industrial Control, Springer, 1999.
- [26] J. Bergström and O. Leufvén, “Surge modeling and control of automotive turbochargers,” Master’s thesis, Linköpings Universitet, SE-581 83 Linköping, 2007.
- [27] L. Eriksson, L. Nielsen, J. Brugård, J. Bergström, F. Pettersson, and P. Andersson, “Modeling of a turbocharged si engine,” *Annual Reviews in Control*, vol. 26, no. 1, pp. 129 – 137, 2002.
- [28] N. Xiros, *Robust Control of Diesel Ship Propulsion*. Springer, 2002.
- [29] J. Woud, P. Boot, and B. Riet, “A diesel engine model for the dynamic simulation of propulsion systems,” 1993.
- [30] J. B. Heywood, *Internal Combustion Engine Fundamentals*. New York: McGraw-Hill, 1988.
- [31] D. MacPherson, V. Puleo, and M. Packard, “Estimation of entrained water added mass properties for vibration analysis,” *SNAME New England Section*, Jun 2007.
- [32] R. Izadi-Zamanabadi, *A Ship Propulsion System as a Benchmark for Fault-tolerant Control*. Department of Control Engineering, Aalborg University, 1997.
- [33] T. Fossen, *Handbook of Marine Craft Hydrodynamics and Motion Control*. John Wiley & Sons, 2011.

Appendix A

Engine/Turbocharger Performance Curves

This appendix contains the performance curves of a MAN Diesel & Turbo TCA55 turbocharger (Figures A.1 and A.2) and the MAN B&W 6L60MC Mk7 two stroke marine diesel engine (Figure A.3)

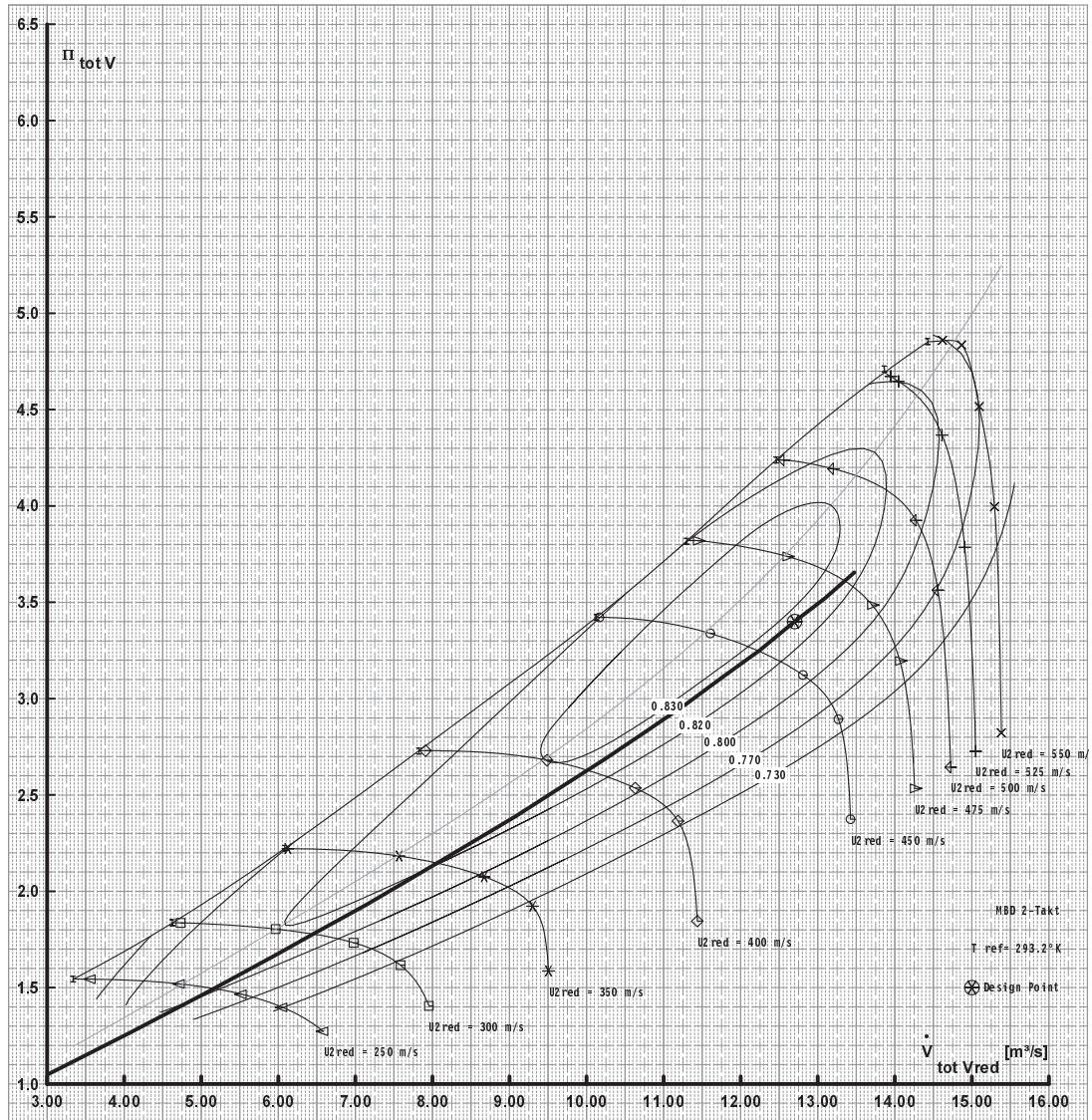
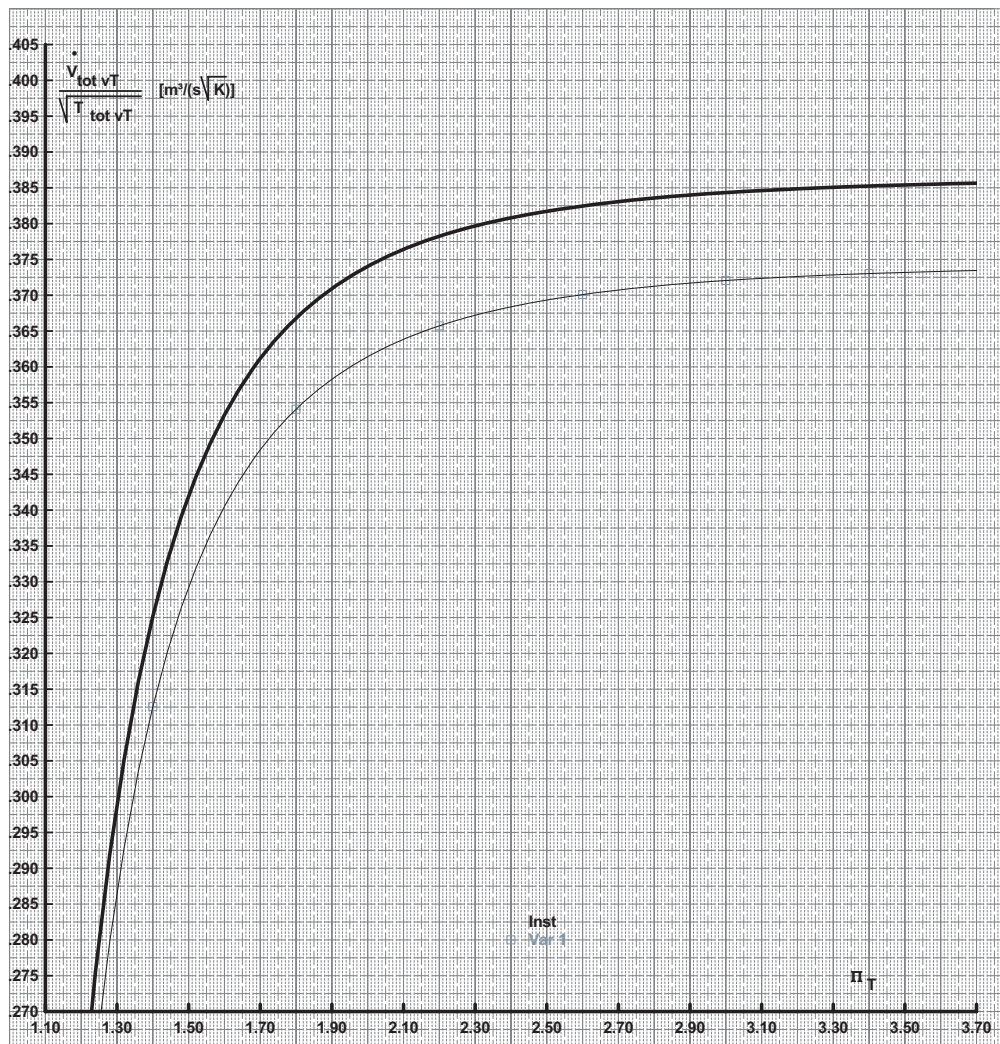


Figure A.1: Compressor map for a MAN Diesel & Turbo TCA55 turbocharger (Courtesy of MAN Diesel & Turbo).

Turbine Characteristic TCA55-21064 for 6S46MC-C; 6480 KW / 129 rpm

SPEC: TCA55-21ATP015AND0307



05.06.2008

Böhringer

Figure A.2: Turbine flow rate map for a MAN Diesel & Turbo TCA55 turbocharger (Courtesy of MAN Diesel & Turbo).

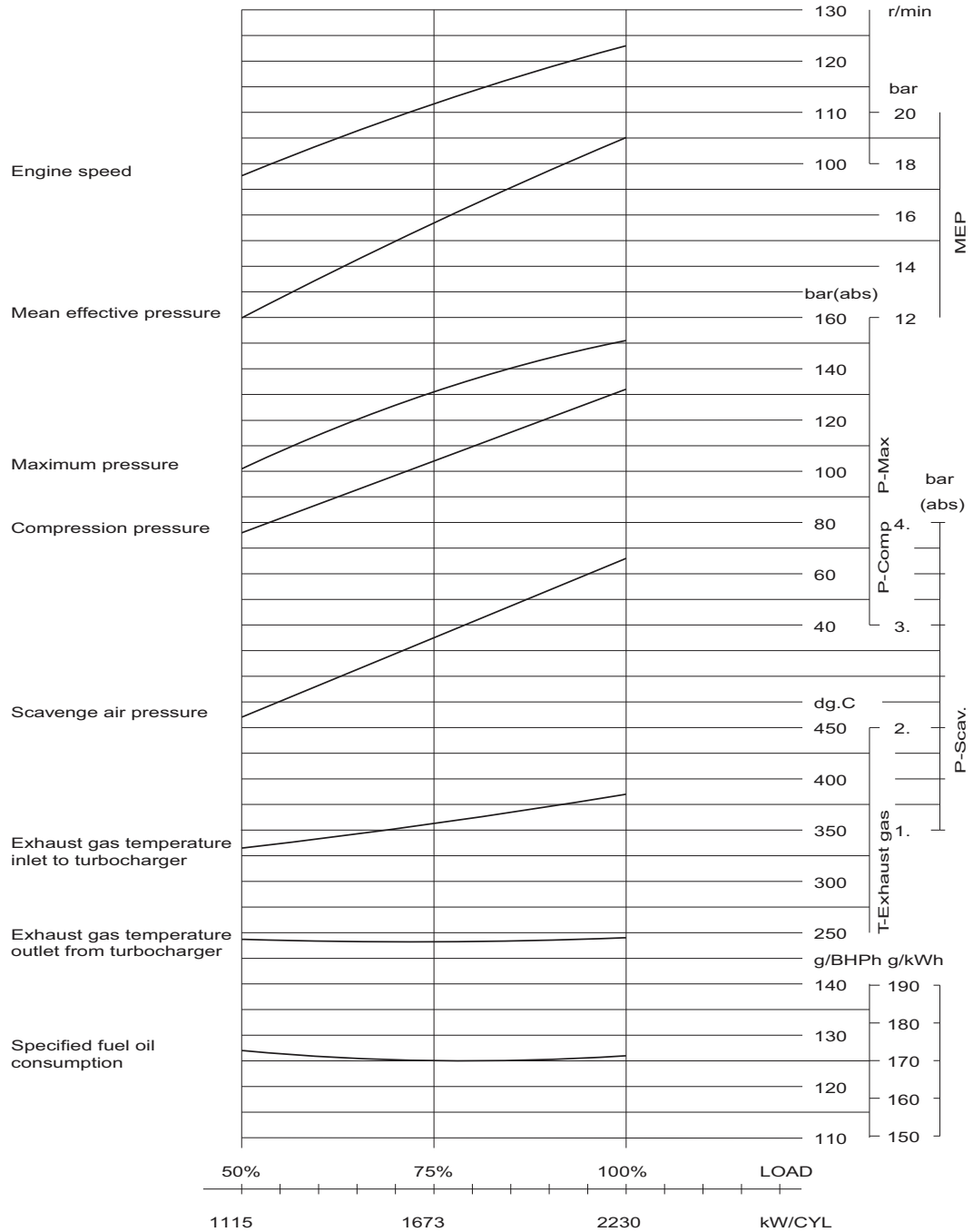


Figure A.3: Performance curves for the MAN B&W 6L60MC-C mk7 two stroke marine diesel engine [2].

Appendix B

Tables of Coefficients

This appendix contain tables of coefficients obtained from curve fitting of various models (Tables B.1, B.2, B.3 and B.4) and the coefficients provided for use in the modeling of the propeller (Table B.5)

Table B.1: Regression coefficients from least squares fit of the exponential compressor flow model (3.20).

Parameter	Value
a_3	-0.2035
a_2	0.6938
a_1	-0.7479
a_0	0.3722
b_2	-11.0505
b_1	27.5087
b_0	-10.4700
c_2	5.5616
c_1	-15.0297
c_0	5.0098

Table B.2: Regression coefficients from least squares fit of the exponential threshold compressor flow model (3.29). Note that the polynomial order of the expressions (3.26) and (3.28) are increased by 1 to increase precision.

Parameter	Value
a_4	0.1735
a_3	-1.0603
a_2	2.2252
a_1	-1.9101
a_0	0.7071
b_2	-58.5565
b_1	146.9636
b_0	-66.9756
c_5	1.1172
c_4	-6.1368
c_3	13.0943
c_2	-13.1055
c_1	5.7735
c_0	0.5490

Table B.3: Regression coefficients from least squares fit of the alternative compressor flow model by rectangular hyperbolas (3.35).

Parameter	Value
k_{11}	0.1171
k_{12}	0.0790
k_{13}	-0.0362
k_{21}	-1.8262
k_{22}	0.7919
k_{23}	-0.2719
k_{31}	0.0638
k_{32}	0.1049
k_{33}	-0.0432

Table B.4: Parameters from least squares fit of the 5th order compressor efficiency polynomial in (3.41).

Parameter	Value
p_{00}	0.3281000
p_{10}	-0.2666000
p_{01}	1.5450000
p_{20}	-0.0646800
p_{11}	0.8046000
p_{02}	-2.2500000
p_{30}	0.0133600
p_{21}	-0.1018000
p_{12}	0.0321300
p_{03}	0.5638000
p_{40}	-0.0020570
p_{31}	0.0210600
p_{22}	-0.0748400
p_{13}	0.1515000
p_{04}	-0.1937000
p_{50}	0.0000094
p_{41}	-0.0010670
p_{32}	0.0043970
p_{23}	-0.0084410
p_{14}	0.0051110
p_{05}	0.0057780

Table B.5: Coefficients for K_T and K_Q for the Wageningen B-screw series propeller used in (5.5) and (5.6).

(a) Thrust coefficients.						(b) Torque coefficients.					
n	$C_{s,t,u,v}$	s	t	u	v	n	$C_{s,t,u,v}$	s	t	u	v
1	0.0088049600	0	0	0	0	1	0.0037936800	0	0	0	0
2	-0.2045540000	1	0	0	0	2	0.0088652300	2	0	0	0
3	0.1663510000	0	1	0	0	3	-0.0322410000	1	1	0	0
4	0.1581140000	0	2	0	0	4	0.0034477800	0	2	0	0
5	-0.1475810000	2	0	1	0	5	-0.0408811000	0	1	1	0
6	-0.4814970000	1	1	1	0	6	-0.1080090000	1	1	1	0
7	0.4154370000	0	2	1	0	7	-0.0885381000	2	1	1	0
8	0.0144043000	0	0	0	1	8	0.1885610000	0	2	1	0
9	-0.0530054000	2	0	0	1	9	-0.0037087100	1	0	0	1
10	0.0143481000	0	1	0	1	10	0.0051369600	0	1	0	1
11	0.0606826000	1	1	0	1	11	0.0209449000	1	1	0	1
12	-0.0125894000	0	0	1	1	12	0.0047431900	2	1	0	1
13	0.0109689000	1	0	1	1	13	-0.0072340800	2	0	1	1
14	-0.1336980000	0	3	0	0	14	0.0043838800	1	1	1	1
15	0.0063840700	0	6	0	0	15	-0.0269403000	0	2	1	1
16	-0.0013271800	2	6	0	0	16	0.0558082000	3	0	1	0
17	0.1684960000	3	0	1	0	17	0.0161886000	0	3	1	0
18	-0.0507214000	0	0	2	0	18	0.0031808600	1	3	1	0
19	0.0854559000	2	0	2	0	19	0.0158960000	0	0	2	0
20	-0.0504475000	3	0	2	0	20	0.0471729000	1	0	2	0
21	0.0104650000	1	6	2	0	21	0.0196283000	3	0	2	0
22	-0.0064827200	2	6	2	0	22	-0.0502782000	0	1	2	0
23	-0.0084172800	0	3	0	1	23	-0.0300550000	3	1	2	0
24	0.0168424000	1	3	0	1	24	0.0417122000	2	2	2	0
25	-0.0010229600	3	3	0	1	25	-0.0397722000	0	3	2	0
26	-0.0317791000	0	3	1	1	26	-0.0035002400	0	6	2	0
27	0.0186040000	1	0	2	1	27	-0.0106854000	3	0	0	1
28	-0.0041079800	0	2	2	1	28	0.0011090300	3	3	0	1
29	-0.0006068480	0	0	0	2	29	-0.0003139120	0	6	0	1
30	-0.0049819000	1	0	0	2	30	0.0035985000	3	0	1	1
31	0.0025983000	2	0	0	2	31	-0.0014212100	0	6	1	1
32	-0.0005605280	3	0	0	2	32	-0.0038363700	1	0	2	1
33	-0.0016365200	1	2	0	2	33	0.0126803000	0	2	2	1
34	-0.0003287870	1	6	0	2	34	-0.0031827800	2	3	2	1
35	0.0001165020	2	6	0	2	35	0.0033426800	0	6	2	1
36	0.0006909040	0	0	1	2	36	-0.0018349100	1	1	0	2
37	0.0042174900	0	3	1	2	37	0.0001124510	3	2	0	2
38	0.0000565229	3	6	1	2	38	-0.0000297228	3	6	0	2
39	-0.0014656400	0	3	2	2	39	0.0002695510	1	0	1	2
						40	0.0008326500	2	0	1	2
						41	0.0015533400	0	2	1	2
						42	0.0003026830	0	6	1	2
						43	-0.0001843000	0	0	2	2
						44	-0.0004253990	0	3	2	2
						45	0.0000869243	3	3	2	2
						46	-0.0004659000	0	6	2	2
						47	0.0000554194	1	6	2	2

Appendix C

Matlab/Simulink Files

This appendix gives a short description of the Matlab/Simulink files in the digital attachment of this thesis. The Matlab initialization file is included in the appendix to present the constants and initial values used in the simulation.

Table C.1: Description of Matlab scripts.

File	Description
<code>cmap_eff.m</code>	Curve fitting and plotting of the compressor map efficiency.
<code>cmap_flw.m</code>	Interpolation, curve fitting and plotting of the compressor flow rate models.
<code>cmapImport.m</code>	Imports the samples from the compressor map, saves the information to <code>cmap.mat</code> .
<code>init.m</code>	Initialization of the simulation variables.
<code>simRun.m</code>	Runs the simulation and plots simulation data.
<code>tmap.m</code>	Curve fitting and plotting of the turbine map models

Table C.2: Description of Matlab functions.

File	Description
compflw.m	Finds the compressor volume flow rate (3.30) for the compressor flow model (3.20).
compflw_alt.m	Finds the compressor volume flow rate (3.30) for the alternative compressor flow model (3.35).
compflwEmbedded.m	Finds the compressor volume flow rate (3.30) for the compressor flow model (3.20). Modified to work as an function within Simulink.
surfaceFitEff.m	Finds the 5th order polynomial coefficients for the compressor efficiency. ^a
surfaceFitQ.m	Fits a surface to the compressor speed line samples using cubic interpolation. Turbocharger blade speed and pressure ratio is input, volume flow rate is output. Used to find the unknown air flow rate through the compressor. ^a
surfaceFitU.m	Fits a surface to the compressor speed line samples using cubic interpolation. Flow rate and pressure ratio is input, turbocharger speed is output. Used for 3D plotting of the speed lines. ^a
turbflw.m	Calculates the turbine flow rate (4.18)
turbflw2.m	Calculates the turbine flow rate (4.17)

^aUses curve fitting toolbox.

Table C.3: Description of data files.

File	Description
ceff.mat	Contains the compressor efficiency model coefficients.
cflw.mat	Contains the compressor flow rate model coefficients.
cmap.mat	Contains samples of the speed and efficiency curves of the real compressor map.
KQ.txt	Contains the propeller torque coefficients.
KT.txt	Contains the propeller thrust coefficients.
tflw.mat	Contains the turbine flow model coefficients.

Table C.4: Description of Simulink files and Matlab functions within.

File	Description
<code>simDiagram.mdl</code>	Simulink diagram of the ship propulsion plant system.
<code>engine</code>	Calculates all the entire engine process, outputs the differential equations for the engine and plotting data of interest.
<code>prop</code>	Calculates the propeller thrust and torque.
<code>scavLim</code>	Implements the fuel limiter according to scavenge air pressure.
<code>torqueLim</code>	Implements the fuel limiter according to the torque limits.

Listing C.1: engineInit.m

```

1 %% engineInit.m
2 %
3 %   Script for setting the engine constants and initial values for simulation
4 %
5 % Author: Andreas Torp Karlsen (andreas.t.karlsen@gmail.com)
6 % Last revised: 18.06.2012
7 %%
8
9 clear all;
10 clc;
11
12 global k_a R_a T_amb c_pa d_c % for use in 'compflw' and 'compflw_alt', global to ...
    avoid passing as parameters
13
14 nx = 6; % Number of engine states
15 ni = 25; % Number of intermediate/plotting variables
16
17 % Values for MAN-B&V 6L60MC-C MK6(Xiros 2002, p.34)
18 P_mcr = 9177*10^3; % Engine MCR power[W]
19 N_mcr = 114.6; % Engine MCR speed[rpm]
20 z_c = 6; % Number of engine cylinders
21 V_d = 0.5429; % Engine displaced volume pr cylinder [m^3]
22 J_tot = 59800; % Engine + propeller nominal moment of inertia [kg m^2]
23 p_imax = 16*10^5; % Maximum imep [Pa]
24 T_ep = 273+230; % Exhaust pipe temperature [K]
25 k_f2 = 0.03;
26 k_f1 = 681.3110;
27 k_f0 = 818.2450;
28 k_f = [k_f2 k_f1 k_f0]; % Friction pressure coefficients
29
30 % Thermodynamic values
31 T_amb = 293.2; % Ambient temperature [K]
32 p_amb = 101325; % Ambient/athmospheric pressure [Pa]
33 c_pa = 1005; % Specific heat capacity air, constant pressure [J/(kg K)]
34 c_va = 718; % Specific heat capacity for air at constant volume [J/(kg K)]
35 c_pe = 1117; % Specific heat capacity exhaust gas at constant pressure ...
    [J/(kg K)]
36 k_a = 1.4; % Ratio of specific heats for air [J/(kg K)]
37 k_e = 1.34; % Ratio of specific heats for exhaust [J/(kg K)] at (400-1100K)
38 R_a = 287; % Specific gas constant air [J/(kg K)]
39 R_e = 277.1; % Specific gas constant exhaust [J/(kg K)]
40
41 % Fuel Values
42 AFR_s = 14.7; % Stoichiometric air/fuel ratio
43 AFR_high = 22; % Air/fuel ratio for perfect combustion,
44 AFR_low = 8.0; % Lean flamability limit
45 H_l = 40640*10^3; % Fuel lower heating value [J/kg]
46 m_fmax = 0.0393; % Max fuel amount per cylinder per cycle [kg]
47 k_z1 = 0.0105*10^-5;
48 k_z0 = 0.3120;
49 k_z = [k_z1 k_z0]; % Fuel chemical energy proportion in ex. gas coefficient
50
51 % Valves / Orifices
52 c_d = 0.9; % Inlet port/exhaust valve flow discharge coefficient
53 A_Veq = 0.04; % Inlet port/exhaust valve mean equivalent area [m^2]
54 Pi_tr = 0.95; % Treshold for pressure ratio so that calculation retains Lipchitz
55
56 % Intercooler
57 T_water = 298; % Coolant water temperature [K]
58 eta_ic = 0.98; % Intercooler efficiency
59
60 % Intake/exhaust manifold
61 V_im = 1.5*V_d; % Volume intake manifold [m^3]
62 V_em = 1.5*V_d; % Volume exhaust manifold [m^3]
63 eta_em = 1; % Exhaust manifold thermodynamic efficiency
64
65 % Turbocharger
66 J_tc = 1.5*4.83; % Inertia of turbocharger system [kg m^2]
67 d_c = 0.5; % Compressor diameter [m]
68 d_t = 0.5; % Turbine diameter [m]
69 eta_t_max = 0.82; % Turbine max efficiency
70 bsr_max = 0.7; % Turbine blade speed ratio at max efficiency
71 k_t = 2; % Turbine efficiency coefficient
72 T_a0 = 293.2; % Turbine inlet temperature in map [K]
73 k_srg = [4.5895*10^-5, 0.0018, -0.0645]; % Polynomial coefficients for the surge ...
    volume flow
74
75 % Propeller load dynamics
76 rho_a = 1.23; % Density of air [kg m^-3]
77 rho_w = 1025; % Sea water density [kg/m^3]
78 w = 0.277; % Wake fraction number
79 Q_mcr = P_mcr/(((2*pi)/60)*N_mcr);
80 k_Q0 = Q_mcr / N_mcr^2; % Propeller curve torque coefficient [N m/rpm^2]
81
82 % Propeller parameters
83 D = 6.5; % Propeller diameter [m]

```

```

84 Z = 5; % Number of propeller blades [-]
85 PD = 0.665; % Propellerpitch to diameter ratio [-]
86 EAR = 0.57; % Propeller area ratio [-]
87 J_ew = ((0.0703*PD^2*EAR^2)/(pi*Z))*rho_w*D^5; % Entrained water inertia [kg m^2]
88 J_tot = J_tot + J_ew; % Shafting system total moment of inertia
89
90
91 % Ship parameters
92 s_dw = 55000; % Ship size (at scantling draught) [dwt]
93 l_oa = 190; % Length overall [m]
94 l_pp = 183; % Length between perpendiculars [m]
95 B = 32.26; % Breadth [m]
96 D_s = 12.7; % Scantling draught [m]
97 D_d = 11.5; % Design draught [m]
98 M_s = 6.358*10^6; % Ship mass [kg]
99 M_a = 0.25*M_s; % Added mass [kg]
100 t_d = 0.2; % Thrust deduction coefficient [-]
101
102 % Governor parameters
103 Kp = 1; % Proportional gain (PID)
104 Ki = 0.1; % Integrator gain (PID)
105 Kw = 1; % Integrator anti-windup gain (inverse of anti-windup ...
reset time constant)
106 u_lb = 0; % Fuel rack lower bound
107 u_ub = 1; % Fuel rack upper bound
108 k_trq = [0.4, 1, 0.4, 0.8]; % Torque limiter constants
109 k_scv = [0.5, 1, 1.2, 2.0]; % Scavenge limiter constants
110
111 % Initial values
112 p_im0 = 3.5*p_amb; % Intake manifold pressure [Pa]
113 T_im0 = 300; % Intake manifold temperature [K]
114 p_em0 = 3*p_amb; % Exhaust manifold pressure [Pa]
115 T_em0 = 600; % Exhaust manifold temperature [K]
116 w_e0 = 114.6*(2*pi)/60; % Engine angular frequency [rad/s]
117 w_tc0 = 20000*(2*pi)/60; % Turbocharger angular frequency [rad/s]
118 u_0 = 1; % Initial fuel rack position
119 V_s0 = 15*0.5144; % Initial ship speed [m/s]
120
121 x0 = [p_im0; T_im0; p_em0; T_em0; w_tc0; w_e0];
122
123 % Creating the thrust (K_T) and torque (K_Q) coefficients
124 J = 0:0.01:0.74; % Range of advance speed
125 [C_T,s,t,u,v] = textread('KT.txt', '%f %d %d %d %d'); %Import the polynomial coefficients
126 K_T = zeros(size(J));
127 for i = 1:length(K_T)
128     for j = 1:length(C_T)
129         K_T(i) = K_T(i) + C_T(j)*J(i)^s(j)*PD^t(j)*EAR^u(j)*Z^v(j);
130     end
131 end
132 [C_Q,s,t,u,v] = textread('KQ.txt', '%f %d %d %d %d'); %Import the polynomial coefficients
133 K_Q = zeros(size(J));
134 for i = 1:length(K_Q)
135     for j = 1:length(C_Q)
136         K_Q(i) = K_Q(i) + C_Q(j)*J(i)^s(j)*PD^t(j)*EAR^u(j)*Z^v(j);
137     end
138 end
139
140 % Calculation of ship resistance coefficient
141 Vmax = 15*0.5144444;
142 KTT = ((1-w)*Vmax) / (N_mcr*D/60);
143 KTTi = interp1(J,K_T,KTT,'linear');
144 KQQi = interp1(J,K_Q,KTT,'linear');
145 Chat_T = (1-t_d)*KTTi*rho_w*D^4*(N_mcr/60)^2/Vmax^2;
146
147 % Setting default plotting properties
148 set(0,'defaultlinelinerwidth',1.5)
149 set(0,'defaultaxeslinelinerwidth',1)
150 %set(0,'defaultMarkerSize',10)
151 %set(0,'defaultpatchlinelinerwidth',1)
152 %set(0,'DefaultAxesColorOrder',[0 0 0],'DefaultAxesLineStyleOrder','-|-.|--|:')

```